Research Square

Preprints are preliminary reports that have not undergone peer review.
They should not be considered conclusive, used to inform clinical practice,
or referenced by the media as validated information.

Functional genomics reveals a role for lysosomal nutrient sensing in tenocyte biology and Achilles tendon repair

Valerie Salazar

valerie.salazar@novartis.com

Novartis Pharma AG https://orcid.org/0000-0002-2111-9313

Sophia Pantasis

Novartis Pharma AG https://orcid.org/0000-0003-4221-8246

Benjamin Jourde

Novartis (Switzerland)

Doriane Eckert

Novartis Pharma AG

Amelie Sauty de Chalon

Novartis Pharma AG

Claudia Agarinis

Novartis Pharma AG

Maurane Henry

Novartis Pharma AG

Isabelle Garnier

Novartis Institutes for Biomedical Research

Michael Obrecht

Novartis Pharma AG

Alexandra Schober

Novartis Pharma AG

Alexandra Vissieres

Analytical Sciences and Imaging, Novartis Institutes for Biomedical Research, Basel

Charles Moes

Novartis Pharma AG

Heike Butendeich

Novartis Pharma AG

Immihan Yasa

The Hong Kong University of Science and Technology - Guangzhou Campus https://orcid.org/0000-0002-5013-7246

Joanna Mitchelmore
Novartis Biomedical Research
Tai Nguyen
Novartis Pharma AG
John Reece-Hoyes
Novartis Institutes for BioMedical Research
Florian Nigsch
Novartis Institutes for BioMedical Research https://orcid.org/0000-0002-2919-8749
Joerg Schlotterbeck
Novartis Pharma AG
Dieter Staab
Novartis Pharma AG https://orcid.org/0009-0000-1509-700X
Stephanie Chreng
Novartis Pharma AG
Ioannis Moutsatsos
Novartis Pharma AG
Isabelle Claerr
Novartis Pharma AG
Vincent Unterreiner
Novartis Pharma AG
Martin Rausch
Novartis Pharma AG
Daniela Gabriel
Novartis Institutes for Biomedical Research
Mirko Arcuri
Novartis Pharma AG
Natalie Accart
Novartis Pharma AG
Sophie Brachat
Novartis Institutes for BioMedical Research
Johannes Voshol
Novartis Pharma AG
Leslie Ofori
Novartis Pharma AG
Fanny Decarpentrie
Novartis Pharma AG
Olivier Leupin
Novartis Pharma AG
Fanning Zeng

Novartis Institutes for Biomedical Research
Yufei Li
Novartis Pharma AG
Claudia Merkl
Novartis Institutes for Biomedical Research
Nicolau Beckmann
Novartis Institutes for Biomedical Research
Sabine Guth-Gundel
Novartis Pharma AG
Michaela Kneissel
Novartis Institutes for BioMedical Research
Christian Parker
Novartis Institutes for BioMedical Research

Article

Keywords: Tendon, Tenocyte, Achilles, Rotator cuff, Regeneration; Lysosomal Nutrient-Sensing; LAMTOR, Ragulator

Posted Date: November 13th, 2026

DOI: https://doi.org/10.21203/rs.3.rs-11084138/v1

License: This work is licensed under a Creative Commons Attribution 4.0 International License.
Read Full License

Additional Declarations: Yes there is potential Competing Interest. All authors were employed by Novartis Pharma AG during the completion of this work.

Functional genomics reveals a role for lysosomal nutrient sensing in tenocyte biology and Achilles tendon repair

Short title: Lysosomal nutrient-sensing regulates tenogenesis

Sophia Pantasis[1], Benjamin Jourde[1], Doriane Eckert[1], Amelie Sauty de Chalon[1], Claudia Agarinis[3], Maurane Henry[1], Isabelle Garnier[1], Michael Obrecht[1], Alexandra Schober[2], Alexandra Vissières[3], Charles Moes[1], Heike Butendeich[3], Immihan Ceren Yasa[3], Joanna Mitchelmore[1], Tai Nguyen[4], John Reece-Hoyes[5], Florian Nigsch[3], Joerg Schlotterbeck[3], Dieter Staab[3], Stephanie Chreng[3], Ioannis Moutsatsos[6], Isabelle Claerr[3], Vincent Unterreiner[3], Martin Rausch[3], Daniela Gabriel[3], Mirko Arcuri[7], Natalie Accart[1], Sophie Brachat[1], Johannes Voshol[3], Leslie Ofori[4], Fanny Decarpentrie[8], Olivier Leupin[1,9], Fanning Zeng[1], Yufei Li[1], Claudia Merkl[1], Nicolau Beckmann[1], Sabine Guth-Gundel[1], Michaela Kneissel[1], Christian N. Parker[3] and Valerie S. Salazar[1]

[1] Novartis BR Diseases of Aging and Regenerative Medicine, Switzerland

[2] Novartis BR Diseases of Aging and Regenerative Medicine, USA

[3] Novartis BR Discovery Sciences, Switzerland

[4] Novartis Global Discovery Chemistry, USA

[5] Novartis BR CVM Biochemistry, USA

[6] Novartis BR Discovery Sciences, USA

[7] Novartis BR, Biologics Research Center, Switzerland

[8] Novartis In Vivo Sciences and Comparative Medicine, Switzerland

[9] Novartis Early Strategic Partnerships, Switzerland

Correspondence:

Valerie Salazar, Diseases of Aging and Regenerative Medicine, Novartis Pharma AG, Novartis Campus, CH-4056 Basel, Switzerland, valerie.salazar@novartis.com

Key words:

Tendon, Tenocyte, Achilles, Rotator cuff, Regeneration; Lysosomal Nutrient-Sensing; LAMTOR, Ragulator

Abstract

Despite decades of intense translational research on bone and cartilage, much remains unknown about enhancing tendon repair. To identify strategies for tendon regeneration, we immortalized multi-potent cells from embryonic limb buds of *Scx-gfp* mice. Clones with tenogenic potential were used to run genome-wide genetic screens to identify genes that regulate *Scx-gfp*. Pathway enrichment analysis uncovered a cluster of hits mapping to lysosomal nutrient sensing (LYNUS). Using Crispr-mediated gene ablation in 3 cell types from 3 species, we confirmed regulation of *Scx-gfp* by LYNUS pathway and a role for Ragulator and Rag GTPases in tenocyte differentiation and function. Molecular profiling of *Lamtor1-deficient* cells revealed profound shifts in autophagy and lipid metabolism that contribute to *Scx* induction and the chondrocyte/tenocyte cell fate decision through Gpnmb and cholesterol biosynthetic pathway. *In vivo*, *Lamtor1*$^{+/-}$ mice displayed improved repair of Achilles tendon injury as measured by tissue biomechanics and MRI. In rat rotator cuff, pharmacological inhibition of *Lamtor1* modulated LYNUS pathway and tenocyte gene expression but surprisingly lacked therapeutic effects on clinically-relevant phenotypes. Our work reveals a novel role for LYNUS in tenocyte biology and murine Achilles tendon repair while underscoring challenges in translating *in vitro* tenocyte biology to clinically meaningful pharmacological effects *in vivo*.

Introduction

Tendons are dense connective tissues that stabilize joints, transmit force between muscles and bones, and store energy for release during movement. The tissue biomechanical properties of tendon derive from a collagen-rich tissue composition organized along axes of biomechanical strain[1]. In contrast to bone which has a robust intrinsic capacity to repair throughout life[2], regeneration of mammalian tendon is restricted to early postnatal life[3]. Adult tendon healing typically proceeds by fibrotic scar-mediated repair rather than true regeneration, resulting in mechanically inferior tissue that may predispose the tendon to recurrent injury and degenerative tendinopathy[4].

Injuries and degeneration of rotator cuff or Achilles tendons are among the most common tendon-related conditions in musculoskeletal medicine. Many patients undergo surgical repair, but poor healing and re-tear remain common[1]. Clinically approved medicines to restore native tendon tissue structure and function remain unavailable, fueling a major unmet need in orthopedic and sports medicine. Clinically-approved regenerative agents for tendon, ligament, or tendon–bone healing could transform treatment for tendon injuries and disease in patients of all ages and activity levels.

The discovery of novel therapies is often rooted in intrinsic biology and supported by human genetics[5]. Vertebrate tendon biology and disease are strongly linked to TGFβ pathway[2,6-8]. Tendon-related phenotypes have been observed following perturbations of ligands such as *Tgfb2/3*[6] (MIM 614816; MIM 615582) or *Mstn*[9], the type I receptor *Alk5/Tgfbr1*[6,10] (MIM 609192), the type II receptor *Tgfbr2*[6,8] (MIM 610168), the intracellular mediators *Smads2/3/4*[6,10-13] (MIM 613795), and the matricellular modulator *Fbn1*[14,15] (MIM 154700). Tendon-related phenotypes related to BMP family molecules are also well annotated including pro-tenogenic activity by *Gdf5/6/7*[16-18], inhibition of tenocyte cell fate by Noggin[19], and activin-dependent conversion of tenocytes to bone-forming osteoblasts by FOP-associated mutations of the BMP receptor *Alk2/Acvr1*[20,21] (MIM 135100). Despite this robust evidence for a role for TGFβ/BMP pathways in tendon biology, the translation into treatments for tendon trauma or disease is hampered by myriad factors including the complex functional redundancy of signal transduction mechanisms, challenges in achieving target-selective small molecule inhibitors, the cost, formulation, and antigenicity hurdles associated with recombinant biologics, and safety risks associated with systemic modulation of

ubiquitous pathways. A broader understanding of the repertoire of mechanisms that govern the biology of tendon-resident cells could generate new testable hypotheses about how to activate tendon regeneration.

Tenocytes are mechanoresponsive tendon-resident fibroblasts responsible for building and repairing tendon throughout development and adult life[22]. During development, tenocytes of the appendicular skeleton emerge from lateral plate mesoderm and limb bud mesenchyme. Newly specified tenocytes express high levels of the bHLH transcription factor called *scleraxis* (*Scx*)[4,19], which continues to be expressed in mature tenocytes at varying levels throughout postnatal life[23-25]. Genetic studies in mice indicate that *Scx* is dispensable for tendon development but fundamental to adult tendon homeostasis[6,8,26]. *Scx-gfp* transgenic tenocyte reporter mice have greatly facilitated experimental tractability of tenocytes at single-cell resolution[27]. In 2017, the lab of Alice Huang reported that neonatal mice could repair an Achilles tendon rupture with native tendon-like tissue that was populated primarily by *Scx-gfp*+ cells[3]. By contrast, adult animals formed a fibrocartilage scar populated primarily by *Scx-gfp*- cells. Together, these observations sparked global interest to determine how *Scx*+ cells contribute to tendon repair. Identifying mechanisms that control the induction or regenerative capacity of Scx+ cells could help uncover new strategies to regenerate tendon and restore mobility to patients suffering from tendon injury and disease.

To interrogate this hypothesis at scale, we established a renewable source of *Scx-gfp* reporter cells by immortalizing multipotent mesenchymal cells from the embryonic limb bud[28] of *Scx-gfp* mice. Regulators of *Scx-gfp* were identified by Crispr-mediated genome-wide genetic screens. Many hits mapping to the TGF/BMP pathway were recovered in alignment with historical findings. Most hits, however, represented mechanisms not previously linked to tendon biology, including a large cluster of hits mapping to lysosomal nutrient sensing machinery (LYNUS)[29]. Using a comprehensive suite of assays in mouse, rat, and human cell models, we confirmed a previously unknown role for lysosomal nutrient sensing in tenocyte differentiation and function. By subsequently focusing on Lamtor1 as an essential representative component of LYNUS machinery, we generated insights on pleiotropic mechanisms underlying tenogenic effects of LYNUS pathway inhibition. We furthermore demonstrated that disruption of LYNUS through genetic ablation of a single copy of *Lamtor1* is sufficient to improve early tendon repair in a mouse model

of Achilles tendon injury. Intriguingly however, these collective observations failed to translate into improved healing of supraspinatus tendon in a pharmacological model of rat rotator cuff repair. Additional future work will be needed to determine if this surprising finding arises from differences in mechanisms that control tendon repair at distinct anatomical sites or can be overcome by an alternative therapeutic approach.

Results

CRISPR/Cas9 Screening Reveals Modulation of *Scx-gfp* by Lysosomal Nutrient Sensing Pathway

To identify regulators of *Scx-gfp*, we performed a pooled genome-wide CRISPR/Cas9 screen in mouse limb bud cells immortalized from E11.5 dpc *Scx-gfp* embryos (MLBCs) (Figure 1A). *Scx-gfp* expression is density-dependent. Screens were thus performed at low cell density or high cell density (Figure 1B), enabling identification of gene knockouts that enhance or suppress *Scx-gfp* expression (Table S1). Approximately 20,000 genes were targeted using up to five sgRNAs per gene. Consistent with literature documenting roles for TGF-beta and BMP pathways in tenocyte cell fate specification, downregulation of *Scx-gfp* was observed in multiple knockouts mapping to canonical TGFβ pathway (Figure S1A-B), while upregulation of *Scx-gfp* was observed in multiple knockouts mapping to canonical BMP pathway (Figure 1C-D). Pathway enrichment analysis of knockouts with reduced *Scx-gfp* expression revealed a strong relationship to proliferation, supporting our observation of cell density-dependent *Scx-gfp* expression and strategy to screen at low versus high cell densities (Figure S1E). Pathway enrichment analysis of knockouts with increased *Scx-gfp* expression revealed biological processes related to lysosomal function, nutrient sensing, and mTORC1 signaling (Figure 1C), including a cluster of genes encoding lysosomal-associated proteins involved in amino acid sensing (Figure S1F). Robust and highly significant upregulation of *Scx-gfp* expression was observed at both high and low density in many gene knockouts encoding proteins in lysosomal nutrient sensing (LYNUS) pathway (Figure 1D-E). Robust and highly significant downregulation of *Scx-gfp* expression was also observed at both high and low density in multiple gene knockouts of the nutrient sensing pathway (Figure S1G–H), including mTOR which has been previously linked to tendon biology[30]. Although initially appearing as a paradox, the combined set of hits demonstrate potent bi-directional regulation of *Scx-gfp* by positive and negative effectors of a common pathway based on lysosomal nutrient sensing and the related signal transduction networks (Figure 1F). To assess reproducibility, induction of *Scx-gfp* was confirmed in *Lamtor1* and *Lamtor4* knockout MLBCs via electroporation of sgRNA/Cas9 ribonucleoprotein complexes and flow cytometry (Figure 1G).

Genetic disruption of LYNUS Pathway Promotes Tenogenesis in 2D and 3D MLBC Models

To assess the impact of LYNUS pathway disruption on tenocyte differentiation, we generated *Lamtor1* and *Lamtor4* knockout MLBCs and evaluated their behavior across multiple *in vitro* differentiation assays.

Quantitative PCR and SCX-luciferase reporter assays confirmed elevated *Scx* transcription in *Lamtor1* KO MLBCs cultured in tenogenic medium (Figure 2A–B). Western blots validated increased Scx or GFP protein levels in *Lamtor1* KO or *Lamtor4 KO* cells (Figure 2C–D). Enhanced fibrillar collagen deposition was found by CNA35 staining on 2D cultures of *Lamtor4 KO* (Figure 2E-F) and 3D suspension spheroids of *Lamtor1* KO (Figure 2G–H) alongside increased *Scx- gfp* expression (Figure 2I).

Limb bud cells are a common progenitor to tenocytes, chondrocytes and osteoblasts. All three cell types can form and produce matrix in a tendon scar. To assess tendon-like tissue formation, MLBCs were embedded in 3D fibrin gels (Figure 2J) or rolled into mini-tissues (Figure 2L) and assembled on posts. When cultured in tenogenic medium, *Lamtor1* KO made more Sirius Red+ collagen than wild-type controls (Figure 2 K, M; Figure S2A–E). When cultured in endochondral medium, *Lamtor1* KO mini-tissues produced less Alcian Blue+ glycosaminoglycans-rich ECM characteristic of chondrocytes while maintaining increased collagen deposition (Figure 2N; Figure S2A-E). When cultured in osteogenic medium, *Lamtor1* and *Lamtor4* KO MLBCs produced less Alizarin Red+ calcified matrix characteristic of osteoblasts in micromass or 2D cultures (Figure 2O-P; Figure S2F–J). Together these findings provide evidence that genetic disruption of LYNUS promotes tenocyte differentiation across multiple platforms in MLBCs including 2D cultures, 3D spheroids, and engineered 3D tenoids, while concurrently suppressing alternative endochondral lineage programs.

Enhanced Tenogenesis After Genetic Disruption of LYNUS Pathway is Conserved Across 3 Species, 3 Cell Types, and Multiple LYNUS Protein Complexes

To eliminate the possibility that these effects were specific to Lamtor1/4 and/or MLBCs, we extended our analysis to primary rat tail tenocytes (RTTs) and immortalized human mesenchymal stem cells (hMSCs). We expanded to additional hits mapping to the Ragulator complex (*Lamtor1*, *Lamtor4*, *Lamtor2*) and Rag-GTPase dimer (*Rraga* and *Rragc*).

In 3D fibrin-based mini-tissues formed from primary RTTs, *Lamtor4* KO had significantly increased tissue diameter, force to failure, and hydroxyproline content compared to wild-type controls (Figure 3A–D). Similar enhancements were observed in RTT micro-tissues cultured on flexible hanging posts, where *Lamtor4* KO micro-tissues exhibited increased collagen deposition and greater tissue tension, as assessed by reduced post-to-post distance (Figure 3E–F). On flexible PDMS two-pillar devices, *Lamtor4* KO RTT tissues showed elevated collagen, a well-developed actin cytoskeletal network, and increased contractile force (Figure 3G–J). *Rragc* KO RTTs displayed increased collagen deposition in 2D (Figure 3K) and enhanced biomechanical properties in 3D mini-tissues including greater diameter, force to failure, and hydroxyproline content (Figure 3L–O). Enhanced *Scx* expression, collagen generation, and biophysical properties were observed across most experimental conditions tested in 2D and 3D RTT cultures of *Lamtor1* KO*, Lamtor2* KO*, Rraga* KO*, Wdr24* KO, and *Mios* KO (Figure S3A–I).

In immortalized hMSCs, *LAMTOR1* KO 3D micro-tissues showed greater deflection of anchor posts (Figure 3P–R). Immortalized hMSCs *LAMTOR4* KO micro-tissues also showed increased SCX expression by immunofluorescence and greater post deflection (Figure 3S–T). These findings were supported by increased *Scx* transcript and protein levels (Figure S3J–L), as well as increase of tenogenic markers like Tenomodulin or Tenascin in 2D cultures (Figure 3L-M), and elevated collagen deposition under 2D tenogenic conditions (Figure S3N–O). Macroscopic analysis of 3D hMSC micro-tissues confirmed increased size and tension in hMSCs *LAMTOR4* KO constructs (Figure S3P).

The combined results demonstrate enhanced tenocyte differentiation and tendon-like tissue assembly across diverse 2D and 3D models in mouse embryonic limb cells, primary rat tail tenocytes and human MSCs, supporting a conserved role for lysosomal nutrient sensing in tenogenesis.

***LAMTOR1* or *LAMTOR4* Deficiency Alters Lysosome, Lipid, and Calcium Homeostasis**

To explore broader cellular consequences of LYNUS disruption and gain insights on possible mechanisms impacting tenocyte cell fate or function, we performed multiparametric analysis with 41 fluorescent probes in *LAMTOR1* KO and *LAMTOR4* KO hMSCs. Altered staining patterns compared to wild-type were observed for NBD C6-ceramide, Bodipy FL C5 sphingomyelin, Bodipy FL C5-ganglioside GM1, Lysotracker Green, and a calcium indicator (Figure 4A). Quantitative image analysis confirmed significant

changes in dot count, intensity, and morphology, indicating increased lysosomal abundance and altered lipid trafficking/metabolic processes in *LAMTOR1* KO and *LAMTOR4* KO hMSCs (Figure 4B).

Activation of TFEB/Autophagy Programs by *Lamtor1* Deficiency Enhances Tenogenic Potential

Lysosomes are highly regulated by nutrient availability and growth factor signaling through mTORC1 signal transduction networks and MITF-family transcription factors. We assessed the functionality of nutrient sensing and coupling to mTORC1 activity in wild-type and *LAMTOR1* KO hMSCs (Figure 4C-D). Under nutrient-rich conditions, *LAMTOR1* KO hMSCs exhibited similar levels of phosphorylated S6 ribosomal protein (p-S6RP) levels compared to WT. Deprivation of non-essential amino acids (NE AA), essential amino acid (EAA), and serum markedly decreased p-S6RP in both genotypes; however, a greater reduction was observed in *LAMTOR1* KO hMSCs. Upon rescue with EAA, WT hMSCs rapidly recovered p-S6RP while *LAMTOR1* KO hMSCs did not. *LAMTOR1* is thus required for communicating levels of amino acids but not serum factors to the mTORC1/S6K axis (Figure 4C-D).

Western blot analysis revealed increased abundance of p62/SQSTM1, a marker of autophagic flux, in *LAMTOR1* or *LAMTOR4* KO hMSCs (Figure 4D, F-G) as well as *Lamtor1* or *Lamtor4* KO MLBCs (Figure S4A-B) cultured in normal growth medium. Western blot and immunofluorescence analysis further confirmed enhanced autophagic flux in *Lamtor1* KO or *Lamtor4* KO MLBCs via increased accumulation of p62 and LC3 upon inhibition of lysosomal degradation using Bafilomycin A or Chloroquine (Figure S4C-F). Consistent with increased lysosome abundance and p62, loss of *LAMTOR1* or *LAMTOR4* in hMSCs activated TFEB and TFE3, MITF-family transcription factors considered master regulators of lysosomal biogenesis and autophagy (Figures 4D-F and S4A). TFEB was also activated in *Lamtor1* KO MLBCs (Figure S4A). This correlated to increased expression of TFEB target genes *RRAGD* and SQSTM in *LAMTOR1* KO hMSCs (Figures 4G and S4A) as well as *Lamtor1* KO MLBCs (Figure S4G-J). Notably, altered signaling by lysosomal nutrient sensing machinery was not due to low levels of intracellular amino acids in *LAMTOR1* KO hMSCs (Figure S4K) or *Lamtor1* KO MLBCs (Figure S4L). In fact, MLBCs had increased levels of alanine, glutamate, and glutamine, and hMSCs had elevated glutamine levels.

We next compared the effects of genetic disruption of *Lamtor1* with pharmacological inhibition of mTOR. Treatment of WT MLBCs with the mTOR inhibitors Torin1 or Rapamycin (Figure S4O) led to a near-

complete loss of p-S6RP signal, confirming effective mTORC1 suppression. By contrast, *Lamtor1* or *Lamtor4* KO in MLBCs resulted in only a partial reduction of p-S6RP. Stimulation with IGF1 or TGF-β1 (Figure S4P) elicited robust mTORC1 activation in *Lamtor1* KO MLBCs comparable to wild-type controls.

Intriguingly, analysis of the proximal 1.5 kb of human *SCX* promoter uncovered multiple predicted transcription factor binding sites including SMAD-binding elements (SBEs) and E-box motifs recognized by TFEB and SREBP2 (Figure 4H). And the original screening data showed that knockouts of *Smad2*, *Smad3*, *Tfeb*, and *Srebf2* altered expression of *Scx-gfp* (Figure 4I). We therefore tested if TFEB affects tenocyte differentiation by overexpressing WT or constitutively active TFEB in MLBCs. QPCR analysis verified the transcriptional activity of TFEB by increased expression of *RragD* and *Gpnmb* (Figure 4J) and furthermore demonstrated induction of the tenocyte lineage markers *Scx* and *Dcn* (Figure 4K). Overexpression of constitutively active TFEB variants (TFEBmut and TFEBΔ30) in MLBCs also resulted in a notable increase in SCX protein levels, as confirmed by Western blot analysis (Figure 4L).

Together, these findings demonstrate that loss of *Lamtor1* leads to a perceived fasting state characterized by increased autophagy and TFEB/TFE3 activation. While *Lamtor1* is important for amino acid dependent mTORC1 signaling to S6K, it is dispensable for growth factor–mediated signaling from mTORC1 to S6K. And TFEB activation is sufficient to induce tenocyte lineage markers independently of *Lamtor1* deletion.

Regulation of Cholesterol Biosynthetic Pathway by *Lamtor1* Deficiency Favors Tenogenic over Chondrogenic Lineage

To gather further insights on potential mechanisms underlying tenogenic effects of LYNUS disruption, we performed proteomic and lipidomic profiling of MLBCs cultured in growth or tenogenic medium. Principal component analysis (PCA) of proteomic data revealed clear separation between *Lamtor1* KO and WT samples under both conditions (Figure S5A) and many differentially expressed proteins (Figure S5B-E, Table S2). Ingenuity Pathway Analysis (IPA) identified robust regulation of proteins involved in cholesterol biosynthesis and peroxisome function in *Lamtor1* KO MLBCs (Figures 5A-D).

Intriguingly, multiple knockouts of cholesterol biosynthesis genes modulated *Scx-gfp* expression in MLBCs (Figure 5E-F), whereas knockout of peroxisomal genes had no detectable effect on *Scx-gfp*

expression (Figure 5G-H). We therefore tested if cholesterol biosynthetic pathway is necessary for tenogenesis. Indeed, pharmacological inhibition of cholesterol biosynthetic pathway with Atorvastatin or Fluvastatin significantly reduced *Scx* expression in MLBCs cultured in 2D tenogenic conditions (Figure 5I-K). MLBC 3D mini-tissues cultured with Atorvastatin had decreased Scx and Collagen I protein levels (Figure 5K) with increased glycosaminoglycan accumulation enriched around cells with chondrocyte-like morphology (Figure 5L). Quite strikingly, ectopic chondrogenesis was observed by Alcian Blue staining of MLBC 3D mini-tissues cultured with MVD inhibitor, Zoledronic acid, Tolnaftate, Fluconazole, GGPS inhibitor, and Tipifarnib (Figure 5N). A visual of the cholesterol biosynthesis pathway highlights the comprehensive analysis of pharmacological targets tested (Figure S5F), supporting a role for cholesterol biosynthetic pathway in tenocyte cell fate and suggesting that induction of the pathway contributes to the tenogenic potential of *Lamtor1*-deficiency.

Given the robust alterations in proteins associated with cholesterol metabolism and peroxisomes, we performed comprehensive lipidomic profiling. Principal component analysis (PCA) revealed a clear separation between *Lamtor1* KO and WT MLBCs under both control and tenogenic conditions (Figure S6A). Quantitative analysis confirmed widespread changes in lipid class abundance in *Lamtor1* KO cells under both conditions (Figure 6B-C), including a marked decrease in oxidized fatty acids (OxFA), triglycerides (TG), free fatty acids (FA), ceramides (Cer), diacylglycerols (DG), lysophosphatidylethanolamine (LPE), and lysophosphatidylcholine (LPC). In contrast, levels of ether-linked phospholipids, specifically ether phosphatidylethanolamine (EtherPE) and ether phosphatidylcholine (EtherPC), were elevated (Figure S5C). Notably, intracellular cholesterol levels remained unchanged in both MLBCs and hMSCs, indicating that the observed lipidomic alterations were not associated with depletion of intracellular cholesterol content (Figure S5D-E).

Induction of GPNMB by *Lamtor1* Deficiency Favors Tenogenic over Chondrogenic Potential

Further analysis of the proteomics screen (Figure S5C-D) revealed robust upregulation of GPNMB (Figure S6A), a transmembrane glycoprotein, in *Lamtor1* KO MLBCs grown in both control and tenogenic conditions. Increased GPNMB was validated by Western blot and qPCR analyses (Figure S7B–C). To determine if GPNMB regulates tenogenesis, WT MLBCs were treated with recombinant human GPNMB,

which mimics the cleaved, soluble extracellular domain of the native protein with receptor-binding activity. Indeed, treatment with recombinant GPNMB significantly increased SCX-luciferase reporter activity with a magnitude greater than that of tenogenic cocktail containing ascorbic acid and TGF-β1, and similar to *Lamtor1* deficiency (Figure S7D). To assess the impact of GPNMB deficiency on tenocyte differentiation, we generated *Gpnmb* KO MLBCs. Compared to WT MLBCs, *Gpnmb* KOs grown in tenogenic medium showed poor induction of tenocyte differentiation markers including *Scx*, *Col1a2* and *Egr1* (Figure S7E), alongside increased expression of chondrogenic genes such as *Sox9* and *Col2a1* (Figure S7F), suggesting decreased control over tenocyte/chondrocyte cell fate decision. In 3D fibrin mini-tissues generated from *Gpnmb* KO cells compared to WT controls, decreased Sirius Red+ collagen content was observed alongside pockets of Alcian Blue+ matrix with cells of chondrocyte-morphology (Figure 6J). The data show a previously unknown role for GPNMB in tenocyte cell fate specification and differentiation and demonstrate how upregulation of GPNMB may contribute to the tenogenic effect of *Lamtor1*-deficiency.

Lamtor1 **Heterozygosity Enhances Achilles Tendon Healing in a Mouse Injury Model**

We next assessed Achilles tendon repair in mice lacking one copy of *Lamtor1* (*Lamtor1*$^{+/-}$) compared with age- and sex-matched wild-type littermate controls (*Lamtor1*$^{+/+}$). Global heterozygosity was selected based on observations of undesirable and uncontrollable events of germline deletion of a floxed *Lamtor* allele when crossed to *Scx-cre::GFP*[31] and poor recombination efficiency of a floxed *Lamtor* allele using Tamoxifen plus *Scx-creERT2*[3] (data not shown).

Biophysical and biomechanical parameters were measured before injury and two weeks after a surgically induced partial Achilles tendon tear (Figure 6A). Before surgery, adult male *Lamtor1*$^{+/-}$ and *Lamtor1*$^{+/+}$ mice showed comparable body weight (Figure 6B), ultrasound-based Achilles shear wave velocity (SWE, Figure 6C), and MRI-based Achilles T2* values (Figure 6D). Achilles tendons from male *Lamtor1*$^{+/-}$ mice also displayed largely normal baseline biomechanical properties, including cross-sectional area (Figure 6E), max load to failure (Figure 6F), Young's modulus (Figure 6G), and complex modulus (Figure 6H), although maximum load to failure was reduced (Figure 6F). After injury, males of both genotypes showed reduced body weight and Achilles SWE, increased Achilles MRI T2*, and decreased Young's and E* complex moduli, confirming that surgery had induced a tendinopathy-like phenotype characterized by

impaired tissue stiffness, strength, organization, and water content (Figure 6B-H). Ultrasound and MRI imaging did not reveal genotype-dependent healing differences in males. However, biomechanical testing showed that injured *Lamtor1*$^{+/-}$ tendons had statistically improved complex modulus (Figure 6H) indicating improved mechanical integrity and functional recovery in the physiological range of stress/strain. Trends for 15% improved tissue cross-sectional area (Figure 6E) and 23% Young's modulus (Figure 6G) were observed but did not reach statistical significance in our study with n=10 *Lamtor1*$^{+/-}$ mice. Subsequent statistical analysis predicted a sample size of 24 in each group would have 80% power to detect a difference in means of -13.211 (the difference between a Group 1 mean, μ_1, of 74.889 and a Group 2 mean, μ_2, of 88.1) assuming that the Group 1 standard deviation, σ_1, is 18.964 and the Group 2 standard deviation, σ_2, is 11.606 (ratio of Group 2 to Group 1 standard deviation is 0.612) using a two group Satterthwaite t-test with a 0.05 two-sided significance level (Table S3).

A similar assessment was conducted in females (Figure 6I). Before surgery, adult female *Lamtor1*$^{+/-}$ mice had similar weight, imaging and biomechanical phenotypes as age- and sex-matched *Lamtor1*$^{+/+}$ littermates (Figure 6J-P). After injury, females of both genotypes had reduced body weight and Achilles SWE, increased Achilles MRI T2*, and decreased Young's and E* complex moduli, confirming that surgery had induced a tendinopathy-like phenotype characterized by impaired tissue stiffness, strength, organization, and water content (Figure 6J-P). While ultrasound did not reveal genotype-dependent differences in SWE (Figure 6K), biomechanical testing showed that injured *Lamtor1*$^{+/-}$ tendons showed statistically-significant improvements in tendon cross-sectional area (Figure 6M) and E* complex modulus (Figure 6P) indicating improved mechanical integrity and functional recovery in the physiological range of stress/strain. A trend for 23% improved Young's modulus (Figure 6G) was observed but did not reach statistical significance in our study with n=11 *Lamtor1*$^{+/-}$ mice. Subsequent statistical analysis predicted a sample size of 19 in each group would have 80% power to detect a difference in means of -16.476 (the difference between a Group 1 mean, μ_1, of 55.979 and a Group 2 mean, μ_2, of 72.455) assuming that the Group 1 standard deviation, σ_1, is 20.508 and the Group 2 standard deviation, σ_2, is 12.895 (ratio of Group 2 to Group 1 standard deviation is 0.628) using a two group Satterthwaite t-test with a 0.05 two-sided significance level (Table S3).

Together, we demonstrate that *Lamtor1* heterozygosity is sufficient to modestly but significantly enhance clinically-meaningful aspects of Achilles tendon healing in the first two weeks after injury. These findings suggest that even partial inhibition of Lamtor1 by a pharmacological inhibitor could have therapeutic effects on tendon healing after injury.

In vivo **pharmacological inhibition of** ***Lamtor1*** **modulates LYNUS pathway and activates tenocyte gene expression but lacks therapeutic effects in a rat model of rotator cuff injury**

Rotator cuff repair was evaluated in age- and weight-matched female rats for up to five weeks after a surgically induced partial supraspinatus tendon tear. One week after surgery, a single injection of *Lamtor1* siRNA (0.5mg/20uL) or vehicle control (20uL) was injected into the sub-acromial space (Figure 7A). QPCR was performed on injured/treated supraspinatus tendons versus healthy/non-treated contralateral control tendons at 7 and 14 days post-treatment (14 and 21 days post-surgery). *Lamtor1* expression was unaffected by surgery but robustly inhibited by local application of *Lamtor1* siRNA at both timepoints indicating local, efficient, and durable pharmacological inhibition of *Lamtor1* mRNA at the site of injury and treatment (Figure 7B,E). Consistent with *in vitro* observations of LYNUS disruption in *Lamtor1* KO cells (Figure 4D-F and S4B), pharmacological inhibition of *Lamtor1* led to robust induction of the TFEB target gene *Gpnmb*, which emerged earlier and with greater magnitude than in injured tendons treated with vehicle (Figure 7C,E). Consistent with *in vitro* observations of tenocyte induction in *Lamtor1* KO cells (Figure S3M), pharmacological inhibition of *Lamtor1* led to robust induction of the tenocyte differentiation marker *Tnc*, which emerged earlier and with greater magnitude than in injured tendons treated with vehicle (Figure 7D,G).

After injury, supraspinatus tendons exhibited increased MRI values for T2 and T2* (Figure 7H-I), histological expansion of the peritendon (Figure 7J), increased tendon cross-sectional area (Figure 7K), increased Max Load to failure (Figure 7L), and decreased Young's and E* complex moduli (Figure 7M-N), confirming that surgery had induced a tendinopathy-like phenotype characterized by impaired tissue morphology, stiffness, organization, and water content. Despite the robust tenogenic effects of *Lamtor1*-deficiency observed via comprehensive *in vitro* cell-based modeling, the enhanced Achilles tendon repair observed in *Lamtor1*-heterozygous mice, and robust sustained pharmacological inhibition of *Lamtor1*

here in supraspinatus tendon using siRNA, no therapeutic effects on supraspinatus tendon healing were observed as assessed in this particular preclinical paradigm (Figure 7H-N).

DISCUSSION

We demonstrate a previously unknown role for lysosomal nutrient sensing (LYNUS) in tenocyte cell fate and function and a specific role for *Lamtor1* in mouse Achilles tendon repair. Our work was enabled by *de novo* generation of immortalized tenocyte progenitors from the well-characterized *Scx-gfp* reporter mice. We performed CRISPR/Cas9 genetic perturbations at scale, confirming robust recovery of known regulators of *Scx,* and uncovering novel regulators mapping to lysosomal nutrient sensing machinery. Roles for components of the Ragulator and Rag-GTPase dimer in tenocyte differentiation and function were validated across multiple *in vitro* systems including 2D cultures and 3D tendon mini-tissues using 3 cell types from human, mouse, and rat origin. High-resolution profiling platforms were applied to identify the pleiotropic biological and molecular mechanisms underlying enhanced tenogenesis in *Lamtor1*-deficient cells. Enhanced Achilles tendon repair was demonstrated using *Lamtor1* heterozygous mice. And finally, we developed injectable *Lamtor1* siRNA to assess the translational potential of these findings using a pharmacological model of rat rotator cuff repair.

In vitro models to study tenocyte cell biology remain limited. The most widely used systems include primary tenocytes[32], tendon-derived stem/progenitor cells[33], and bone marrow-derived MSCs[34]. While biologically relevant, factors such as rapid phenotypic drift, limited proliferation potential, and low amenability to genetic perturbations make these systems difficult to combine with scalable approaches for functional genomics. In 1994, the Genetics Institute research group of Vicki Rosen and John Wozney used clonal limb bud cell lines from E13.5 d.p.c. mouse embryos to demonstrate that BMP-2 initiates the differentiation of uncommitted progenitors to bone and cartilage lineages[28], enabling the validation of recombinant BMP2 for clinical bone repair. Here, we generated limb bud cells from E11.5 d.p.c. embryos of the widely used *Scx-gfp* reporter line to identify and validate novel genes that govern tenocyte lineage.

The role for lysosomal nutrient sensing in tenocyte biology and Achilles tendon repair is not previously described. Our findings thus expand the current paradigm, which primarily focuses on transcriptional regulators such as Scx, Mkx, and Egr1[23,35-38], mechanical cues[39], or TGFβ/BMP pathways (summarized in Introduction). Using a comprehensive suite of *in vitro* assays and multiple cell types, our work showed that genetic disruption of LYNUS through ablation of *Lamtor1* or *Lamtor4* enhances *Scx* expression,

collagen deposition, and tendon-like tissue assembly *in vitro*. With a variety of high-resolution phenotypic profiling methods, we provided evidence that the cellular and molecular mechanism underlying tenogenic effects of *Lamtor1* ablation are not simple and linear but complex and pleiotropic. Notably, our work also clearly demonstrated that loss of *Lamtor1* impairs amino acid response but does not block mTORC1/S6K response to growth factors. More specifically, despite attenuated nutrient-dependent mTORC1 signaling, *Lamtor1*-deficient cells retained the ability to transduce IGF1 and TGF-β1 signaling through the mTOR/S6K axis. In our systems, loss of *Lamtor1* is therefore not equivocal to mTOR inhibition.

Lamtor1 ablation was also found to drive a profound shift in lipid metabolism. This is consistent with the known role for the Ragulator complex (including LAMTOR1-5) as a scaffold that integrates amino acid and cholesterol sensing at the lysosome via interactions with SLC38A9 and LYCHOS (GPR155)[40,41]. The link between the Ragulator and lipid metabolism is still underexplored and may have important future implications for translational metabolic regulation research. In the context of tenogenesis, we provide evidence that inhibition of cholesterol biosynthetic pathway disrupts control over the tenocyte/chondrocyte cell fate decision. Notably, statins, which inhibit a key step in the cholesterol biosynthetic pathway, are speculated to promote tendinopathies and risk of tendon rupture. And tendon xanthomas characterized by depots of excess cholesterol and activated fibroblasts are a hallmark of clinical hypercholesteremia[42-45]. These collective observations suggest that tight control over cholesterol metabolism could be important for tendon formation, physiology and repair.

In mice, heterozygous loss of *Lamtor1* improved clinically-relevant aspects of Achilles tendon repair including tissue morphology, biomechanical integrity, and non-invasive MRI-based diagnostics of disease pathology state. The application of MRI is not yet widely used to for phenotypic analysis of mouse tendon repair. The relationship observed between MRI and tissue biomechanics is valuable as biomechanical assessment is not feasible as a clinical endpoint and further investigation of surrogates is thus needed by the broader community to improve translational research.

This work was limited by challenges in generating mice with conditional *Lamtor1* deletion in the tenocyte lineage. Crossing a *Lamtor1-flox* allele with *Scx-cre::gfp*[31] frequently caused germline deletion, resulting in mixed litters with variable embryonic lethality, adults with body-wide *Lamtor1* mosaicism, and

progressive loss of the floxed allele across breeding generations. Crossing the *Lamtor1-flox* allele with *Scx-creERT2*[3] also proved insufficient as utilization of the LSL-tdTomato reporter showed the maximum tolerated dose of tamoxifen mediated recombination in less than half of resident Achilles tendon cells. For these reasons, we generated global heterozygotes from the *Lamtor1* flox strain, as described in the Methods, and found that this approach produced phenotypes consistent with our comprehensive *in vitro* findings. New *in vivo* genetic tools could support future studies of conditional *Lamtor1* deletion in tenocyte progenitors. In particular, Cre drivers that act prior to the Scx+ cell-state transition would better align with our screen which focused on identifying mechanisms preceding *Scx-gfp* expression. The nature and magnitude of preclinical phenotypes in mice that faithfully predict clinical translation also remain unknown.

Additional work could also help clarify whether pharmacological optimizations such as dose-escalation or longer treatment times could uncover therapeutic effects of Lamtor1 inhibition in rotator cuff injury. Alternatively, pharmacological inhibition of other LYNUS pathway components may provide better leverage to induce tendon repair in preclinical models and clinical orthopedic settings. This large undertaking is well-supported by our data package but falls beyond the scope of this present work.

In summary, novel cell models and methods were used to identify and validate a previously unknown role for LYNUS pathway in tenocyte biology and tendon repair. Future work will elucidate whether this can be successfully translated into novel therapies for tendon repair through modulation of *Lamtor1* or another component in the common underlying mechanism.

Figure legends

Figure 1. A genome-wide Crispr/Cas9 screen reveals potent regulation of *Scx-gfp* by the lysosomal nutrient sensing pathway.

(A) Experimental workflow of a pooled genome-wide Crispr/Cas9 screen performed in immortalized *Scx-gfp* mouse limb bud cells (MLBC) grown in MLBC growth medium. In total, 20,000 genes were targeted with ≤5 sgRNA guides/gene. Figure created with BioRender.com. **(B)** Schematic of the screening strategy. *Scx-gfp* MLBC were screened at low cell density (with low basal GPF expression) or high cell density (with high basal GFP expression) to identify gene knockouts that decrease or increase *Scx-gfp* expression. Figure created with BioRender.com. **(C)** Top 7 significantly enriched Reactome pathways among genes upregulated in the low-density condition. Pathway enrichment was assessed using a hypergeometric test. Count represents the number of genes from each pathway found in the low-density upregulated gene set. GeneRatio indicates the proportion of genes in the hit list that are part of the respective pathway. p.adjust denotes the adjusted p-value, reflecting the statistical significance of enrichment after correcting for multiple testing, based on comparison to the background gene set used in the screen. **(D-E)** Scatter plots showing the effects of selected gene knockouts in the lysosomal nutrient sensing (LYNUS) pathway on *Scx-gfp* expression during the (D) low cell density screen or (E) high cell density screen. **(F)** Schematic representation of individual proteins and complexes comprising the core LYNUS machinery and its extended regulatory network. Hits from the pooled CRISPR/Cas9 screen in *Scx-gfp* MLBCs are highlighted in red. Figure created with BioRender.com. **(G)** *Scx-gfp* MLBC were electroporated with sgRNA/Cas9 ribonucleoprotein complexes to generate *Lamtor1* KO or *Lamtor4* KO cells. Flow cytometry confirmed that *Scx-gfp* expression was induced by individual gene knockouts, consistent with results from the pooled screen.

Figure 2: Genetic disruption of the LYNUS machinery enhances *in vitro* tenogenesis in mouse embryonic limb bud cells.

(A) Quantitative PCR analysis in MLBCs (WT and *Lamtor1* KO) normalized to *Rps18* (n=3; mean ± std; multiple unpaired t-test). **(B)** Relative luminescence in MLBCs transfected with an *SCX*-luciferase reporter plasmid (100 ng) and treated for 48 hours with MLBC tenogenic medium (DMEM, 10%FBS, 1%

Pen/Strep, 50ug/ml Ascorbic Acid, 1ng/ml TGF-β1) (n=3; mean ± std, two-way ANOVA). **(C-D)** Western blot analysis of whole-cell lysates from MLBCs (WT or *Lamtor1* KO or *Lamtor4 KO*; n=3) treated with MLBC growth medium. Ponceau S staining was used to confirm equal protein loading. **(E-F)** MLBCs (WT and *Lamtor4* KO) were differentiated for 3 days in MLBC growth medium (GM), GM plus 50 μg/mL ascorbic acid (AA), or GM plus AA and 10 ng/mL TGF-β1 (tenogenic medium, AA + TGF-β1). Fibrillar collagen was stained with Alexa 555-conjugated CNA35 (orange) and nuclei with Hoechst (blue) (n=4; mean ± std; two-way ANOVA). **(G)** MLBCs (WT, *Lamtor1* KO, and *Lamtor4* KO) were cultured as suspension spheroids for 8 days. Fibrillar collagen was stained with Alexa 555-conjugated CNA35 (pink), *Scx*-GFP was visualized (green), and nuclei were counterstained with Hoechst (blue). **(H–I**) Quantification of **(H)** collagen deposition (CNA35 fluorescence) and **(I)** *Scx*-GFP expression in **(G)** suspension spheroids grown in MLBC control or tenogenic medium (n=4-18, mean ± std, two-way ANOVA). **(J)** Schematic of 3D fibrin-based mouse tendon mini-tissues. MLBCs were seeded in fibrin gels, self-assembled into 3D structures, and differentiated for 13 days in MLBC tenogenic medium. Figure created with BioRender.com. **(K)** MLBC 3D fibrin mini-tissues (WT or *Lamtor1* KO) were cultured in tenogenic medium for 13 days. Fibrillar collagen was stained with Sirius Red and imaged under brightfield (BF) and polarized light, and quantified (n=3-4; mean ± std; unpaired t-test, scale bar = 100 μm). **(L)** Schematic representation of 3D rolled mouse tendon mini-tissues. MLBCs were expanded in 2D in MLBC growth medium, then cultured for 5 days in MLBC tenogenic medium to stimulate ECM deposition. Cell layers were rolled into 3D structures, pinned, and further differentiated in MLBC tenogenic medium for 13 days. Figure created with BioRender.com. **(M)** MLBC 3D rolled mini-tissues (WT or *Lamtor1* KO) were cultured in tenogenic medium for 18 days. Fibrillar collagen was stained with Sirius Red, imaged under brightfield (BF) and polarized light, and quantified (n=4; mean ± std; unpaired t-test, scale bar = 100 μm. **(N)** MLBC 3D rolled mini-tissues (WT or *Lamtor1* KO) were cultured in MLBC tenogenic medium (DMEM, 10% FBS, 1% Pen/Strep, 50 μg/mL AA, 10 ng/mL TGF-β1, left) or in endochondral medium (DMEM, 10% FBS, 1% Pen/Strep, 50 μg/mL AA, 100 nM dexamethasone, 40 μg/mL L-proline, 1 mM sodium pyruvate, ITS supplement, right) and co-stained with Picro Sirius Red and Alcian Blue. Scale bar = 100 μm. **(O)** MLBCs (WT, *Lamtor1* KO or *Lamtor4* KO) were cultured as adherent micromasses in osteogenic medium (DMEM, 10% FBS, 1% Pen/Strep, 50 μg/mL AA, 10 mM β-glycerophosphate, 200 ng/mL BMP-2) for 10

478 days. Calcified matrix was stained with Alizarin Red (n=3). **(P)** MLBCs (WT, *Lamtor1* KO or *Lamtor4* KO)
479 were cultured in 2D in osteogenic medium and stained with Alizarin Red after 4, 6, or 10 days (n=3).
480 Statistical significance: *p<0.05, **p<0.01, ***p<0.001, ****p<0.0001.

481 **Figure 3: Genetic disruption of LYNUS machinery enhances *in vitro* tenogenesis in primary rat**
482 **tenocytes and immortalized human MSCs.**

483 **(A)** Schematic representation of 3D fibrin-based rat tendon mini-tissues. Primary rat tail tenocytes (RTT;
484 WT or *Lamtor4* KO) were seeded into fibrin gels that self-assembled into 3D structures and differentiated
485 for 7 days in RTT DMEM/F12 tenogenic medium (DMEM/F12 plus 20% FBS, 1% MEM NEAA, 0.1% β-
486 mercaptoethanol, 1% Pen/Strep, 50 µg/mL ascorbic acid, and 5 ng/mL TGF-β1) tested by biomechanics.
487 Figure created with BioRender.com. **(B–D)** Biomechanical analysis of RTT mini-tissues: **(B)** Diameter (n =
488 8–11), **(C)** Force to failure (n = 7–11), **(D)** Hydroxyproline content normalized to DNA (n = 9–11). Data are
489 shown as mean ± standard deviation, analyzed using unpaired t-tests. **(E)** Schematic of 96-well 3D micro-
490 tissues formed on flexible hanging posts (stiff posts: k = 0.51 kN/µm; soft posts: k = 0.051 kN/µm). RTTs
491 (WT or *Lamtor4* KO) were seeded into fibrin gels and differentiated for 7 days in RTT DMEM/F12
492 tenogenic medium. Figure created with BioRender.com. **(F)** RTT micro-tissues seeded on stiff posts were
493 stained for fibrillar collagen using Alexa 555-conjugated CNA35 (orange, left). Quantification of post-to-
494 post distance was used as a surrogate for tissue tension (right). **(G-J)** RTT micro-tissues grown on
495 flexible PDMS two-pillar devices (k = 11.1 µN/µm), differentiated for 4 days in RTT DMEM/F12 tenogenic
496 medium. Figure created with BioRender.com. **(H)** Second harmonic generation imaging of RTT micro
497 tissues grown on flexible PDMS two-pillar devices. Collagen (green) with F-actin counterstaining (purple).
498 Scale bar = 500 µm. **(I)** Quantification of collagen (n=8, mean ± std, unpaired t-test). **(J)** Contractile force
499 (µN) calculated from post deflection and stiffness (n=5-8; mean ± std, unpaired t-test). **(K)** RTTs (WT or
500 *RragC* KO) were differentiated in 2D in RTT DMEM/F12 tenogenic medium. Fibrillar collagen was imaged
501 and quantified using Alexa 555-CNA35 and Hoechst. Each data point represents one well with nine fields
502 per well (n = 3 per timepoint). **(L)** Representative images of RTTs (WT or *RragC* KO) grown as 6-well 3D
503 mini-tissues in RTT DMEM/F12 tenogenic medium. **(M-O)** RTT 3D mini-tissues (WT or *RragC* KO) were
504 cultured for 7 days in RTT DMEM/F12 tenogenic medium and analyzed for: **(M)** Diameter (n = 2–5), **(N)**

Force to failure (n = 3–4), **(O)** Hydroxyproline content normalized to DNA (n = 5). Data are shown as mean ± standard deviation, analyzed using unpaired t-tests. **(P-T)** 3D human immortalized MSC tendon micro-tissues formed on flexible hanging posts (WT or *LAMTOR1* KO), seeded in fibrin gels and differentiated for 7 days in hMSC standard growth medium. **(P)** Representative images at day 12 post-plating (left) and quantification of post-to-post distance over time (4–12 days; n = 4; two-way ANOVA). **(Q)** Diameter of hMSC micro-tissues (WT vs. *LAMTOR1* KO day 8 soft = ****, day 11 soft = ***, day 12 soft = ***; day 8 stiff = ****, day 11 stiff = **, day 12 stiff = *). **(R)** Relative post deflection of hMSC micro-tissues grown on soft or stiff posts (WT vs. *LAMTOR1* KO day 8 soft = *, day 11 soft = ****, day 12 soft=****; day 8 stiff= ns, day 11 stiff = ns, day 12 stiff = ns); (1-12 days, n = 4–8; two-way ANOVA). **(S)** Representative immunostaining and quantification of SCX (yellow) and nuclei (blue, DAPI) in hMSC micro-tissues (WT or *LAMTOR4* KO) grown in hMSC basal medium plus 50 µg/mL AA (control) or primed 2 days with 1 ng/mL TGF-β1 before plating in 3D (primed tenogenic) on soft posts for 12 days (n = 3–4; two-way ANOVA). **(T)** Relative post deflection of hMSC micro-tissues (WT or *LAMTOR4* KO; n = 3) grown on soft posts for 12 days in hMSC basal medium (Ctrl) or primed for 2 days with 1 ng/mL TGF-β1 before plating in 3D (Primed Tenogenic); (WT vs. *LAMTOR4* KO day 8 soft = ns, day 11 soft = ****, day 12 soft =****; day 8 Primed = ***, day 11 Primed = ns, day 12 Primed = ns). Significance: *p<0.05, **p<0.01, ***p<0.001, ****p<0.0001.

Figure 4: *Lamtor1-deficient* cells perceive amino acid deprivation leading to induction of autophagy and activation of TFEB.

(A) Fluopack screening of immortalized human MSCs (WT, *LAMTOR1* KO, or *LAMTOR4* KO). using 41 fluorescent probes. Representative images of the top five probes (green signal) are shown: NBD C6-ceramide, Bodipy FL C5 sphingomyelin, Bodipy FL C5-ganglioside GM1, Lysotracker Green, and Calcium Indicator. Nuclei were counterstained with Hoechst (blue). Scale bar as indicated. **(B)** Quantitative analysis of the top five probes presented as violin plots, including measurements of branching points, dot count per cell, cell body mean intensity, dot mean intensity, and average dot diameter. (6 replicates, 6 fields per well, n=300-500 cells, mean ± std, ordinary one-way ANOVA). **(C)** Immortalized human MSCs (WT and *LAMTOR1* KO) were deprived of FBS and amino acids for 1 hour (starvation), then reconstituted with indicated nutrients (starvation, non-essential amino acids = NEAA, essential amino acids = EAA) for

1 hour, all under standard nucleotide levels. Cells were stained for phospho-S6 ribosomal protein (p-S6RP; red) and nuclei with Hoechst (blue). Scale bar = 200 µm. **(D)** Western blot analysis of whole-cell lysates from hMSCs (WT, *LAMTOR1* KO; n = 3)**.** *GAPDH* (hMSCs) was used to verify equal protein loading. **(E)** Representative immunofluorescence images of immortalized hMSCs (WT, *LAMTOR1* KO, *LAMTOR4* KO) stained for TFEB (red) and nuclei (blue, Hoechst). Scale bar = 200 µm. **(F)** Immortalized human MSCs (WT, *LAMTOR1* KO, *LAMTOR4* KO) were cultured in hMSC basal medium (MSCBM® Basal Medium and MSCGM® SingleQuots® Supplement Kit Lonza) and stained for TFE3 (left) or p62 (right) using immunofluorescence (red). Nuclei were counterstained with Hoechst (blue). Quantification of TFE3 and p62 signal is shown on the right. Scale bar = 200 µm. (n=2, mean ± std, ordinary one-way ANOVA). **(G)** Western blot analysis of whole-cell lysates from immortalized hMSCs (WT, *LAMTOR1* KO, *LAMTOR4* KO; n = 3) cultured in hMSC basal medium. GAPDH was used to verify equal loading. **(H)** Schematic representation of the 1.5 kb human *SCLERAXIS* (*SCX*) proximal promoter with predicted transcription factor binding sites. Smad-binding elements (SBEs) are marked in orange, and E-box motifs recognized by SREBP2/TFEB are marked in pink. **(I)** Results from CRISPR/Cas9 screen for genes encoding proteins that can bind to SBEs and E-box binding motifs predicted in **(H)**. Each data point represents effects of a unique guide RNA on *Scx-gfp* expression (fold change) upon gene knockout at high cell density (HCD) or low cell density (LCD) and corresponding controls. **(J)** Quantitative PCR analysis of TFEB target genes (*RagD*, *Gpnmb*) and **(K)** tenogenic markers (*Scx*, *Dcn)* expression in MLBCs (WT) transfected with control plasmid (pcDNA3.1), TFEB plasmid, or TFEB mutant plasmid. Cells were cultured in MLBC control medium (DMEM, 10% FBS, 1% Pen/Strep, 50 µg/mL AA or MLBC tenogenic medium (DMEM, 10% FBS, 1% Pen/Strep, 50 µg/mL AA , and 1 ng/mL TGF-β1). (n= 3; relative mean ± std; 2-way ANOVA). **(L)** Western blot analysis of whole-cell lysates from MLBCs (WT, n = 3) transfected with the described plasmids (control plasmids: pcDNA, mScarlet; Tfeb, Tfeb mut (active), Tfeb Δ30 (active)) and cultured for 1 day in control or tenogenic medium. Ponceau S staining was used to confirm equal protein loading.

Figure 5: *LAMTOR1*-deficient cells exhibit a profound shift in cholesterol metabolism which independently regulates tenocyte versus chondrocyte lineage allocation.

(A-B) Ingenuity Pathway Analysis (IPA) of proteomics data from MLBCs (WT, *Lamtor* KO) cultured for 4 days in either **(A)** MLBC growth medium (DMEM, 10% FBS, 1% Pen/Strep; blue) or **(B)** MLBC tenogenic medium (DMEM, 10% FBS, 1% Pen/Strep, 50 µg/mL AA, and 10 ng/mL TGF-β1; orange). Bar plots represent z-scores; red dots indicate p-values (n = 3). **(C-D)** Volcano plots of proteomics analysis on MLBC highlighting components of cholesterol biosynthesis and peroxisomal pathways after 4 days of culture in **(C)** MLBC growth medium (blue) or **(D)** MBLC tenogenic medium (orange). **(E-H)** Scatter plots showing the effects of selected gene knockouts in the cholesterol biosynthesis pathway **(E-F)** or the peroxisomal pathway **(G-H)** on *Scx-gfp* expression at **(E, G)** low or **(F, H)** high cell density screening conditions. **(I-J)** Quantitative PCR analysis of *Scx* expression in MLBCs (WT) treated with 1 µM Atorvastatin or 1 µM Fluvastatin for 3 days in MLBC tenogenic medium. (n=3, mean ± std, unpaired t-test). **(K)** Representative immunofluorescence images of MLBC 3D fibrin mini-tissues stained for *Scx* (orange, left) or Collagen I (orange, right), plus nuclei counterstaining using DAPI (blue). Tissues were cultured for 7 days in tenogenic medium and subsequently treated for 7 days with or without 1 µM Atorvastatin. Scale bar = 100 µm. **(L)** Representative images of MLBC 3D fibrin mini-tissues on day 14, following 7 days in tenogenic medium and 7 days with or without 1 µM Atorvastatin. Tissues were co-stained with Alcian Blue (glycosaminoglycans, blue) and Picro Sirius Red (collagen, pink). Scale bar = 200 µm. **(M)** Representative images of MLBC 3D fibrin mini-tissues on day 14, treated for 7 days with tenogenic medium and an additional 7 days with either 1 µM Atorvastatin, MVD inhibitor, Zoledronic acid, Tolnaftate, Fluconazole, GGPS inhibitor, or Tipifarnib (n = 3). Scale bar = 50 µm. Statistical significance: *p<0.05, **p<0.01, ***p<0.001, ****p<0.0001.

Figure 6: Lamtor1 global heterozygous mice show improved healing of Achilles tendon partial tear

Schematic representation of a mouse Achilles tendon injury model performed on **(A)** male or (**I)** female wild-type (*Lamtor1*$^{+/+}$, n=20) or global heterozygous *Lamtor1* knockout mice (*Lamtor1*$^{+/-}$, n=11). Body weight as a function of time relative to Achilles tendon injury in males **(B)** or females **(J)**. Quantification of Achilles tendon shear wave velocity by ultrasound SWE imaging in males **(C)** or females **(K)**. Quantification of Achilles tendon T2* relaxation time by MRI in males **(D)** or females **(L).** Biomechanical analysis of healthy and injured Achilles tendons at 2 weeks post-injury in males **(E-H)** and females **(M-P)**:

(E, M) Cross-sectional area, **(F, N)** max load to failure, **(G, O)** Young's modulus, and E* Dynamic Modulus **(H, P)**. All data are presented as mean ± standard deviation (n = 11–20), analyzed using two-way ANOVA. Group sizes: WT healthy = 16–17, WT injured = 18–20, KO healthy = 10, KO injured = 10–11. Statistical significance: *p<0.05, **p<0.01, ***p<0.001, ****p<0.0001.

Figure 7: Local pharmacological inhibition of Lamtor1 induces potent transcriptional response to LYNUS inhibition and tenocyte activation but lacks therapeutic effects on clinically-relevant phenotypic endpoints in a rat model of rotator cuff injury.

(A) Schematic representation of a rat supraspinatus tendon injury model performed on age- and weight-matched female Sprague Dawley rats. **(B-G)** Quantitative PCR analysis on supraspinatus tendon at day 14 **(B-D)** or day 21 **(E-G)** after a surgical supraspinatus tendon injury and day 7 **(B-D)** or day 14 **(E-G)** after a single subacromial injection of Lamtor1 siRNA or saline control. Data are expressed as mean ± standard deviation relative to supraspinatus tendon from healthy contralateral control shoulders in the same animals. **(H)** Quantitative MRI-based analysis of supraspinatus tendon T2 or **(I)** T2* relaxation time**.** **(J)** Histological analysis by H&E staining of formalin-fixed paraffin-embedded sections of rat rotator cuff tissue prepared 28 days after surgery (21 days after single sub-acromial injection of saline vehicle or *Lamtor1* siRNA). **(K-N)** Biomechanical analysis of healthy and injured supraspinatus tendons at 4 weeks post-injury: **(K)** Cross-sectional area, **(L)** max load to failure, **(M)** Young's modulus, and **(N)** E* Dynamic Modulus. All data are presented as mean ± standard deviation, analyzed using two-way ANOVA. Group sizes: Healthy non-treated n≤18, injured + vehicle n≤9, injured + Lamtor1 siRNA n≤9. Statistical significance: *p<0.05, **p<0.01, ***p<0.001, ****p<0.0001.

SUPPLEMENTARY FIGURE LEGENDS

Figure S1

(A-D) Waterfall plots from the CRISPR/Cas9 screen showing the effects of gene knockouts in TGFβ/BMP pathway on *Scx-gfp* expression in MLBCs. **(A, C)** Downregulation of *Scx-gfp* by selected gene knockouts at low **(A)** and high **(C)** cell density. **(B, D)** Upregulation of *Scx-gfp* by selected gene knockouts at low **(B)** and high **(D)** cell density. **(E)** Pathway enrichment analysis of the CRISPR/Cas9 screen in MLBCs cultured in MLBC growth medium (DMEM supplemented with 10% FBS, 1% Pen/Strep), presented as a dot plot illustrating biological pathways significantly enriched among gene knockouts that reduced *Scx-gfp* expression. **(F)** Protein–protein interaction network of hits comprising the top 7 enriched Reactome pathways (as defined by KOs that upregulate *Scx-gfp* at low density). The network was generated using STRING-db and includes all genes associated with these pathways. Nodes represent genes, and edges indicate predicted or known interactions. Line color reflects the type of interaction evidence (e.g., experimental, database, co-expression). Genes highlighted in red are localized to the lysosome, while those in blue are involved in amino acid–regulated mTORC1 signaling. **(G-H)** Waterfall plots from the CRISPR/Cas9 screen showing effects of selected knockouts on *Scx-gfp* at low (G) or high (H) cell density, highlighting genes that are part of the amino acid–dependent mTORC1 activation gene cluster.

Figure S2

(A) Picro Sirius Red (collagen content) and Alcian Blue staining (glycosaminoglycan content) co-staining of MLBC 3D rolled mini-tissues (WT, *Lamtor1* KO). Representative images on day 22, treated for 8 days in 2D culture and 14 days in 3D culture in either MLBC tenogenic medium (DMEM supplemented with 10% FBS, 1% Pen/Strep, 10 ng/mL TGF-β1, and 50 µg/mL AA) or MLBC endochondral medium (DMEM supplemented with 10% FBS, 1% Pen/Strep, 50 µg/mL AA, 100 nM dexamethasone, 40 µg/mL L-proline, 1 mM sodium pyruvate, and ITS supplement) (n=3). Scale bar = 1mm. **(B-E)** Quantification of extracellular matrix staining in MLBC 3D rolled mini-tissues (WT, *Lamtor1* KO) cultured in tenogenic or endochondral medium: **(B, C)** Sirius Red staining, **(D, E)** Alcian Blue staining. (n=3, mean ± std, unpaired t-test). **(F)** MLBCs (WT, *Lamtor1* KO, *Lamtor4* KO) were cultured in 2D for 6 days in MLBC control medium (DMEM, 10% FBS, 1% Pen/Strep, 50 µg/mL AA), MLBC tenogenic medium (same as above with

10 ng/mL TGF-β1), or MLBC osteogenic medium (DMEM, 10% FBS, 1% Pen/, 50 µg/mL AA, 10 mM β-glycerophosphate, 200 ng/mL BMP2), and stained with Alizarin Red. Scale bar = 200 µm. **(G)** Quantification of collagen content in control and tenogenic conditions. **(H)** Quantification of matrix calcification in MLBC grown in osteogenic conditions. (n=3, mean ± std, 2-way ANOVA). **(I)** MLBCs (WT, *Lamtor1* KO or *Lamtor4* KO) were cultured in 2D in 96-well plates in MLBC control or tenogenic medium and stained with Alizarin Red after 4, 6, or 10 days (n = 3). **(J)** MLBCs (WT, *Lamtor1* KO or *Lamtor4* KO) were cultured in 2D in MLBC osteogenic medium and stained with Alizarin Red after 4, 6, or 10 days. Quantification of extracellular matrix calcification is shown. (n=3, mean ± std, 2-way ANOVA). Statistical significance: *p<0.05, **p<0.01, ***p<0.001, ****p<0.0001.

Figure S3

(A) Primary rat tail tenocytes (RTT) (WT and *Lamtor4* KO) were cultured in 2D for 3 days in RTT N2 control medium (DMEM/F12 + N2 supplement, 1% Pen/Strep, 50 µg/mL AA), or RTT N2 tenogenic medium supplemented with 5 ng/mL TGF-β1. Fibrillar collagen was stained using Alexa 555-conjugated CNA35 and quantified (n=2; mean ± std; two-way ANOVA). **(B)** RTTs (WT, *Lamtor1* KO, *Rraga* KO, *Wdr24* KO, *Lamtor2* KO, *Mios* KO) were cultured in 2D for 3 days in RTT DMEM/F12 control medium (DMEM/F12 + N2 supplement, 1% Pen/Strep + 50 µg/mL AA), or in RTT DMEM/F12 tenogenic medium supplemented with 5 ng/mL TGF-β1. Fibrillar collagen was stained and quantified using Alexa 555-conjugated CNA35 (n=2; mean ± std; two-way ANOVA). **(C)** Quantitative PCR analysis of *Scx* expression in RTTs (WT, *Lamtor2* KO, *Mios* KO, *Atp6v0e1* KO, or *RragC* KO) cultured in RTT N2 control medium. Expression was normalized to *Eif4a2* (n=2; mean ± std; multiple unpaired t-test). **(D)** Quantitative PCR analysis of *Scx* expression in RTTs (WT and *Lamtor1* KO, *Rraga* KO, *Wdr24* KO, *Lamtor2* KO, *Mios* KO, *RragC* KO cultured in RTT DMEM/F12 medium (with or without 50 µg/mL ascorbic acid). Expression was normalized to *Eif4a2* (n=1). **(E)** Representative images of primary RTTs (WT and *Lamtor4* KO) cultured as 3D mini-tissues in RTT medium (DMEM, 20 % FBS, 1% MEM NEAA, 0,1% Mercaptoethanol 50 mM, 1% Pen/Strep, 300 µg/mL AA). **(F-H)** RTT 3D mini-tissues (WT, *RragA* KO, *Nprl2* KO, *Lamtor2* KO, *Slc38a9* KO, *Wdr24* KO, *Mios* KO, or *Atp6v0e1* KO) were cultured for 7 days in RTT medium (DMEM, 20 % FBS, 1% MEM NEAA, 0,1% Mercaptoethanol 50 mM, 1% Pen/Strep, 300 µg/mL AA) and subjected to

biomechanical analysis. **(F)** Mini-tissue diameter (n=2-6, mean ± std , ordinary one-way ANOVA). **(G)** Force to failure (n=3-8; mean ± std, ordinary one-way ANOVA). **(H)** Hydroxyproline content normalized to DNA (n=2-5; mean ± std, ordinary one-way ANOVA). **(I)** Quantitative PCR analysis of *Scx* and *Col1a1* expression in RTT 3D fibrin mini-tissues (WT, *Lamtor2* KO, *RragC* KO, *RragA* KO, *Mios* KO, or *Wdr24* KO) cultured for 7 days in tenogenic RTT medium (DMEM, 20 % FBS, 1% MEM NEAA, 0,1% Mercaptoethanol 50 mM, 1% Pen/Strep, 300 µg/mL AA). Expression was normalized to *Eif4a2* (n=2-4, mean ± std, ordinary one-way ANOVA). **(J-K)** Quantitative PCR analysis of immortalized human MSCs cultured in 2D (WT and *LAMTOR1* KO) to assess expression of *LAMTOR1* **(J)** and *SCX* **(K)**, normalized to *Rps18* (n=3, mean ± std, unpaired t-test). **(L)** Western blot analysis of whole-cell lysates from immortalized hMSCs (WT or *LAMTOR1* KO, LAMTOR4 KO; n=2) cultured in hMSC growth medium (DMEM, 10% FBS, 1% Pen/Strep). Ponceau S staining was used to confirm equal loading. **(M)** Western blot analysis of whole-cell lysates from immortalized hMSCs (WT, *LAMTOR1* KO; n = 3) cultured in hMSC tenogenic medium (DMEM, 10% FBS, 1% Pen/Strep, 50 µg/mL AA, 10 ng/mL TGFβ1). Ponceau S staining was used to confirm equal loading. **(N)** Immortalized hMSC (WT and *LAMTOR4* KO) were differentiated 3 days in growth medium (GM), GM supplemented with 50 µg/mL AA (Asc. Acid), or GM with AA and 10 ng/mL TGF-β1 (AA + TGF-β1). **(O)** Quantification of fibrillar collagen using Alexa 555-conjugated CNA35 (orange); nuclei were counterstained with Hoechst (blue). (n=4; mean ± std; two-way ANOVA). **(P)** Representative image of 96-well flexible hanging post microtissues (stiff posts: k = 0.51 kN/µm; soft posts: k = 0.051 kN/µm) seeded with immortalized hMSCs (WT or *LAMTOR4* KO) at 12 days post-plating. Constructs were stained with hematoxylin and cultured in hMSC standard growth medium supplemented with 50 µg/mL ascorbic acid or with ascorbic acid and 10 ng/mL TGF-β1 (AA + TGF-β1) (n=4). Statistical significance: *p<0.05, **p<0.01, ***p<0.001, ****p<0.0001.

Figure S4

(A-B) Western blot analysis of whole-cell lysates from MLBCs (WT, *Lamtor1* KO, or *Lamtor4* KO; n = 3) cultured in standard MLBC growth medium (DMEM plus 10% FBS and 1% Pen/Strep)**.** Ponceau S was used to verify equal protein loading. **(C)** Western blot analysis of whole-cell lysates from MLBCs (WT, *Lamtor1* KO; n = 3) cultured in MLB growth medium and treated with Bafilomycin A (25 nM) for 1 h, 3 h, or

6 h. **(D-E)** Quantification of p62 immunofluorescence in MLBCs (WT, *Lamtor1* KO, *Lamtor4* KO) cultured in growth medium and treated with **(D)** Bafilomycin A (25 nM) or **(E)** Chloroquine (50 µM). (n=2-4, mean ± std, two-way ANOVA). **(F)** Quantification of LC3 immunofluorescence in MLBCs (WT, *Lamtor1* KO, *Lamtor4* KO) cultured in MLBC growth medium and treated with Chloroquine (50 µM). (n=2, mean ± std, two-way ANOVA). Quantitative PCR analysis of *RRAGD* or *SQTM* expression normalized to *Rps18* in **(G-H)** hMSCs (WT, *LAMTOR1* KO) and **(I-J)** MLBCs (WT, *Lamtor1* KO) all n=3, mean ± std, unpaired t-test). **(K-L)** BCA protein quantification for amino acid measurements **(M-N)** in whole-cell lysates from **(K)** immortalized hMSCs or **(L)** MLBCs (n=9-12, mean ± std, unpaired t-test). **(M-N)** Amino acid quantification from whole-cell lysates of **(M)** immortalized hMSCs or **(N)** MLBCs (n=9-12, mean ± std, two-way ANOVA). Statistical significance: *p<0.05, **p<0.01, ***p<0.001, ****p<0.0001. **(O)** Western blot analysis of whole-cell lysates from MLBCs (WT, *Lamtor1* KO, *Lamtor4* KO) cultured in MLBC growth medium and treated with Torin1 (100 nM) or Rapamycin (100 nM) for 24 h. Quantification of phosphorylated S6 ribosomal protein (p-S6RP) is shown on the right. *β-Actin* was used as a loading control. **(P)** Western blot analysis of whole-cell lysates from MLBCs (WT, *Lamtor1* KO) seeded in MLBC growth medium (DMEM 10% FBS, 1% Pen/Strep), followed by treatment with MEMα (5.5 mM glucose, serum-free) for 1 h, and subsequent stimulation with IGF1 (100 nM) or TGF-β1 (10 ng/mL) in MEMα for 15 or 60 min. *Ponceau S* staining was used to confirm equal loading.

Figure S5

(A) Principal component analysis (PCA) of MLBC proteomic profiles demonstrating distinct clustering of samples (WT, *Lamtor1* KO) cultured for 3 days in either standard MLBC growth medium (DMEM plus 10% FBS and 1% Pen/Strep) or tenogenic MLBC medium (DMEM plus 10% FBS, 1% Pen/Strep, 50 µg/mL ascorbic acid, and 10 ng/mL TGF-β1). **(B-C)** Volcano plots illustrating differential protein abundance in MLBCs (WT, *Lamtor1* KO) cultured in (B) growth medium or (C) tenogenic MLB medium (n=3, 3 days). **(D-E)** Top upregulated and downregulated proteins identified in *Lamtor1* KO MLBCs from the proteomics screen under **(D)** growth medium or **(E)** tenogenic MLB medium conditions. **(F)** Schematic representation of the cholesterol biosynthesis pathway and its extended regulatory network. Pharmacological inhibitors targeting the pathway are highlighted in red. Figure created with BioRender.com.

Figure S6

(A) Principal component analysis (PCA) of MLBC lipidomic profiles showing separation of sample distributions (WT, *Lamtor1* KO) in growth medium or tenogenic MLBC medium (n = 6, 1 day). **(B)** Volcano plots of lipidomic data from MLBCs (WT, *Lamtor1* KO) cultured in growth medium (left) or tenogenic MLBC medium (right) (n = 6, 1 day). **(C)** Heatmap of lipidomics analysis on MLBCs (WT, *Lamtor1* KO) after 1 day of culture in MLBC control medium or tenogenic medium. Lipid class abundance is shown relative to WT control; red indicates upregulation, blue indicates downregulation. **(D-E)** Total cholesterol content was measured in cell lysates from MLBC **(D)** or immortalized hMSC **(E)**, comparing WT and *Lamtor1* knockout (KO) conditions. Quantitative analysis revealed no significant difference in cholesterol levels between *Lamtor1* KO and control cells in either cell type (n=3, mean ± std, unpaired t-test). Statistical significance: *p<0.05, **p<0.01, ***p<0.001, ****p<0.0001.

Figure S7

(A) Relative abundance of Gpnmb from the proteomics screen of MLBCs (WT, *Lamtor1* KO) cultured for 4 days in MLBC control medium (DMEM, 10% FBS, 1% Pen/Strep) or MLBC tenogenic medium (DMEM, 10% FBS, 1% Pen/Strep, 10 ng/mL TGF-β1, 50 µg/mL AA. **(B)** Western blot analysis of whole-cell lysates from MLBCs (WT, *Lamtor1* KO; n = 6) cultured for 5 days in MLBC tenogenic medium. Ponceau S staining was used to confirm equal protein loading. **(C)** Quantitative PCR analysis of *Gpnmb* expression normalized to *Rps18* in MLBCs (WT and *Lamtor1* KO) **(D)** Relative luminescence in MLBCs transfected with an *SCX*-luciferase reporter plasmid (100 ng) and incubated for 48 hours with TGF-β1 (1 ng/mL) and AA (50 µg/mL), with or without 1 µM recombinant human GPNMB. **(E-F)** Quantitative PCR analysis of *Gpnmb* and **(E)** tenogenic markers (*Scx, Egr1*, and *Col1a2*) or **(F)** chondrogenic markers (*Sox9*, *Col2a1*, *Col10a1*) in MLBCs (WT or *Gpnmb* KO) cultured in MLBC control or tenogenic medium normalized to *Rps18*. **(G)** Representative images of MLBC 3D fibrin mini-tissues (WT or *Gpnmb* KO) on day 7 cultured in MLBC tenogenic medium. Tissues were co-stained with Alcian Blue (glycosaminoglycans, blue) and Picro Sirius Red (collagen, pink). Scale bar = 100 µm.

MATERIALS AND METHODS

Materials and Methods

Animal Husbandry and Ethics

All mice were housed under specific pathogen-free (SPF) conditions at the Novartis BioMedical Research (BR), Basel, Switzerland, with ad libitum access to standard chow and water. All procedures were approved by the Cantonal Veterinary Office of Basel-Stadt (license BS-2439, ID 20626) and conducted in accordance with the Swiss Animal Welfare Act.

Mouse Models and Genetic Manipulation

Lamtor1$^{flox/+}$ mice (GemPharmatech, Nanjing, China) on a C57BL/6 background (Charles River Laboratories, Wilmington, MA, USA) were used. Due to infertility in homozygous floxed animals, global heterozygous knockouts were generated via in utero electroporation (IUE) of Cas9 into heterozygous embryos. Experimental group sizes are indicated in figure legends. All efforts were made to minimize animal use and suffering.

Mouse Achilles Tendon Surgery

At 4 months of age, male and female control and *Lamtor1* global heterozygous mice underwent right hindlimb Achilles tendon injury. Animals were anesthetized with 2% isoflurane and pre-treated with [Ethiqa XR buprenorphine, 3.25 mg/kg] 1 hour prior to surgery. A 2 mm longitudinal incision was made in the tendon under aseptic conditions. The skin was sutured, and mice were housed individually with environmental enrichment. The contralateral limb served as an internal control.

Rat Supraspinatus Tendon Surgery

At 4-5 months of age, female Sprague Dawley rats (Janvier, France) underwent right rotator cuff surgery to place a controlled supraspinatus tendon injury. Animals were pre-treated with [Ethiqa XR buprenorphine, 0.65 mg/kg] 1 hour prior to surgery. A supraspinatus tendon injury was performed aseptically under general anaesthesia with 2% isoflurane. After skin incision and deltoid muscle incision, the supraspinatus tendon was extracted from the subacromial space and kept under tension, and a full-

765 length longitudinal tenotomy was placed with a scalpel. The deltoid muscle and the skin were sutured
766 closed individually with sutures, and rats were housed post-recovery with pre-surgery cage mates. The
767 contralateral limb served as an internal control.

768 The applied *Lamtor1* siRNA aligns with rat *Lamtor1* mRNA (LOC100361543) at CDS position 493.
769 Antisense reference sequence: 5'-TGAGAAAGTGCACTATAGGCATA-3'. Sense reference sequence: 5'-
770 TGCCTATAGTGCACTTTCTCA-3'. Annealed oligos were prepared at 25 mg/mL in sterile saline and
771 injected 7 days after surgery (20uL) into the sub-acromial space.

772 **In Vivo Imaging**

773 Magnetic resonance imaging (MRI) and ultrasound shear wave elastography (SWE) were performed as
774 described[46]. MRI measurements were conducted using a Pharmascan 7 Tesla scanner (Bruker Medical
775 Systems, Germany) on animals anesthetized with isoflurane (1.5-2 vol% for mice, 2.5- vol 3% for rats, in
776 100% oxygen) delivered via a face mask and placed on prone position in a plexiglas cradle. Eye
777 protection was provided using Viscotears (Bausch + Lomb Swiss, Switzerland). Body temperature was
778 kept at 37°C using a heating pad. The respiration rate was monitored throughout the MRI session. A
779 volume resonator (40 and 72 mm inner diameter for mice and rats, respectively) served for
780 radiofrequency transmission. A two-channel phased array receive-only mouse head surface coil was used
781 for signal reception. All radiofrequency coils were manufactured by Bruker.

782 For the rat rotator cuff, following MRI acquisitions were performed: (i) anatomical T_2-weighted images
783 were acquired using a RARE (Rapid Acquisition with Relaxation Enhancement) sequence with the
784 parameters repetition time (TR) 5600 ms, effective echo time (TE) 21 ms, RARE factor 4, field-of-view
785 (FOV) 40x30 mm^2, matrix 256x192, in-plane pixel 0.156x0.156 mm^2, slice thickness 0.42 mm, 15 slices,
786 scan time 4 min 29 s; (ii) assessments of the relaxation time T_2 sensitive to inflammation were performed
787 using a multi-echo spin-echo sequence with the parameters TR 2696.2 ms, 16 echo times (TEs) equally
788 spaced by 11 ms and ranging from 11 ms to 176 ms, 11 slices, acceleration factor 1.34, scan time 6 min
789 28 s. Anatomical parameters were the same as for the RARE acquisition. The relaxation time T2 was
790 determined by exponentially fitting the corresponding signal from a given region-of-interest as function of
791 TE; (iii) the relaxation time T_2*, which is related to inflammation and microstructural disorganization in

tendinopathy (Malmgaard-Clausen et al, 2021), was determined using a three-dimensional ultrashort echo time (UTE3D) sequence with the parameters TR 4 ms, 39940 projections, excitation pulse 0.02 ms, 64 kHz bandwidth, 2.5 degrees, FOV 40x40x45 mm^3, matrix 160x160x160, pixel 0.25x0.25x0.28 mm^3. Two UTE3D acquisitions were performed, each lasting 2 min 40 s, with TE_1 of 0.02 and TE_2 of 1.2 ms. Given the exponential decay of the detected signal, T_2* was computed from these two acquisitions using the formula

Relaxation time $T_2^* = (TE_2\text{-}TE_1)/\ln(S_1/S_2) = 1.18\ ms/\ln(S_1/S_2)$

S_i Signal in region of interest for UTE3D acquisition with TE_i (i=1,2)

TE_i Echo time for UTE3D acquisition (TE_1 = 0.02 ms, TE_2 = 1.2 ms)

Analogous UTE3D acquisitions were performed on the mouse Achilles tendon to determine T_2*. The parameters were the same as for the measurements of the rat rotator cuff, except for FOV 25x35x25 mm^3, pixel 0.16x0.22x0.16 mm^3. Tendon stiffness was assessed by SWE immediately after the MRI, without letting the mice wake up. SWE was performed using an Aixplorer system (SuperSonic Imagine, France) with a 25 MHz SL25-15 linear transducer to assess tendon stiffness. The animals were placed on a heating pad, the legs were lightly shaved and a contact gel was applied for the ultrasound examinations. For each mouse, three SWE measurements were performed and the mean stiffness was considered for further analyses.

Biomechanical Testing

Post-mortem Achilles tendons were stored in PBS-moistened gauze. Cross-sectional area (CSA) was calculated from images taken at four angles. Tendons were tested using an Electroforce 3200 system (TA Instruments) with the following protocol: preload (0.1 N), preconditioning (30 cycles, 0.25–0.5% strain), stress relaxation (4% strain), frequency sweep (0.1–10 Hz, 0.125% strain), and ramp to failure (0.5% strain/s). Additional failure testing was performed using a Univert system (CellScale) with uniaxial loading at 0.1 mm/s. CSA was calculated as width × thickness. Tendons were kept hydrated with PBS throughout testing.

Post-mortem supraspinatus tendons were collected at day 28 post-surgery from both injured and healthy contralateral shoulders, wrapped in PBS-soaked gauze, and stored at −20°C. For mechanical testing, frozen specimens were thawed and mounted with the tendon attached to the humerus. Morphology was measured using digital slide calipers. Tendons were analyzed as previously described[47].

Histology and Staining

Tissues and 3D constructs were fixed in 10% neutral-buffered formalin (Sigma-Aldrich, HT501128) for 24 h at 4 °C, dehydrated in graded ethanol, cleared in xylene, and paraffin-embedded. Sections (5 µm) were stained as follows:

Picro-Sirius Red: Collagen was stained with Sirius Red (Direct Red 80, #43665, Sigma-Aldrich) for 45 min, rinsed in acidified water, counterstained with Mayer's hematoxylin (Sigma-Aldrich), and mounted.

Alcian Blue: Sections were equilibrated in 3% acetic acid and stained with 0.1% Alcian Blue (pH 2.5, A5268, Sigma-Aldrich) for 15 min.

Alizarin Red: Cells were fixed in 10% formalin, stained with 0.4% Alizarin Red-S (A5533, Sigma-Aldrich) for 10–30 min, and washed with Milli-Q water.

Immunofluorescence

All antibodies are listed in Table S4. FFPE sections were dewaxed, rehydrated, and subjected to antigen retrieval in 10 mM citrate buffer (pH 6) at 95 °C for 1 h. After PBS-T washes, samples were blocked with 12% BSA (Sigma-Aldrich), incubated with primary antibodies overnight at 4 °C, and with secondary antibodies for 2 h at room temperature. Hoechst 33342 (Thermo Fisher Scientific, H3570) was used for nuclear staining. IHC was performed using Vectastain ABC-HRP and DAB kits (Vector Laboratories). For PDMS-based microtissues, fixation was done in 4% paraformaldehyde (Electron Microscopy Sciences), followed by permeabilization with 0.5% Triton X-100 (Sigma-Aldrich), blocking with 3% BSA (Fluka), and staining with Alexa Fluor 647 Phalloidin (1:300, Thermo Fisher) and Hoechst 33342 (1:1500).

For cultured cells, fixation was performed with either methanol (20 min) or 10% formalin (30 min), followed by permeabilization with 0.1% NP-40 (Sigma-Aldrich), blocking with Blocking Reagent (Sigma

#37527), and antibody staining as above. DAPI (Thermo Fisher) was used for nuclear counterstaining (Table S4).

Image acquisition and quantification

Histochemical and fluorescence-stained 3D tissues were imaged using an Axio Imager A1 or Axioskop 2 fluorescence microscope (Carl Zeiss), or an EVOS microscope (Thermo Fisher Scientific). Images were acquired with an Axiocam HRc camera (Carl Zeiss) and processed using Axiovision software. Quantitative image analysis was performed using Fiji (ImageJ) software (Schindelin et al., 2012).

High-content imaging, including Fluopack screening and 3D spheroid analysis, was conducted using a Yokogawa spinning disk confocal microscope (CV7000). Fluopack images were analyzed with CellProfiler in the web-based application HCS IA, while spheroid images were processed using CellPathfinder software (Yokogawa) to quantify nuclei count, spheroid area, Scx-GFP intensity, and Alexa Fluor 555-labeled collagen signal.

For PDMS-based two-pillar microtissues, fluorescence imaging was performed using an Olympus FV3000 confocal microscope and analyzed with Olympus CellSense software. Label-free collagen I visualization was achieved via second harmonic generation (SHG) imaging using a Zeiss LSM 980 NLO two-photon microscope equipped with a Spectra-Physics InSight X3 laser tuned to 920 nm. Imaging was performed using a 25× 0.8 NA LD-LCI objective and a 1.2 NA water immersion condenser. Forward-scattered SHG signals were detected using a transmitted light PMT, and backward-scattered signals were collected with a non-descanned GaAsP detector and a 440–480 nm emission filter.

MLB Cell Line Generation and Characterization

Immortalized *Scx-gfp* mouse limb bud cells (MLBCs) were derived from embryonic day 11.5–13.5 mouse limb buds. Primary cells were transduced with lentiviral vectors encoding c-Myc to promote immortalization. Geneticin (G418) was added at the time of transduction and withdrawn once stable cell growth was established. Following the senescence of non-transduced cells, resistant clones—conferred by the G418 resistance gene encoded in the lentiviral vector—were selected and expanded. Low GFP-expressing populations were enriched via FACS and further engineered to express Cas9 under EF1α promoter control, using blasticidin selection.

Primary Rat Tail Tenocytes

Adult rat tails were harvested under sterile conditions, and fascicles were dissected from the tail tendons using fine forceps. The tissue was minced and subjected to enzymatic digestion in a solution of 3mg/ml collagenase type IV (Thermo Fisher Scientific, Cat# 17104019) (PBS + 1% Pen/Strep) for 4 hours at 37 °C with hourly pipette resuspension. Post-digestion, tissues were plated in 150 cm² dishes with 30 mL RTT culture medium (DMEM + 20% FBS + 1% Pen/Strep). Cells were cultured at 37 °C, 5% CO_2, monitored for attachment, and expanded upon reaching confluence. Cell stocks were cryopreserved at passage 2 in 0.1% DMSO at 550,000 cells/mL

Cell Culture

Immortalized mouse limb bud cells (MLB), immortalized human mesenchymal stem cells (hMSC, JCRB1154, UE7T-13), and primary rat tenocytes (RTT) were cultured at 37 °C, 5% CO_2. Specific media used for different assays and cell types can be found in Table S5. Cells were regularly tested for mycoplasma contamination using the MycoStrip™ Kit (rep-mys-100, version 22L15-NJ, InvivoGen).

3D fibrin mini-tissues

For 3D fibrin construct formation, cells were trypsinized, counted, and resuspended in medium at a density of 150,000–500,000 cells per construct, depending on the experimental design and cell type. Fibrin gels (per well of a 6-well plate) were prepared by mixing 200 µL fibrinogen (20 mg/mL in 0.9% NaCl, F4883, Sigma), 10 µL aprotinin (10 mg/mL, A3428, Sisgma), 600 µL cell suspension, and 4 µL thrombin (200 U/mL in PBS, T4393-100U, Sigma). The mixture was quickly pipetted and transferred into Sylgard (Siliconelastomer Kit Sylgard 184 Geeigne, 634165S, VWR) coated 6-well plates pre-pinned with silk suture pieces (K861H, Ethicon) and insect pins (FST26002-10, Fine Scienec Tools, 0.1mm). Plated cells in gel were allowed to polymerize for 1 hour, at 37 °C before adding 3 mL of tenogenic medium. Medium was refreshed every 2–3 days. Constructs were monitored for compaction and alignment. CNA35 imaged at the Cytation 5 imager and analyzed with Gen5 software.

3D 96-well flexible hanging post micro-tissues and Flexible PDMS two pillar device

The same fibrin gel protocol was adapted for miniaturized tendon tissue models, including 96-well

hanging post microtissues and PDMS-based two-pillar devices. Custom PDMS devices (IBIDI, Germany) with 18 wells and paired flexible pillars were UV-sterilized and coated overnight with 2% Pluronic F127 to prevent matrix adhesion. In these formats, fibrin-cell mixtures were cast into the respective platforms, allowing self-assembly and cell-mediated tension generation under tenogenic conditions. At endpoint, tissues were processed for downstream analyses including imaging, RNA/protein extraction, or histology.

3D rolled mini-tissues

For the generation of rolled tendon-like constructs, MLBCs were seeded at a density of 300,000 cells per well in 12-well plates and cultured for 2 days in growth medium. Cells were then treated with tenogenic medium for 8 days to promote extracellular matrix deposition. After 8 days, the resulting cell sheet was carefully detached and rolled using a sterile pipette tip into a cylindrical structure approximately 1 cm in length. The rolled constructs were pinned down onto Sylgard-coated 6-well plates using insect pins and cultured for an additional 13 days in medium of choice. Medium was refreshed every 2–3 days. Constructs were subsequently processed for histological, molecular, or biomechanical analysis.

Spheroid formation

For 3D spheroid formation, immortalized mouse limb bud cells (MLBCs) were seeded at 2,500 cells per well into S-Bio 384 PrimeSurface ultra-low attachment plates (MS-9384UZ). Plates were centrifuged at 1,000 rpm for 1 minute to promote cell aggregation and incubated for 8 days. Medium was exchanged three times per week using a CyBio Well Vario automated liquid handler (Analytik Jena GmBH, serial no 606386), replacing 30–50 µL per well. To quantify collagen deposition, Alexa Fluor 555-conjugated CNA35 (1 µg/mL) and Hoechst 33258 (#33342, H3570, Invitrogen; 1:500 dilution) were added to each well 1 hour prior to imaging on Yokogawa Microscope (#KZP00019).

Microtissue Force Measurement

For the PDMS pillar deflection, Axial contractile force (F) was calculated from pillar deflection (δ) using Hooke's law: $F = k \times \delta$, where k is the spring constant of the PDMS pillar at the tissue height (h_{tissue}). To account for deflection at different heights, the Euler–Bernoulli beam equation was applied: $F_h = k_0 \times \delta / (h/h_0)^3$, with h_0 = 1 mm and k_0 = 11 µN/µm. To correct for deflection measured at the pillar top, the actual deflection at tissue height was calculated as:$\delta = \delta_{top} \times h_{tissue} / (3 \times h_{top} - h_{tissue})$.

Osteogenic cell differentiation

Cells were seeded at peak confluence in a basic medium overnight. The following day, the medium was replaced every 2-3 days with an osteogenic medium comprising DMEM (10569-010), 10% FBS (97068-085), 1% P/S (15140-122), 50 µg/mL ascorbic acid (A4544-100g), 10 mM β-glycerol phosphate (G9891), and 200 ng/mL BMP2 (120-02C-10ug). The extracellular matrix around the cells began to show dark deposits indicative of mineralization. Cells were fixed and processed as desired between days 6 and 10.

Endochondral cell differentiation

Cells were expanded to a sub-confluent state in basic medium, trypsinized, and plated as a 10 µL drop containing (2 \times 10^5) cells in each well of a 48-well plate. The plate was incubated for 2 hours at 37°C, followed by the careful addition of 1 mL of basic medium overnight. The next day, the basic medium was replaced with 500 µL of chondrogenic medium, consisting of DMEM (10569-010), 10% FBS (97068-085), 1% P/S (15140-122), 50 µg/mL Ascorbic Acid (A4544-100g), 10 mM Dexamethasone (D4902-100mg), 40 µg/mL L-Proline (P5607-25), 1 nM Sodium Pyruvate (S8636-100ml), 10 mM β-glycerophosphate (G9891, Sigma), and ITS premix (25-800-CR), as previously described (Wang et al., 2016). The medium was refreshed every 2-3 days for a duration of 4-10 days, after which the cells were processed for Alcian Blue staining as desired.

Tenogenic cell differentiation

Cells were seeded at 70% confluency in their respective control media. The following day, the medium was replaced with tenogenic differentiation media specific to each cell line and refreshed every 2–3 days for a total of 2–8 days (see specific media composition for each cell line in Table S5). After this period, cells were processed as required. Due to substantial extracellular matrix production, cells may begin to contract and potentially detach; therefore, harvesting prior to this stage is recommended.

Hydroxyproline assay

Fibrin constructs were digested using papain, hydrolyzed with 100 µL of 37% HCl (Merck) at 120 °C for 3 h, and evaporated at 60 °C. Chloramine T/oxidation buffer and DMAB reagent were added, and absorbance was measured to quantify hydroxyproline.

Sample Preparation for Proteomics

Protein samples were processed using the PreOmics iST Kit (version 5, 8-reaction format, P.O.00001, Preomics) according to the manufacturer's protocol. Briefly, cell lysates were denatured, reduced, and alkylated in a single-step buffer system, followed by enzymatic digestion using a trypsin/LysC mix. Peptides were purified via solid-phase extraction and eluted for LC-MS/MS analysis. All steps were performed in a single tube to minimize sample loss and variability, ensuring high reproducibility and compatibility with downstream mass spectrometry workflows.

Cell transfection

Cells were seeded in 24-well plates at approximately 50% confluency and transfected with 100 ng of the respective plasmid using Lipofectamine™ (Thermo Fisher Scientific) according to the manufacturer's instructions. After 24 hours, the medium was replaced with treatment medium and cells were incubated for an additional 24 hours before harvesting.

RNA isolation and RT-qPCR analysis

RNA was extracted using the RNeasy Mini Kit (74104, Qiagen) and reverse transcribed with the iScript™ cDNA Synthesis Kit (1708891, Bio-Rad). RT-qPCR was performed using LightCycler® 480 SYBR Green I Master Mix (04707516001, Roche) or Taqman probes with corresponding mastermix (43240218, life technologies) on a LightCycler® 480 II system. Gene expression was normalized to Rps18 using the 2^−ΔΔCt method. Primers used can be found in Table S6.

Protein lysates and Western blotting

Cells were lysed in 6 M urea buffer containing 1 mM EDTA, 0.5% Triton X-100, and 5 mM NaF in PBS (pH 7.2–7.4). Lysates were subsequently diluted to 1 M urea using a matching diluent buffer. Protein concentrations were determined using the Pierce™ BCA Protein Assay Kit (23225, Thermo Fisher Scientific). Equal amounts of protein were resolved on 4–12% SDS-PAGE gels and transferred to nitrocellulose membranes. Membranes were incubated with primary antibodies, followed by HRP-conjugated secondary antibodies. Signal detection was performed using the WesternBright™ ECL kit (K-12045-D20, Advansta). Antibodies used can be found in Table S4.

Proteomics

WT and *Lamtor1* KO mouse limb bud (MLB) cells were cultured under normal growth or tenogenic conditions, and cell pellets (~10^6 cells, ~1 mg protein) were processed using the iST Sample Preparation Kit (PreOmics) with minor protocol adaptations. Lysis was performed in LYSE-iST buffer supplemented with Bond-Breaker TCEP (Cat# 77720, Thermo Fisher Scientific), followed by heat denaturation, sonication, and overnight digestion at 37 °C. Peptides were purified via cartridge-based cleanup, eluted, dried under nitrogen flow, and resuspended in 0.1% formic acid. Concentrations were estimated by LC-UV (Waters H-Class), and ~1.5 µg peptides were injected for LC-MS/MS analysis using a Thermo Orbitrap Fusion Lumos with an EASY-nLC 1200 and a 25 cm IonOpticks Aurora column (Cat# AUR2-25075C18A). Data were acquired with a 3 h gradient and processed using Proteome Discoverer 3.0.1.27 for label-free quantification. Proteins with complete triplicate data in WT or KO conditions were retained, and differential expression was assessed using Spotfire with volcano plot visualization.

Lipidomics

Lipidomic profiling was performed on MLBCs (WT and Lamtor1 KO) cultured in growth or tenogenic medium. Cells were harvested after 24 hours. Cell pellets were extracted using 400 µL of 90% isopropanol. 15 µL of EquiSPLASH® (Avanti Polar Lipids) and additional 1.5 µL of SM, MG and DG internal standards were added to each sample. Samples were vortexed for 10 min and centrifuged for 20 min at 18000 rcf. Resulting supernatants were dried in a SpeedVac and reconstituted in 70 µL 60% acetonitrile. The samples were vortexed and centrifuged again with the same condition mentioned above. Resulting supernatants were directly submitted to LC-MS-based lipid analysis.

LC-MS was performed using a Acquity Premier CSH C18 column (100 x 2.1 mm; 1.7 µm) and matching pre-column (5 x 2.1 mm; 1.7 µm) using a binary solvent system of (A) 60:40 (v/v) acetonitrile:water with ammonium formate (10 mM) and formic acid (0.1%) and (B) (v/v) 90:10 isopropanol:acetonitrile with ammonium formate (10 mM) and formic acid (0.1%). For LC-ESI(-) mode, the organic solvents for mobile phases were the same except for using ammonium acetate (10 mM) as mobile-phase modifier. Flow rate was 0.6 mL/min at 65 °C. Injection volume was 7 µL in both polarities.

Lipids were analyzed using a Vanquish Horizon UHPLC system coupled to an Orbitrap Fusion Lumos mass spectrometer (Thermo Fisher Scientific). The spray voltage was set to +3,500 V for positive ion mode and -3,000 V for negative ion mode. The ionization parameters included sheath gas flow rate at 50 arbitrary units, auxiliary gas flow rate at 10 arbitrary units, sweep gas flow rate at 2 arbitrary units, vaporizer temperature at 300 °C, and ion transfer tube temperature at 320 °C. The AcquireX algorithm was used to generate data-dependent MS/MS information. Lipid annotation via spectral matching was done in MS-DIAL (citation needed: https://www.nature.com/articles/nmeth.3393) followed by data analysis using an in-house R (https://www.r-project.org/) script.

Pooled Genome-Wide CRISPR-Cas9 screen

A genome-wide CRISPR-Cas9 sgRNA library targeting approximately 20,000 genes (≤5 sgRNAs per gene) was packaged into lentivirus and transduced into Cas9-expressing mouse limb bud cells (MLBCs) at a multiplicity of infection (MOI) of 0.5 to ensure single-guide integration. Following puromycin selection, cells were cultured for 11 days, for low cell density, and 13 days, for high density condition, 25% low and 25% high Scx-GFP expressing cells were FACS-sorted and genomic DNA was isolated and subjected to NGS for sgRNA counting.

The mouse genome-wide library was constructed by Cellecta as previously described for human genome wide-libraries (Ramos et al., 2014). The genome-wide sgRNA library targeting 18,360 protein-coding genes, with five unique sgRNAs per gene, where possible, was constructed using chip-based oligonucleotide synthesis to generate spacer-tracrRNA-encoding fragments that were PCR-amplified and cloned as a pool into the BpiI site of the pRSI16 lentiviral plasmid (Cellecta, Mountain View, CA). Olfactory receptors were omitted from the library. The sgRNA were selected to target the most proximal 5’ exon of each gene to contain an NGG PAM motif, filtering for GC content greater than 40% and less than 80%, eliminating homopolymer stretches greater then four, and removing any guides with off-target locations having fewer than four mismatches across the genome. Sequencing of the plasmid pool showed robust normalization with >90% clones present at a representation of +/− five fold from the median counts in the pool.

Illumina library construction and sequencing

Genomic DNA from 4% paraformaldehyde-fixed cells was isolated using phenol/chloroform extraction. Illumina sequencing libraries were generated using PCR amplification with primers specific to the genome integrated lentiviral vector backbone sequence. A total of 24 x 4 µg PCR reactions were performed per transduced sample. PCR reactions were performed in a volume of a 100 µl containing a final concentration of 0.5 µM of each PCR primer (Integrated DNA Technologies, Coralville, IA), 0.5 mM dNTPs (Clontech) and 1x Titanium Taq and buffer (Clontech). PCR cycling conditions used were as follows: 1x 98°C for 5 min; 28x 95°C for 15 s, 65°C for 15 s, 72°C for 30 s; 1x 72°C for 5 min. The resulting Illumina libraries were purified using 1.8x SPRI AMPure XL beads (Beckman Coulter, Indianapolis, IN) following the manufacturer's recommendations and qPCR quantified using primers specific to the Illumina sequences using standard methods. Illumina sequencing libraries were pooled and sequenced with a HiSeq 2500 instrument (Illumina, San Diego, CA). sgRNA libraries were sequenced with 1x30 b (sgRNA) and 1x11 b (sample index) reads. Sequencing was performed following the manufacturer's recommendations, using custom sequencing primers. The number of reads was adjusted to cover each sgRNA with approximately 1000 reads.

Then the raw sequencing reads were aligned to the appropriate library using Bowtie (Langmead et al., 2009) allowing for no mismatches and counts were generated. Differential fold change estimates were generated using DESeq2 (Love et al., 2014) to compare the representation in the 'low' gate to the 'high' gate in the FACS sort. Additionally, to assess effects on proliferation, the fold change of the unsorted cell population compared to the input library was generated. For gene-based hit calling, Redundant siRNA Activity (RSA) (König et al., 2007) and average or maximal fold changes were calculated across all reagents for a given gene. Biological contextualization was assessed by measuring the significance of overlap between screen hits and Gene Ontology Biological Process groups using a hypergeometric test and correcting for multiple hypothesis testing using the Benjamini-Hochberg test.

Validation of CRISPR Hits

To validate candidate genes from the Scleraxis CRISPR screen, we performed CRISPR-Cas9 knockouts of *Lamtor1*, *Mvd*, *Erlin1* in MLBC E11.5 Scx-GFP clone F12 cells using ribonucleoprotein (RNP) complexes. Chemically synthesized crRNAs targeting each gene were annealed with tracrRNA and

complexed with HiFi Cas9 nuclease (IDT). RNPs were delivered via Neon electroporation (1600 V, 20 ms, 1 pulse), with a multiple stop codon (MSC) DNA template included to enhance knockout efficiency. Cells were cultured for 3–10 days post-electroporation in antibiotic-free medium. Genomic DNA was extracted using QuickExtract™ solution, and gene disruption was confirmed by PCR genotyping and agarose gel electrophoresis. Scx-GFP expression was assessed by flow cytometry 14 days post-transfection to evaluate the phenotypic impact of each knockout.

Pathway enrichment analysis CRISPR screen

To identify biological pathways from the CRISPR Screen Hit analysis, enriched among genes upregulated or downregulated in low-density conditions, we performed pathway enrichment analysis of the screening hits (RSA ≤ 4 and log2FC > 1) in R using the hypergeometric test with Reactome pathways, leveraging the R packages enrichR and MSigDB. P values were adjusted for multiple testing using the Benjamini-Hochberg procedure (Jawaid et al, 2025; Dolgalev et al, 2025). For the knockouts that decreased *Scx-gfp* expression, genes that appeared as frequent hitters in previous screens and those that decreased in the unsorted cell population compared to the input were removed from the analysis to avoid hits solely driven by an effect on proliferation. This was only necessary for knockouts that decreased *Scx-gfp* expression due to the substantial overlap between the hits and genes that were frequent hitters/genes that decreased in the unsorted cell population compared to the input, which was not the case with the knockouts that increased *Scx-gfp* expression.

Fluopack Screening

High-content phenotypic screening was performed using the Fluopack platform to assess organelle-specific and functional changes in immortalized hMSCs (WT, *LAMTOR1* KO, *LAMTOR4* KO). Cells were stained with a panel of 41 fluorescent probes targeting various cellular compartments and processes (Table S4). Imaging was conducted using a Yokogawa spinning disk confocal microscope (CV7000), and data were analyzed with CellProfiler in the web-based application HCS IA. This approach enables multiplexed visualization of subcellular features and has been widely used for profiling cellular phenotypes in response to genetic or chemical perturbations (Kang et al, 2020).

Cholesterol Quantification

Cells were lysed in 100 µL of 5× Reaction Buffer from the Amplex™ Red Cholesterol Assay Kit (A12216, Thermo Fisher Scientific) and processed per manufacturer's instructions.

Amino Acid Quantification

MLBCs or hMSC were seeded in 24-well plates at densities of 50,000 and 60,000 cells per well. After 3 days, cells were washed twice with ice-cold basal medium (135 mM NaCl, 3.5 mM KCl, 1.2 mM $MgSO_4$, 1.3 mM $CaCl_2$, 1.2 mM KH_2PO_4, 10 mM HEPES, 10 mM D-Glucose, pH 7.4, 290 mOsm). A total of 200 µL 5 mM HEPES/1 mM EDTA pH 7.4 buffer was added per well, and cells were vigorously scraped using a sterile cell scraper. Samples were sonicated for 4 minutes in ice-cold water. An aliquot of 70 µL was taken from each sample for protein quantification using the BCA assay (Thermo Fisher Scientific). Based on protein content, samples with matched protein levels were selected for HPLC analysis. Lysates were centrifuged at 13,400 × g for 4 minutes, and the supernatants were used for injection. High-performance liquid chromatography (HPLC) was performed using a Waters Acquity UHPLC equipped with a fluorescence detector (Waters) and a Eclipse XDB-C18 column (Agilent). The mobile phase, flow rate, and detection wavelength were adapted from the "long" gradient program as outlined by Perucho et al. (doi: 10.1007/s00726-015-1925-1). The gradient used two solvents (A) 0.05 M sodium acetate, pH 5.88 and methanol (95:5) in double distilled water and (B) methanol and double distilled water (70:30). The gradient program was 75% A for 0 to 2.5 minutes, gradient step to 67% A until 9.5 minutes, isocratic step to 40% A from 9.5 to 12.5 minutes, gradient step to 20% A until 21.5 minutes and held at 20% A until 24.5 minutes. To aid in cleaning the column the method ran at 100% B from 24.5 to 30 minutes. The flow rate was kept at 0.5 ml/min and detection wavelengths set to 240-450 nm (λ_{ex} – λ_{em}). Samples were added to HPLC vials and pre-column derivatized with 2-O-phthaldialdehyde (OPA) reagent solution (800 µl methanol, 7,140 µl borate buffer 0.4 M (pH 9.5) (Agilent), and 60 µl 3-mercaptoproprionic acid (Sigma Aldrich)). Derivatization and injection was performed using a programmable PAL HTC-xt autosampler system (LEAP Technologies). 20 µl of OPA was added to 40 µl of sample and after 1 minute, 10 µl of 5% acetic acid was added to stop the reaction. A final volume of 20 µl was injected onto the column.

Chromatograms were analyzed using the MassLynx 4.2 TargetLynx XS software. Retention times and peak areas were used for quantification relative to known standards.

Pathway analysis Proteomics screen

Proteomic datasets were analyzed using Ingenuity Pathway Analysis (IPA, Qiagen) to identify significantly enriched canonical pathways and upstream regulators. Differentially expressed proteins from MLBCs (wild-type and Lamtor1 knockout) cultured in either growth or tenogenic medium were uploaded into IPA. Proteins were filtered based on an abundance ratio (log_2) threshold of < -1 or > 1 and a p-value < 0.05. Pathway enrichment was determined using IPA's curated molecular interaction and functional annotation database, with statistical significance assessed by p-value and activation z-score. Results were visualized as bar plots indicating predicted pathway activation or inhibition.

Statistical analysis

Using Prism 8 software (GraphPad Software Inc, San Diego, CA), statistical analyses were conducted. Data are presented as mean ± SD. Differences between groups (e.g., genotypes) were assessed using one-way ANOVA or two-way ANOVA for treatment studies. The unpaired, non-parametric t- test was utilized for comparisons between two groups. Significance levels were set at *P ≤ 0.05, **P ≤ 0.01, ***P ≤ 0.001, and ****P ≤ 0.0001.

Data Availability

Data from Scx-gfp screens and LC-MS based proteomics are provided in Excel format as supplemental datasets. Source data from Scx-gfp screens and the code used for analysis will be made available on an approved repository upon peer review and/or publication. Source data are provided with this paper.

Code Availability

Code used for analysis will be made available on an approved repository upon acceptance of the manuscript for peer review and/or publication.

REFERENCES

1 Millar, N. L. *et al.* Tendinopathy. *Nat Rev Dis Primers* **7**, 1 (2021). https://doi.org/10.1038/s41572-020-00234-1

2 Salazar, V. S., Gamer, L. W. & Rosen, V. BMP signalling in skeletal development, disease and repair. *Nat Rev Endocrinol* **12**, 203-221 (2016). https://doi.org/10.1038/nrendo.2016.12

3 Howell, K. *et al.* Novel Model of Tendon Regeneration Reveals Distinct Cell Mechanisms Underlying Regenerative and Fibrotic Tendon Healing. *Sci Rep* **7**, 45238 (2017). https://doi.org/10.1038/srep45238

4 Sharma, P. & Maffulli, N. Tendon injury and tendinopathy: healing and repair. *J Bone Joint Surg Am* **87**, 187-202 (2005). https://doi.org/10.2106/JBJS.D.01850

5 Minikel, E. V., Painter, J. L., Dong, C. C. & Nelson, M. R. Refining the impact of genetic evidence on clinical success. *Nature* **629**, 624-629 (2024). https://doi.org/10.1038/s41586-024-07316-0

6 Pryce, B. A. *et al.* Recruitment and maintenance of tendon progenitors by TGFbeta signaling are essential for tendon formation. *Development* **136**, 1351-1361 (2009). https://doi.org/10.1242/dev.027342

7 Lorda-Diez, C. I., Montero, J. A., Martinez-Cue, C., Garcia-Porrero, J. A. & Hurle, J. M. Transforming growth factors beta coordinate cartilage and tendon differentiation in the developing limb mesenchyme. *J Biol Chem* **284**, 29988-29996 (2009). https://doi.org/10.1074/jbc.M109.014811

8 Tan, G. K. *et al.* Tgfbeta signaling is critical for maintenance of the tendon cell fate. *Elife* **9** (2020). https://doi.org/10.7554/eLife.52695

9 Mendias, C. L., Bakhurin, K. I. & Faulkner, J. A. Tendons of myostatin-deficient mice are small, brittle, and hypocellular. *Proc Natl Acad Sci U S A* **105**, 388-393 (2008). https://doi.org/10.1073/pnas.0707069105

10 Havis, E. *et al.* TGFbeta and FGF promote tendon progenitor fate and act downstream of muscle contraction to regulate tendon differentiation during chick limb development. *Development* **143**, 3839-3851 (2016). https://doi.org/10.1242/dev.136242

11 Schlesinger, S. Y. *et al.* Loss of Smad4 in the scleraxis cell lineage results in postnatal joint contracture. *Dev Biol* **470**, 108-120 (2021). https://doi.org/10.1016/j.ydbio.2020.11.006

12 Havis, E. *et al.* Transcriptomic analysis of mouse limb tendon cells during development. *Development* **141**, 3683-3696 (2014). https://doi.org/10.1242/dev.108654

13 Katzel, E. B. *et al.* The impact of Smad3 loss of function on TGF-beta signaling and radiation-induced capsular contracture. *Plast Reconstr Surg* **127**, 2263-2269 (2011). https://doi.org/10.1097/PRS.0b013e3182131bea

14 Neptune, E. R. *et al.* Dysregulation of TGF-beta activation contributes to pathogenesis in Marfan syndrome. *Nat Genet* **33**, 407-411 (2003). https://doi.org/10.1038/ng1116

15 Judge, D. P. & Dietz, H. C. Marfan's syndrome. *Lancet* **366**, 1965-1976 (2005). https://doi.org/10.1016/S0140-6736(05)67789-6

16 Mikic, B., Schalet, B. J., Clark, R. T., Gaschen, V. & Hunziker, E. B. GDF-5 deficiency in mice alters the ultrastructure, mechanical properties and composition of the Achilles tendon. *J Orthop Res* **19**, 365-371 (2001). https://doi.org/10.1016/S0736-0266(00)90018-4

17 Clark, R. T. *et al.* GDF-5 deficiency in mice leads to disruption of tail tendon form and function. *Connect Tissue Res* **42**, 175-186 (2001). https://doi.org/10.3109/03008200109005648

18 Wolfman, N. M. *et al.* Ectopic induction of tendon and ligament in rats by growth and differentiation factors 5, 6, and 7, members of the TGF-beta gene family. *J Clin Invest* **100**, 321-330 (1997). https://doi.org/10.1172/JCI119537

19 Schweitzer, R. *et al.* Analysis of the tendon cell fate using Scleraxis, a specific marker for tendons and ligaments. *Development* **128**, 3855-3866 (2001). https://doi.org/10.1242/dev.128.19.3855

20 Agarwal, S. *et al.* Scleraxis-Lineage Cells Contribute to Ectopic Bone Formation in Muscle and Tendon. *Stem Cells* **35**, 705-710 (2017). https://doi.org/10.1002/stem.2515

21 Dey, D. *et al.* Two tissue-resident progenitor lineages drive distinct phenotypes of heterotopic ossification. *Sci Transl Med* **8**, 366ra163 (2016). https://doi.org/10.1126/scitranslmed.aaf1090

22 Zhang, G. *et al.* Development of tendon structure and function: regulation of collagen fibrillogenesis. *J Musculoskelet Neuronal Interact* **5**, 5-21 (2005).

23 Sakabe, T. *et al.* Transcription factor scleraxis vitally contributes to progenitor lineage direction in wound healing of adult tendon in mice. *J Biol Chem* **293**, 5766-5780 (2018). https://doi.org/10.1074/jbc.RA118.001987

24 Ideo, K. *et al.* Role of Scx+/Sox9+ cells as potential progenitor cells for postnatal supraspinatus enthesis formation and healing after injury in mice. *PLoS One* **15**, e0242286 (2020). https://doi.org/10.1371/journal.pone.0242286

25 Chen, R., Zhou, X. & Skutella, T. A Tendon-Specific Double Reporter Transgenic Mouse Enables Tracking Cell Lineage and Functions Alteration In Vitro and In Vivo. *Int J Mol Sci* **22** (2021). https://doi.org/10.3390/ijms222011189

26 Huang, A. H. *et al.* Requirement for scleraxis in the recruitment of mesenchymal progenitors during embryonic tendon elongation. *Development* **146** (2019). https://doi.org/10.1242/dev.182782

27 Pryce, B. A., Brent, A. E., Murchison, N. D., Tabin, C. J. & Schweitzer, R. Generation of transgenic tendon reporters, ScxGFP and ScxAP, using regulatory elements of the scleraxis gene. *Dev Dyn* **236**, 1677-1682 (2007). https://doi.org/10.1002/dvdy.21179

28 Rosen, V. *et al.* Responsiveness of clonal limb bud cell lines to bone morphogenetic protein 2 reveals a sequential relationship between cartilage and bone cell phenotypes. *J Bone Miner Res* **9**, 1759-1768 (1994). https://doi.org/10.1002/jbmr.5650091113

29 Settembre, C., Fraldi, A., Medina, D. L. & Ballabio, A. Signals from the lysosome: a control centre for cellular clearance and energy metabolism. *Nat Rev Mol Cell Biol* **14**, 283-296 (2013). https://doi.org/10.1038/nrm3565

30 Lim, J. *et al.* mTORC1 Signaling is a Critical Regulator of Postnatal Tendon Development. *Sci Rep* **7**, 17175 (2017). https://doi.org/10.1038/s41598-017-17384-0

31 Blitz, E., Sharir, A., Akiyama, H. & Zelzer, E. Tendon-bone attachment unit is formed modularly by a distinct pool of Scx- and Sox9-positive progenitors. *Development* **140**, 2680-2690 (2013). https://doi.org/10.1242/dev.093906

32 Dehm, P. & Prockop, D. J. Time lag in the secretion of collagen by matrix-free tendon cells and inhibition of the secretory process by colchicine and vinblastine. *Biochim Biophys Acta* **264**, 375-382 (1972). https://doi.org/10.1016/0304-4165(72)90302-9

33 Bi, Y. *et al.* Identification of tendon stem/progenitor cells and the role of the extracellular matrix in their niche. *Nat Med* **13**, 1219-1227 (2007). https://doi.org/10.1038/nm1630

34 Young, R. G. *et al.* Use of mesenchymal stem cells in a collagen matrix for Achilles tendon repair. *J Orthop Res* **16**, 406-413 (1998). https://doi.org/10.1002/jor.1100160403

35 Murchison, N. D. *et al.* Regulation of tendon differentiation by scleraxis distinguishes force-transmitting tendons from muscle-anchoring tendons. *Development* **134**, 2697-2708 (2007). https://doi.org/10.1242/dev.001933

36 Ito, Y. *et al.* The Mohawk homeobox gene is a critical regulator of tendon differentiation. *Proc Natl Acad Sci U S A* **107**, 10538-10542 (2010). https://doi.org/10.1073/pnas.1000525107

37 Guerquin, M. J. *et al.* Transcription factor EGR1 directs tendon differentiation and promotes tendon repair. *J Clin Invest* **123**, 3564-3576 (2013). https://doi.org/10.1172/JCI67521

38 Lejard, V. *et al.* EGR1 and EGR2 involvement in vertebrate tendon differentiation. *J Biol Chem* **286**, 5855-5867 (2011). https://doi.org/10.1074/jbc.M110.153106

39 Passini, F. S. *et al.* Shear-stress sensing by PIEZO1 regulates tendon stiffness in rodents and influences jumping performance in humans. *Nat Biomed Eng* **5**, 1457-1471 (2021). https://doi.org/10.1038/s41551-021-00716-x

40 de Araujo, M. E. G. *et al.* Crystal structure of the human lysosomal mTORC1 scaffold complex and its impact on signaling. *Science* **358**, 377-381 (2017). https://doi.org/10.1126/science.aao1583

41 Yu, S. *et al.* Structural insights into cholesterol sensing by the LYCHOS-mTORC1 pathway. *Nat Commun* **16**, 6792 (2025). https://doi.org/10.1038/s41467-025-61966-w

42 Scott, A., Zahradnik, T. M., Squier, K., Beck, C. & Brunham, L. R. Diagnostic accuracy of ultrasound and MRI for Achilles tendon xanthoma in people with familial hypercholesterolemia: A systematic review. *J Clin Lipidol* **13**, 40-48 (2019). https://doi.org/10.1016/j.jacl.2018.10.013

43 Soslowsky, L. J. & Fryhofer, G. W. Tendon Homeostasis in Hypercholesterolemia. *Adv Exp Med Biol* **920**, 151-165 (2016). https://doi.org/10.1007/978-3-319-33943-6_14

44 Oosterveer, D. M., Versmissen, J., Yazdanpanah, M., Hamza, T. H. & Sijbrands, E. J. Differences in characteristics and risk of cardiovascular disease in familial hypercholesterolemia patients with and without tendon xanthomas: a systematic review and meta-analysis. *Atherosclerosis* **207**, 311-317 (2009). https://doi.org/10.1016/j.atherosclerosis.2009.04.009
45 Oosterveer, D. M. *et al.* The risk of tendon xanthomas in familial hypercholesterolaemia is influenced by variation in genes of the reverse cholesterol transport pathway and the low-density lipoprotein oxidation pathway. *Eur Heart J* **31**, 1007-1012 (2010). https://doi.org/10.1093/eurheartj/ehp538
46 Obrecht, M. *et al.* Magnetic resonance imaging and ultrasound elastography in the context of preclinical pharmacological research: significance for the 3R principles. *Front Pharmacol* **14**, 1177421 (2023). https://doi.org/10.3389/fphar.2023.1177421
47 Millar, N. L. *et al.* Targeting the IL-17A pathway for therapy in early-stage tendinopathy. *RMD Open* **11** (2025). https://doi.org/10.1136/rmdopen-2024-004729

Acknowledgements

We thank Beat Nyfeler for his autophagy expertise; Alain Schilb, Lukas Hils, and Angelika Meyer for their insights; Jens Richter, Edward Oakeley, Isabelle Fruh, Thierry Doll, Melanie Pellison, and Matthias Müller for their support with cell experiments; the team of Carsten Russ for performing the NGS sequencing to monitor the pooled CRISPR screens; Zinger Yang for processing the sequencing data; Rene Beerli, Najwa Ouali Alami, Carsten Jacobi, Dominic Hoepfner, Michael Bidinosti, Mark Nash, and Ina Kramer for their intellectual support throughout the project.

Author Contributions

S. P. and V.S. wrote the manuscript. C.N.P., and C.A. established cell lines and conducted CRISPR screens. S.P., B.J., D.E., M.H., A.S.C., I.G., C.A., H.B., I.C.Y., M.R., C.M., O.L., Y.L., C.M., C.P., and V.S. designed and conducted cell-based experiments and analyses. J.R.H designed lenti-vectors for MLB immortalization. F.N. analyzed barcode sequencing from the screen. M.A., T.N. and L.O. designed and synthesized therapeutic siRNA. F.D. generated the Lamtor1-null allele. D.E., M.H., M.O., C.M., S.P., N.A., and N.B. conducted animal experiments. J.M., S.B., and S.P. analyzed omics experiments. A.S. conducted amino acid assays. J.S., D.S., J.V., and S.P. performed lipidomics; A.V., J.V., and S.P. conducted proteomics. S.P., B.J., S.C., I.M., I.C., and V.U. ran the Fluopack screen. S.P., V.S., F.Z., Y.L., C.M., D.G., N.B., S.B., and C.N.P. contributed to manuscript development. V.S. and C.N.P. conceived the project. S.G.G. and M.K. supported strategy and resourcing. V.S. led the research.

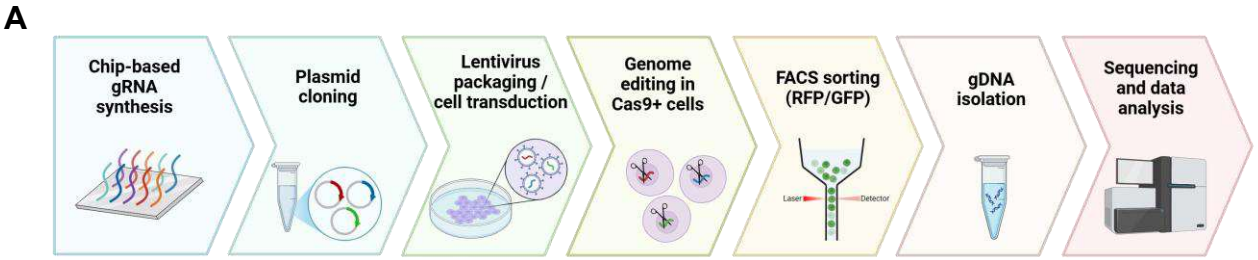
Funding

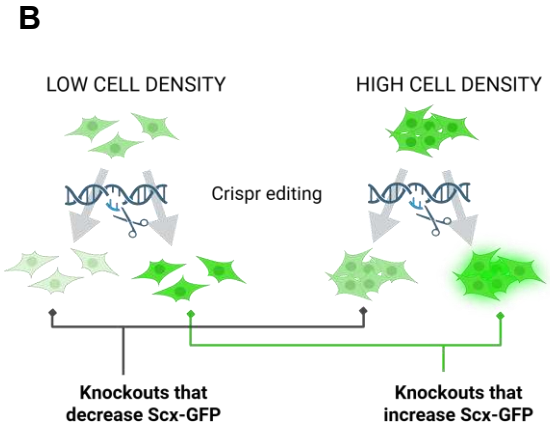
This work was supported by Novartis Pharma AG.

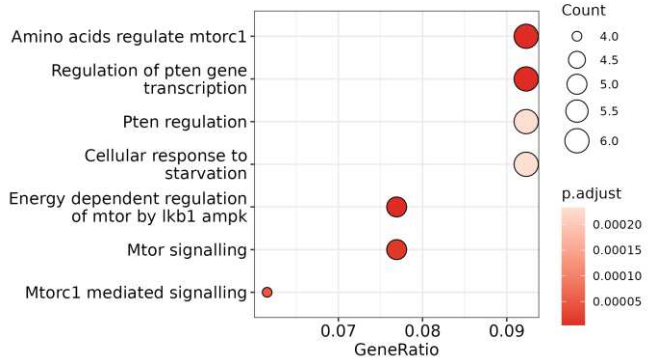
Competing Interests

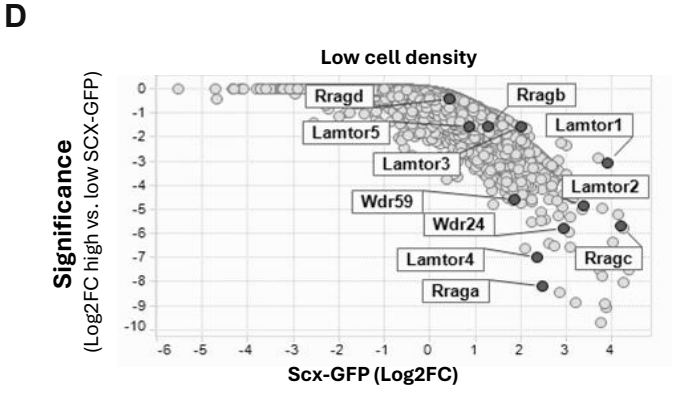
All authors were employed by Novartis Pharma AG during this work.

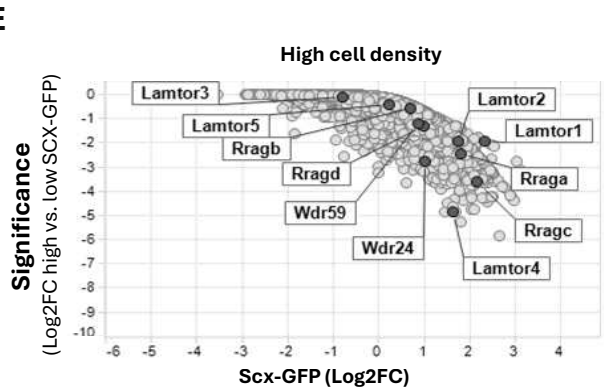
FIGURE 1

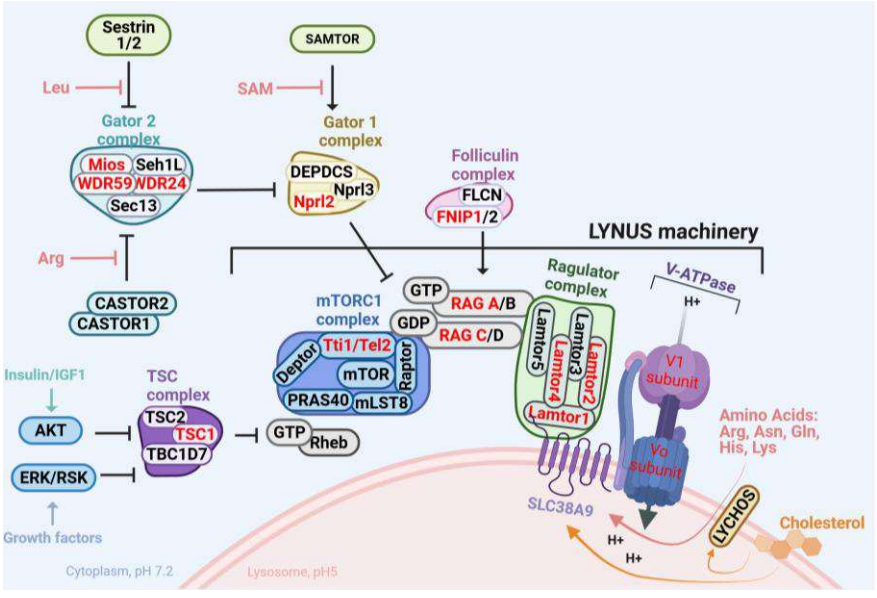

A
Chip-based gRNA synthesis
Plasmid cloning
Lentivirus packaging / cell transduction
Genome editing in Cas9+ cells
FACS sorting (RFP/GFP)
gDNA isolation
Sequencing and data analysis
Laser
Detector


B
LOW CELL DENSITY
HIGH CELL DENSITY
Crispr editing
Knockouts that decrease Scx-GFP
Knockouts that increase Scx-GFP


C
Amino acids regulate mtorc1
Regulation of pten gene transcription
Pten regulation
Cellular response to starvation
Energy dependent regulation of mtor by lkb1 ampk
Mtor signalling
Mtorc1 mediated signalling
0.07
0.08
0.09
GeneRatio
Count
4.0
4.5
5.0
5.5
6.0
p.adjust
0.00020
0.00015
0.00010
0.00005


D
Low cell density
Significance
(Log2FC high vs. low SCX-GFP)
Scx-GFP (Log2FC)
Rragd
Rragb
Lamtor5
Lamtor1
Lamtor3
Lamtor2
Wdr59
Wdr24
Lamtor4
Rragc
Rraga


E
High cell density
Significance
(Log2FC high vs. low SCX-GFP)
Scx-GFP (Log2FC)
Lamtor3
Lamtor2
Lamtor5
Lamtor1
Rragb
Rragd
Rraga
Wdr59
Rragc
Wdr24
Lamtor4


F
Sestrin 1/2
SAMTOR
Leu
SAM
Gator 2 complex
Gator 1 complex
Mios
Seh1L
WDR59
WDR24
Sec13
DEPDCS
Nprl3
Nprl2
Folliculin complex
FLCN
FNIP1/2
LYNUS machinery
Arg
CASTOR2
CASTOR1
mTORC1 complex
GTP
GDP
RAG A/B
RAG C/D
Ragulator complex
V-ATPase
H+
Deptor
Tti1/Tel2
mTOR
Raptor
PRAS40
mLST8
Lamtor5
Lamtor4
Lamtor3
Lamtor2
Lamtor1
V1 subunit
Vo subunit
Insulin/IGF1
TSC complex
AKT
TSC2
TSC1
TBC1D7
GTP
Rheb
ERK/RSK
Growth factors
Amino Acids: Arg, Asn, Gln, His, Lys
SLC38A9
LYCHOS
Cholesterol
H+
H+
Cytoplasm, pH 7.2
Lysosome, pH5

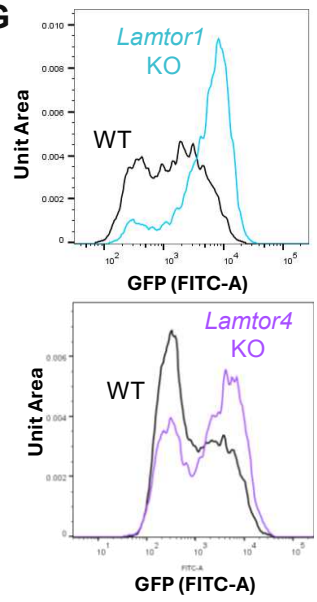

G
Lamtor1 KO
WT
Unit Area
GFP (FITC-A)
Lamtor4 KO
WT
Unit Area
GFP (FITC-A)

FIGURE 2

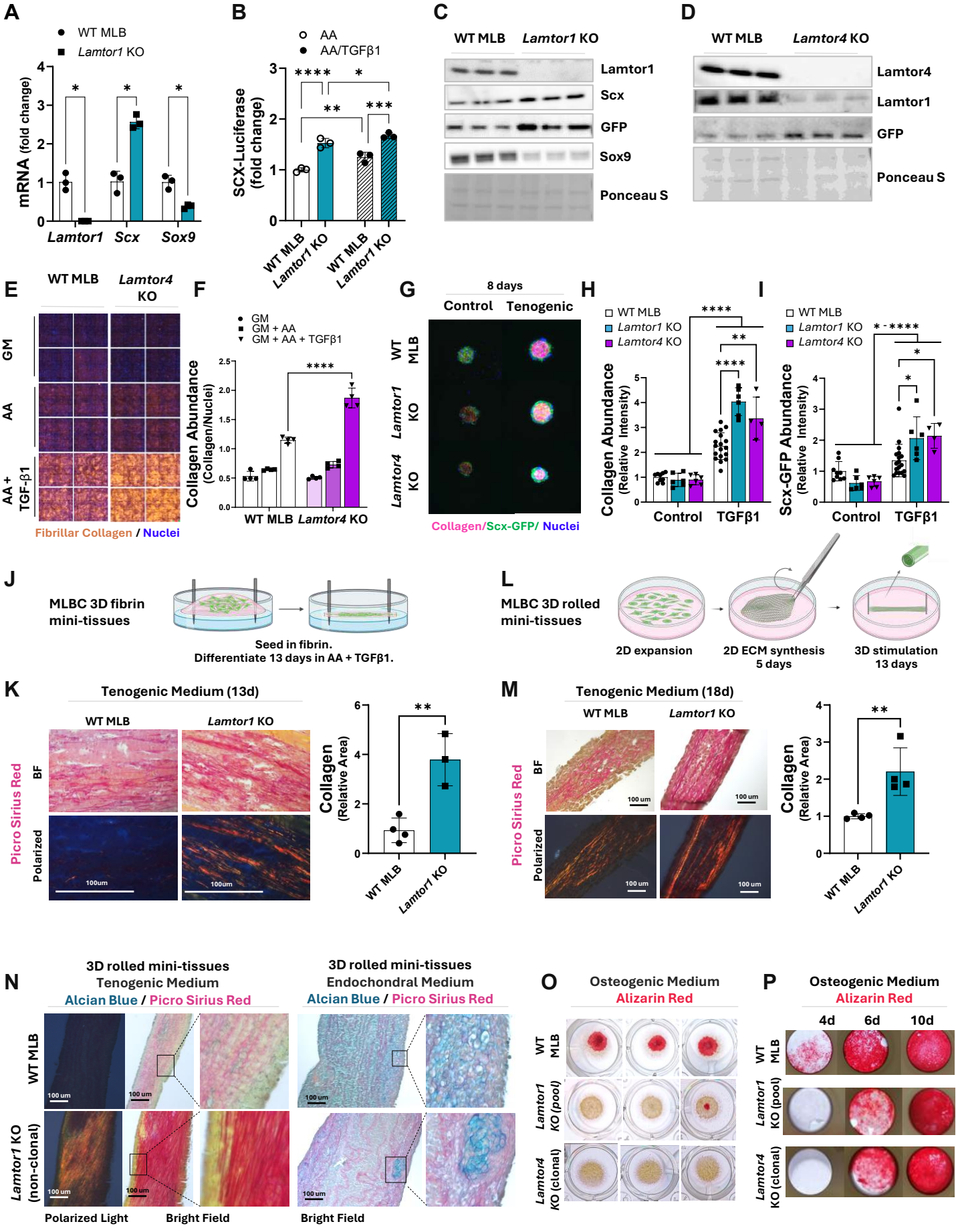

A
WT MLB
Lamtor1 KO
mRNA (fold change)
Lamtor1
Scx
Sox9
B
AA
AA/TGFβ1
SCX-Luciferase (fold change)
WT MLB
Lamtor1 KO
C
WT MLB
Lamtor1 KO
Lamtor1
Scx
GFP
Sox9
Ponceau S
D
WT MLB
Lamtor4 KO
Lamtor4
Lamtor1
GFP
Ponceau S
E
WT MLB
Lamtor4 KO
GM
AA
AA + TGF-β1
Fibrillar Collagen / Nuclei
F
GM
GM + AA
GM + AA + TGFβ1
Collagen Abundance (Collagen/Nuclei)
WT MLB
Lamtor4 KO
G
8 days
Control
Tenogenic
WT MLB
Lamtor1 KO
Lamtor4 KO
Collagen/Scx-GFP/ Nuclei
H
WT MLB
Lamtor1 KO
Lamtor4 KO
Collagen Abundance (Relative Intensity)
Control
TGFβ1
I
WT MLB
Lamtor1 KO
Lamtor4 KO
Scx-GFP Abundance (Relative Intensity)
Control
TGFβ1
J
MLBC 3D fibrin mini-tissues
Seed in fibrin.
Differentiate 13 days in AA + TGFβ1.
L
MLBC 3D rolled mini-tissues
2D expansion
2D ECM synthesis 5 days
3D stimulation 13 days
K
Tenogenic Medium (13d)
WT MLB
Lamtor1 KO
Picro Sirius Red
BF
Polarized
100um
Collagen (Relative Area)
WT MLB
Lamtor1 KO
M
Tenogenic Medium (18d)
WT MLB
Lamtor1 KO
Picro Sirius Red
BF
Polarized
100 um
Collagen (Relative Area)
WT MLB
Lamtor1 KO
N
3D rolled mini-tissues
Tenogenic Medium
Alcian Blue / Picro Sirius Red
3D rolled mini-tissues
Endochondral Medium
Alcian Blue / Picro Sirius Red
WT MLB
Lamtor1 KO (non-clonal)
100 um
Polarized Light
Bright Field
Bright Field
O
Osteogenic Medium
Alizarin Red
WT MLB
Lamtor1 KO (pool)
Lamtor4 KO (clonal)
P
Osteogenic Medium
Alizarin Red
4d
6d
10d
WT MLB
Lamtor1 KO (pool)
Lamtor4 KO (clonal)

FIGURE 3

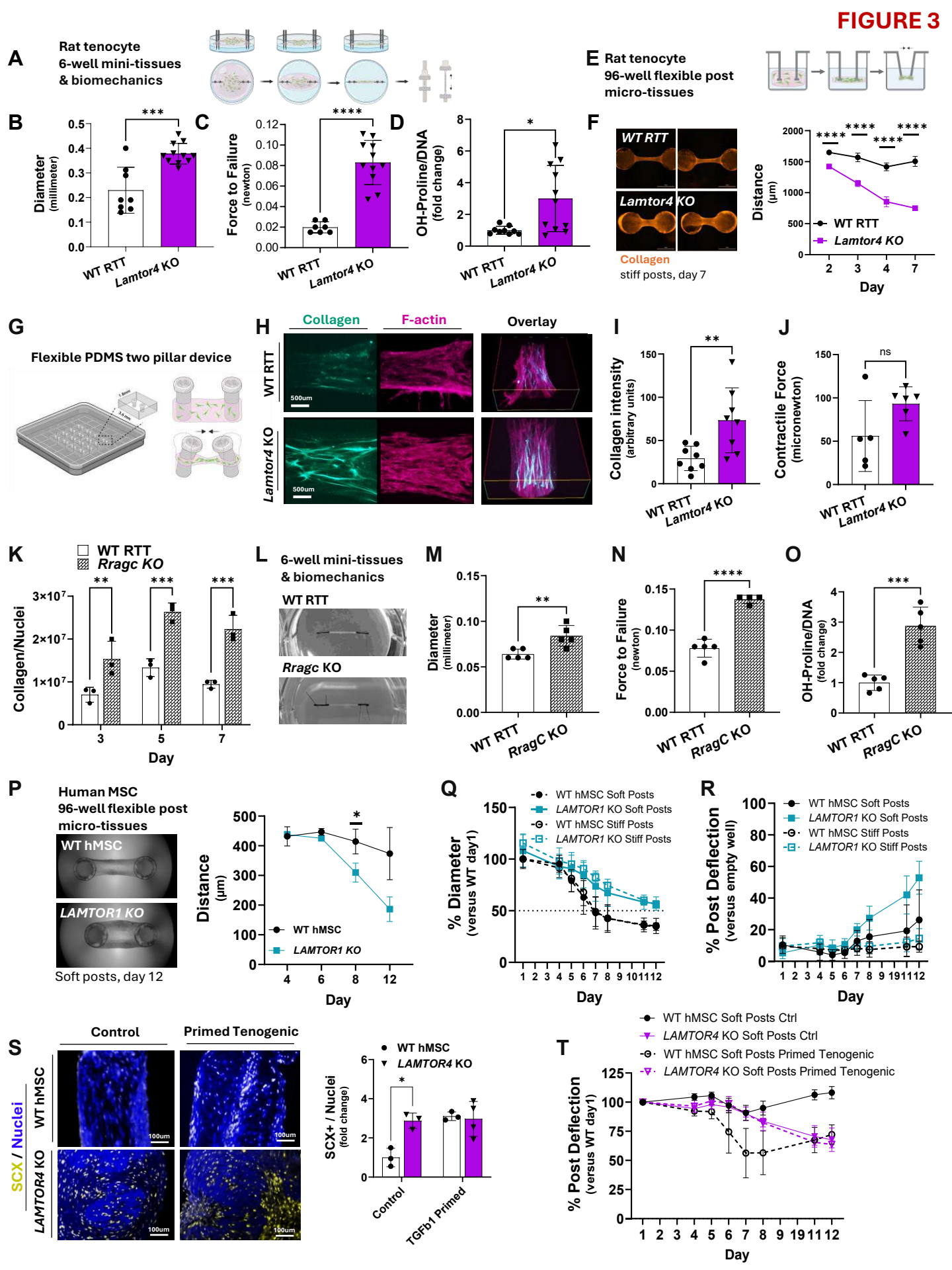

A
Rat tenocyte
6-well mini-tissues
& biomechanics
E
Rat tenocyte
96-well flexible post
micro-tissues
B
Diameter (millimeter)
WT RTT
Lamtor4 KO
C
Force to Failure (newton)
D
OH-Proline/DNA (fold change)
F
WT RTT
Lamtor4 KO
Collagen
stiff posts, day 7
Distance (µm)
Day
G
Flexible PDMS two pillar device
H
Collagen
F-actin
Overlay
500um
I
Collagen intensity (arbitrary units)
J
Contractile Force (micronewton)
ns
K
WT RTT
Rragc KO
Collagen/Nuclei
L
6-well mini-tissues
& biomechanics
M
N
O
RragC KO
P
Human MSC
96-well flexible post
micro-tissues
WT hMSC
LAMTOR1 KO
Soft posts, day 12
Q
WT hMSC Soft Posts
LAMTOR1 KO Soft Posts
WT hMSC Stiff Posts
LAMTOR1 KO Stiff Posts
% Diameter (versus WT day1)
R
% Post Deflection (versus empty well)
S
Control
Primed Tenogenic
SCX / Nuclei
LAMTOR4 KO
SCX+ / Nuclei (fold change)
TGFb1 Primed
T
WT hMSC Soft Posts Ctrl
LAMTOR4 KO Soft Posts Ctrl
WT hMSC Soft Posts Primed Tenogenic
LAMTOR4 KO Soft Posts Primed Tenogenic
% Post Deflection (versus WT day1)

FIGURE 4

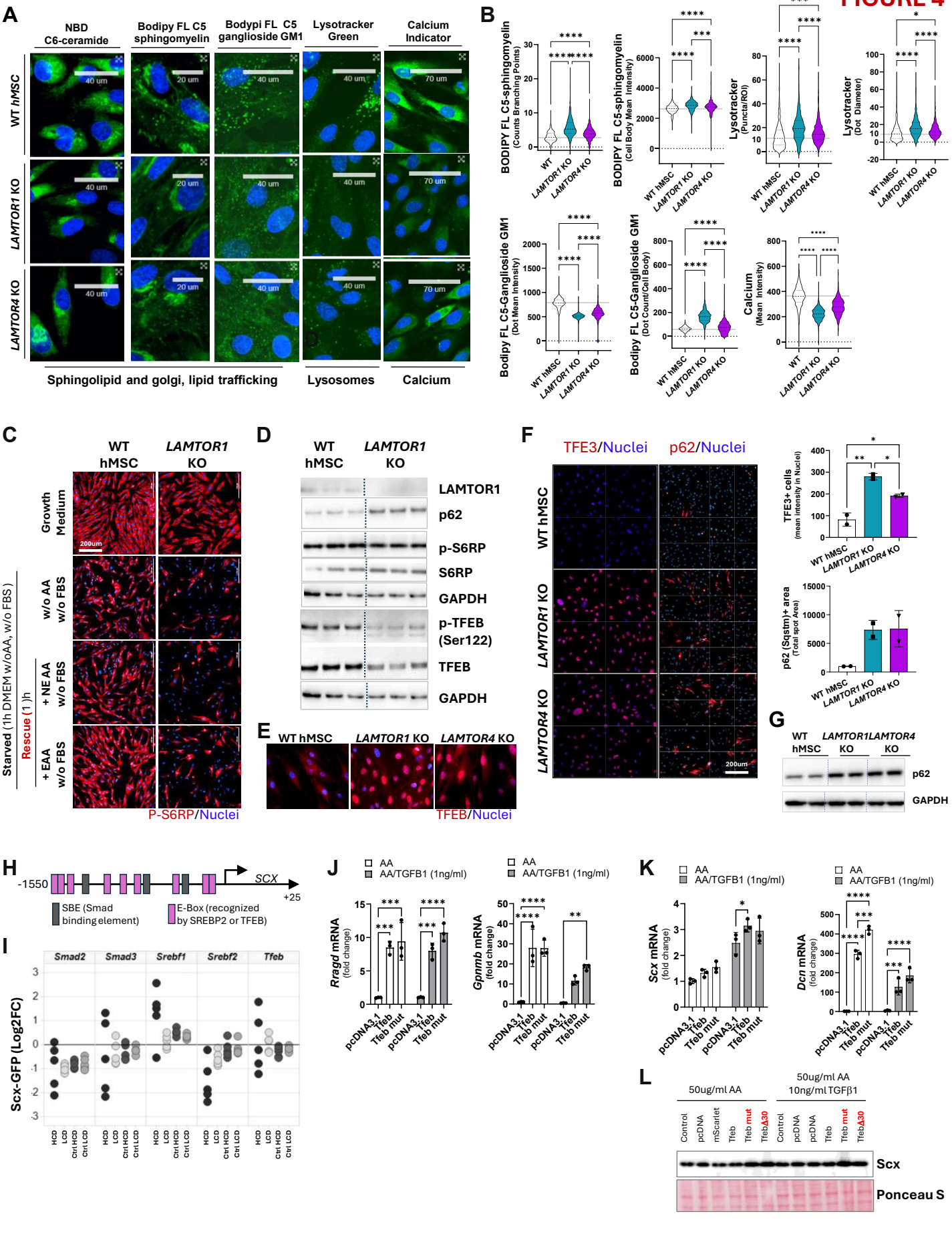

A
NBD C6-ceramide
Bodipy FL C5 sphingomyelin
Bodypi FL C5 ganglioside GM1
Lysotracker Green
Calcium Indicator
WT hMSC
LAMTOR1 KO
LAMTOR4 KO
Sphingolipid and golgi, lipid trafficking
Lysosomes
Calcium
B
BODIPY FL C5-sphingomyelin (Counts Branching Points)
BODIPY FL C5-sphingomyelin (Cell Body Mean Intensity)
Lysotracker (Puncta/ROI)
Lysotracker (Dot Diameter)
Bodipy FL C5-Ganglioside GM1 (Dot Mean Intensity)
Bodipy FL C5-Ganglioside GM1 (Dot Count/Cell Body)
Calcium (Mean Intensity)
C
WT hMSC
LAMTOR1 KO
Growth Medium
w/o AA w/o FBS
+ NE AA w/o FBS
+ EAA w/o FBS
Starved (1h DMEM w/oAA, w/o FBS)
Rescue (1)h
P-S6RP/Nuclei
D
LAMTOR1
p62
p-S6RP
S6RP
GAPDH
p-TFEB (Ser122)
TFEB
GAPDH
E
WT hMSC
LAMTOR1 KO
LAMTOR4 KO
TFEB/Nuclei
F
TFE3/Nuclei
p62/Nuclei
WT hMSC
LAMTOR1 KO
LAMTOR4 KO
TFE3+ cells (mean intensity in Nuclei)
p62 (Sqstm)+ area (Total spot Area)
G
WT hMSC
LAMTOR1 KO
LAMTOR4 KO
p62
GAPDH
H
-1550
SCX
+25
SBE (Smad binding element)
E-Box (recognized by SREBP2 or TFEB)
I
Smad2
Smad3
Srebf1
Srebf2
Tfeb
Scx-GFP (Log2FC)
HCD
LCD
Ctrl HCD
Ctrl LCD
J
AA
AA/TGFB1 (1ng/ml)
Rragd mRNA (fold change)
Gpnmb mRNA (fold change)
pcDNA3.1
Tfeb
Tfeb mut
K
Scx mRNA (fold change)
Dcn mRNA (fold change)
L
50ug/ml AA
50ug/ml AA 10ng/ml TGFβ1
Control
pcDNA
mScarlet
Tfeb
Tfeb mut
TfebΔ30
Scx
Ponceau S

FIGURE 5

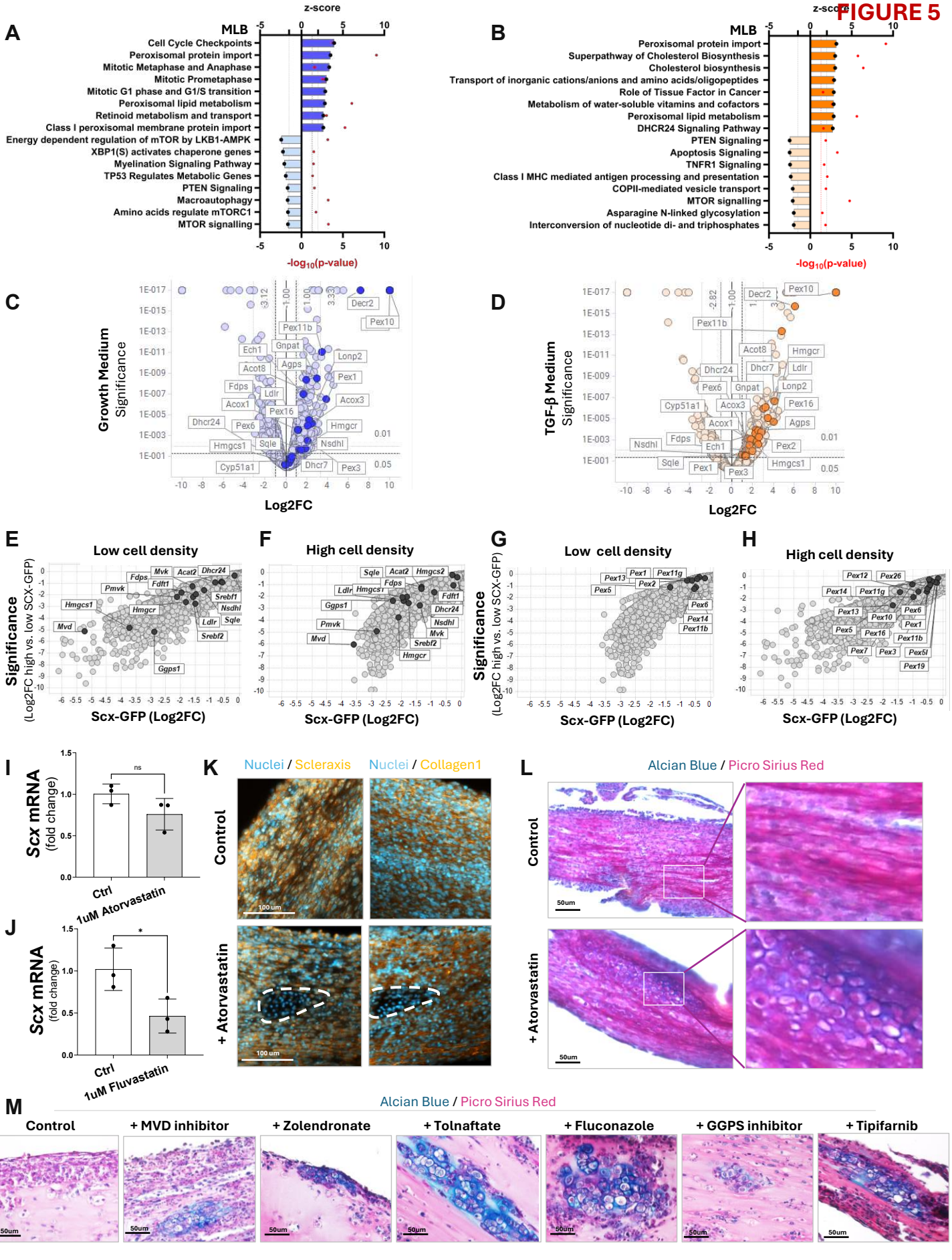

A
MLB
z-score
Cell Cycle Checkpoints
Peroxisomal protein import
Mitotic Metaphase and Anaphase
Mitotic Prometaphase
Mitotic G1 phase and G1/S transition
Peroxisomal lipid metabolism
Retinoid metabolism and transport
Class I peroxisomal membrane protein import
Energy dependent regulation of mTOR by LKB1-AMPK
XBP1(S) activates chaperone genes
Myelination Signaling Pathway
TP53 Regulates Metabolic Genes
PTEN Signaling
Macroautophagy
Amino acids regulate mTORC1
MTOR signalling
-log10(p-value)
B
MLB
z-score
Peroxisomal protein import
Superpathway of Cholesterol Biosynthesis
Cholesterol biosynthesis
Transport of inorganic cations/anions and amino acids/oligopeptides
Role of Tissue Factor in Cancer
Metabolism of water-soluble vitamins and cofactors
Peroxisomal lipid metabolism
DHCR24 Signaling Pathway
PTEN Signaling
Apoptosis Signaling
TNFR1 Signaling
Class I MHC mediated antigen processing and presentation
COPII-mediated vesicle transport
MTOR signalling
Asparagine N-linked glycosylation
Interconversion of nucleotide di- and triphosphates
-log10(p-value)
C
Growth Medium
Significance
Log2FC
D
TGF-β Medium
Significance
Log2FC
E
Low cell density
Significance
(Log2FC high vs. low SCX-GFP)
Scx-GFP (Log2FC)
F
High cell density
Scx-GFP (Log2FC)
G
Low cell density
Significance
(Log2FC high vs. low SCX-GFP)
Scx-GFP (Log2FC)
H
High cell density
Scx-GFP (Log2FC)
I
Scx mRNA
(fold change)
ns
Ctrl
1uM Atorvastatin
J
Scx mRNA
(fold change)
*
Ctrl
1uM Fluvastatin
K
Nuclei / Scleraxis
Nuclei / Collagen1
Control
+ Atorvastatin
100 um
L
Alcian Blue / Picro Sirius Red
Control
+ Atorvastatin
50um
M
Alcian Blue / Picro Sirius Red
Control
+ MVD inhibitor
+ Zolendronate
+ Tolnaftate
+ Fluconazole
+ GGPS inhibitor
+ Tipifarnib
50um

FIGURE 6

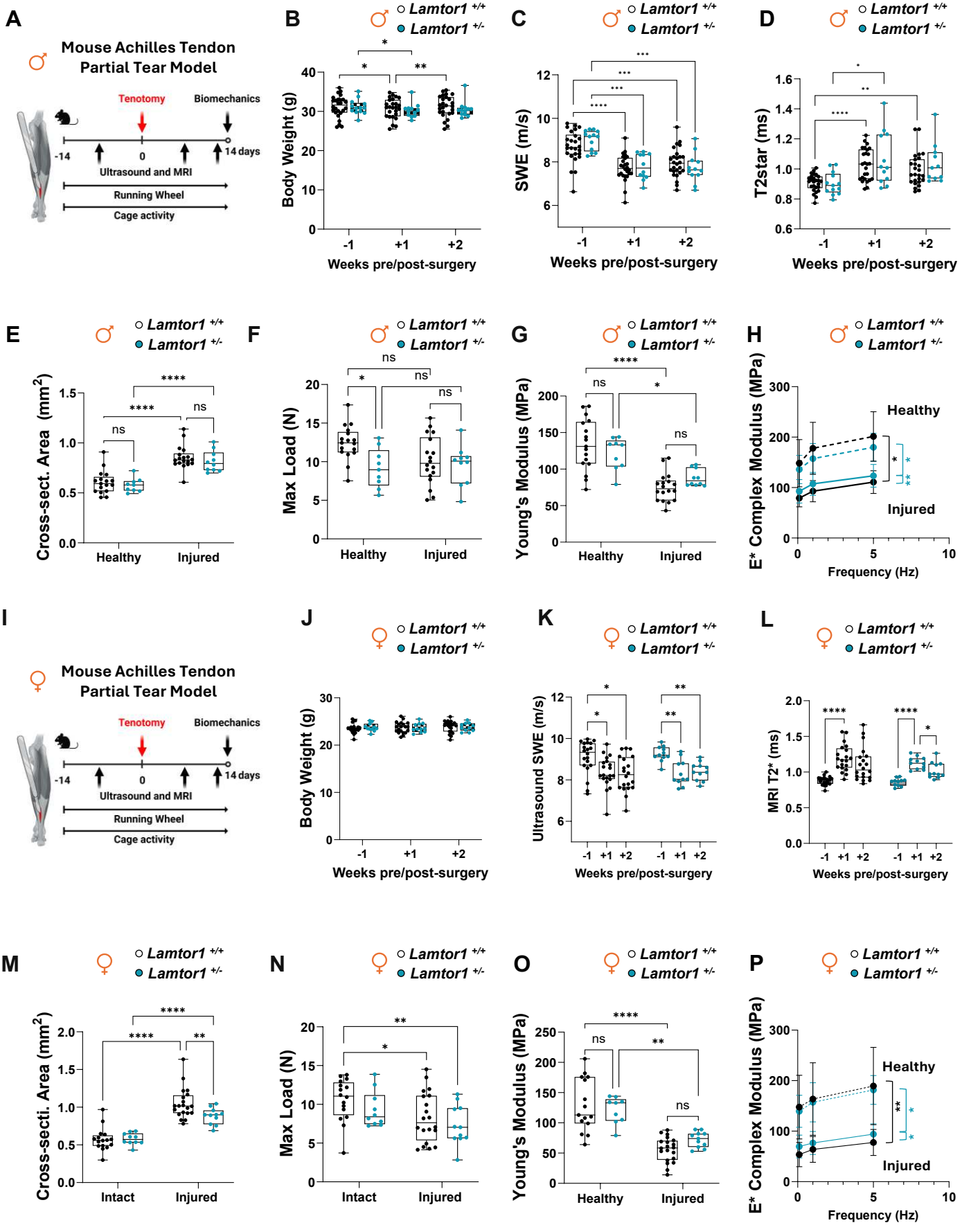

A
Mouse Achilles Tendon Partial Tear Model
Tenotomy
Biomechanics
-14
0
14 days
Ultrasound and MRI
Running Wheel
Cage activity
B
Lamtor1 +/+
Lamtor1 +/-
Body Weight (g)
Weeks pre/post-surgery
C
SWE (m/s)
Weeks pre/post-surgery
D
T2star (ms)
Weeks pre/post-surgery
E
Cross-sect. Area (mm2)
Healthy
Injured
F
Max Load (N)
Healthy
Injured
G
Young's Modulus (MPa)
Healthy
Injured
H
E* Complex Modulus (MPa)
Healthy
Injured
Frequency (Hz)
I
Mouse Achilles Tendon Partial Tear Model
Tenotomy
Biomechanics
-14
0
14 days
Ultrasound and MRI
Running Wheel
Cage activity
J
Body Weight (g)
Weeks pre/post-surgery
K
Ultrasound SWE (m/s)
Weeks pre/post-surgery
L
MRI T2* (ms)
Weeks pre/post-surgery
M
Cross-secti. Area (mm2)
Intact
Injured
N
Max Load (N)
Intact
Injured
O
Young's Modulus (MPa)
Healthy
Injured
P
E* Complex Modulus (MPa)
Healthy
Injured
Frequency (Hz)

FIGURE 7

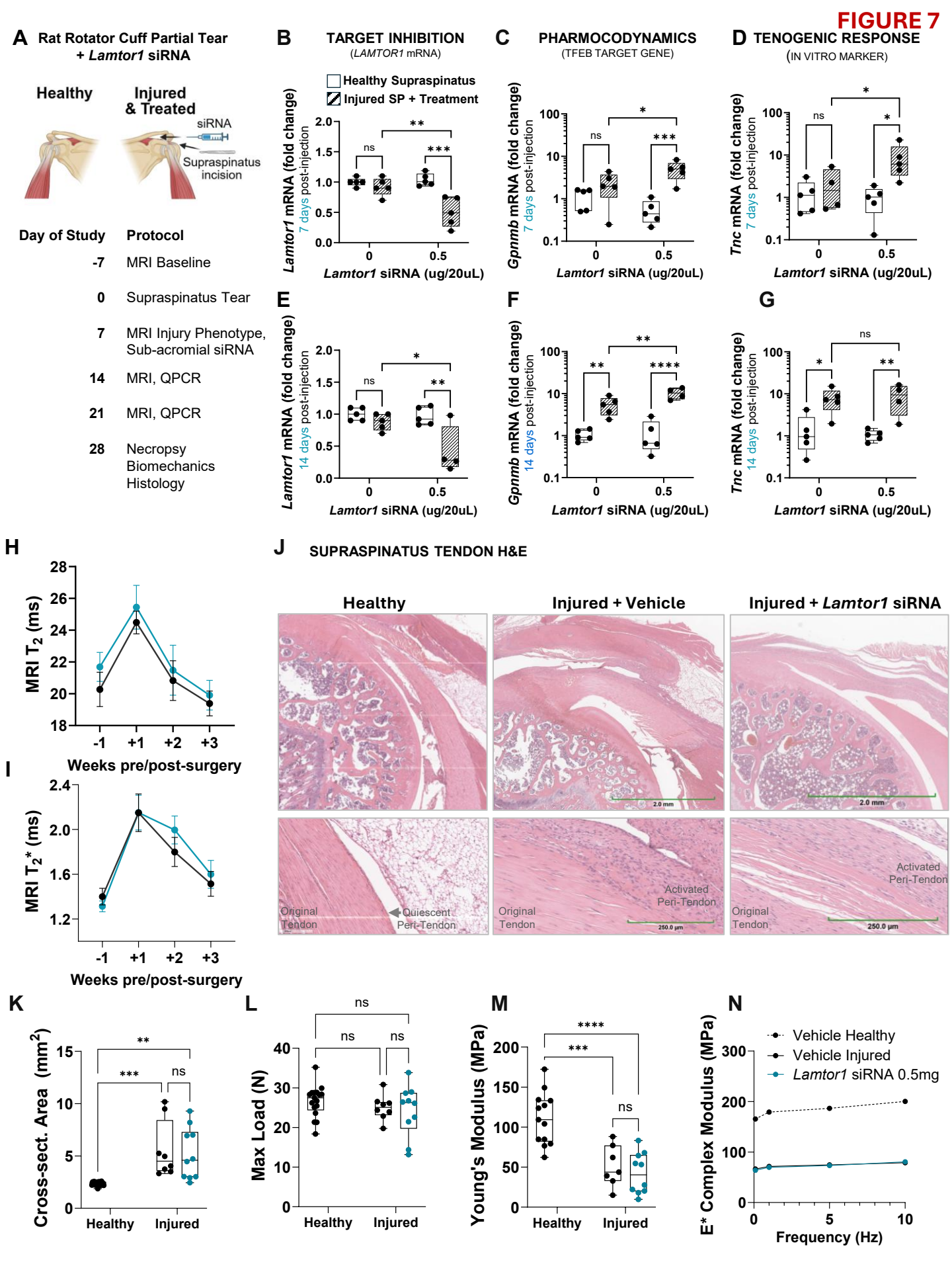

A Rat Rotator Cuff Partial Tear + Lamtor1 siRNA
Healthy
Injured & Treated
siRNA
Supraspinatus incision
Day of Study
Protocol
-7 MRI Baseline
0 Supraspinatus Tear
7 MRI Injury Phenotype, Sub-acromial siRNA
14 MRI, QPCR
21 MRI, QPCR
28 Necropsy Biomechanics Histology
B TARGET INHIBITION (LAMTOR1 mRNA)
Healthy Supraspinatus
Injured SP + Treatment
Lamtor1 mRNA (fold change) 7 days post-injection
Lamtor1 siRNA (ug/20uL)
C PHARMACODYNAMICS (TFEB TARGET GENE)
Gpnmb mRNA (fold change) 7 days post-injection
Lamtor1 siRNA (ug/20uL)
D TENOGENIC RESPONSE (IN VITRO MARKER)
Tnc mRNA (fold change) 7 days post-injection
Lamtor1 siRNA (ug/20uL)
E
Lamtor1 mRNA (fold change) 14 days post-injection
Lamtor1 siRNA (ug/20uL)
F
Gpnmb mRNA (fold change) 14 days post-injection
Lamtor1 siRNA (ug/20uL)
G
Tnc mRNA (fold change) 14 days post-injection
Lamtor1 siRNA (ug/20uL)
H
MRI T2 (ms)
Weeks pre/post-surgery
I
MRI T2* (ms)
Weeks pre/post-surgery
J SUPRASPINATUS TENDON H&E
Healthy
Injured + Vehicle
Injured + Lamtor1 siRNA
Original Tendon
Quiescent Peri-Tendon
Activated Peri-Tendon
2.0 mm
250.0 µm
K
Cross-sect. Area (mm2)
Healthy
Injured
L
Max Load (N)
Healthy
Injured
M
Young's Modulus (MPa)
Healthy
Injured
N
Vehicle Healthy
Vehicle Injured
Lamtor1 siRNA 0.5mg
E* Complex Modulus (MPa)
Frequency (Hz)

FIGURE S1

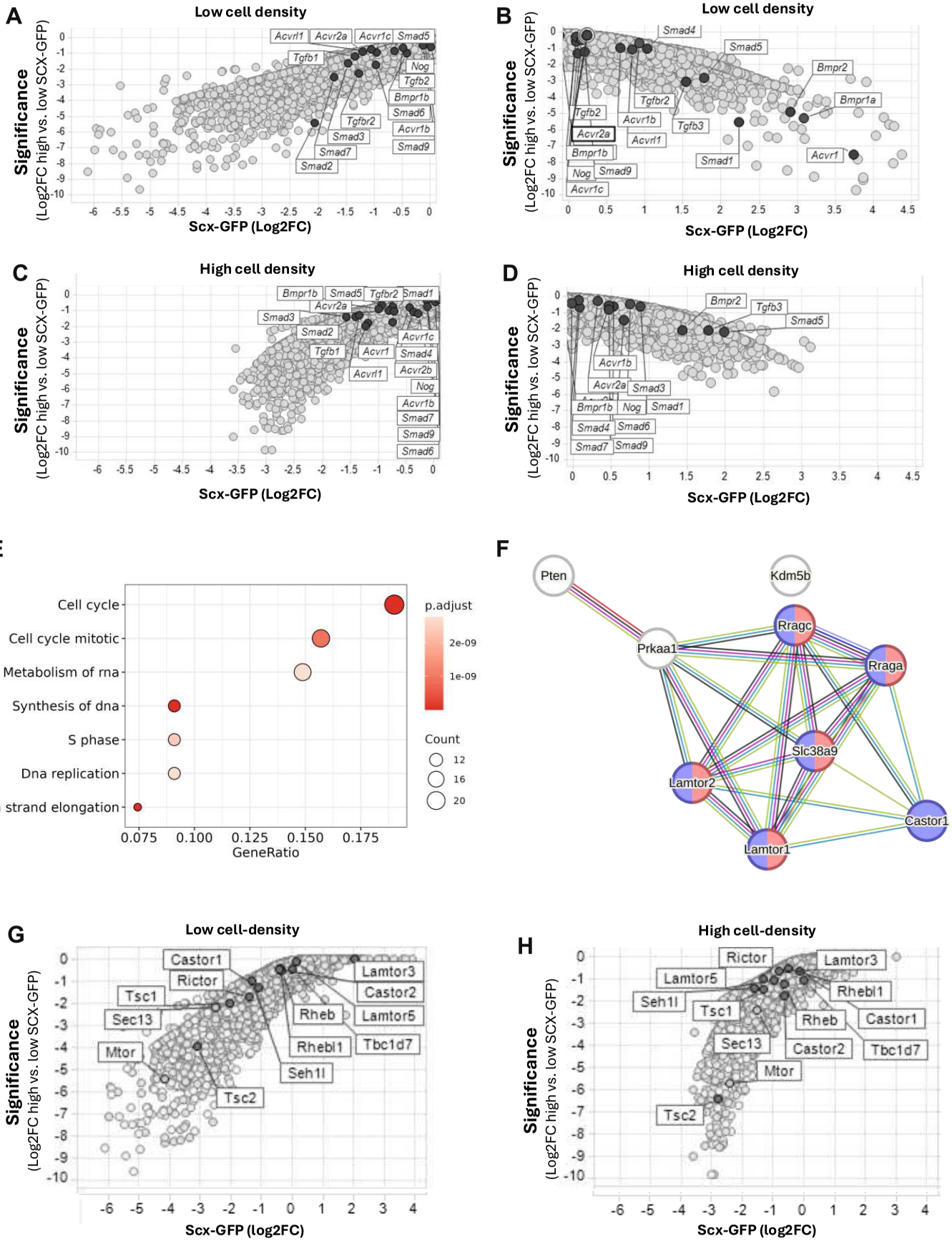

A
Low cell density
Significance
(Log2FC high vs. low SCX-GFP)
Scx-GFP (Log2FC)
Acvrl1
Acvr2a
Acvr1c
Smad5
Tgfb1
Nog
Tgfb2
Bmpr1b
Smad6
Tgfbr2
Acvr1b
Smad3
Smad9
Smad7
Smad2
B
Low cell density
Smad4
Smad5
Bmpr2
Bmpr1a
Tgfbr2
Tgfb2
Acvr1b
Tgfb3
Acvr2a
Acvrl1
Smad1
Acvr1
Bmpr1b
Nog
Smad9
Acvr1c
C
High cell density
Bmpr1b
Smad5
Tgfbr2
Smad1
Acvr2a
Smad3
Smad2
Acvr1c
Tgfb1
Acvr1
Smad4
Acvrl1
Acvr2b
Nog
Acvr1b
Smad7
Smad9
Smad6
D
High cell density
Bmpr2
Tgfb3
Smad5
Acvr1b
Acvr2a
Smad3
Bmpr1b
Nog
Smad1
Smad4
Smad6
Smad7
Smad9
E
Cell cycle
Cell cycle mitotic
Metabolism of rna
Synthesis of dna
S phase
Dna replication
Dna strand elongation
GeneRatio
p.adjust
2e-09
1e-09
Count
12
16
20
F
Pten
Kdm5b
Rragc
Prkaa1
Rraga
Slc38a9
Lamtor2
Castor1
Lamtor1
G
Low cell-density
Significance
(Log2FC high vs. low SCX-GFP)
Scx-GFP (log2FC)
Castor1
Rictor
Lamtor3
Tsc1
Castor2
Sec13
Rheb
Lamtor5
Mtor
Rhebl1
Tbc1d7
Seh1l
Tsc2
H
High cell-density
Rictor
Lamtor3
Lamtor5
Rhebl1
Seh1l
Tsc1
Rheb
Castor1
Sec13
Castor2
Tbc1d7
Mtor
Tsc2

FIGURE S2

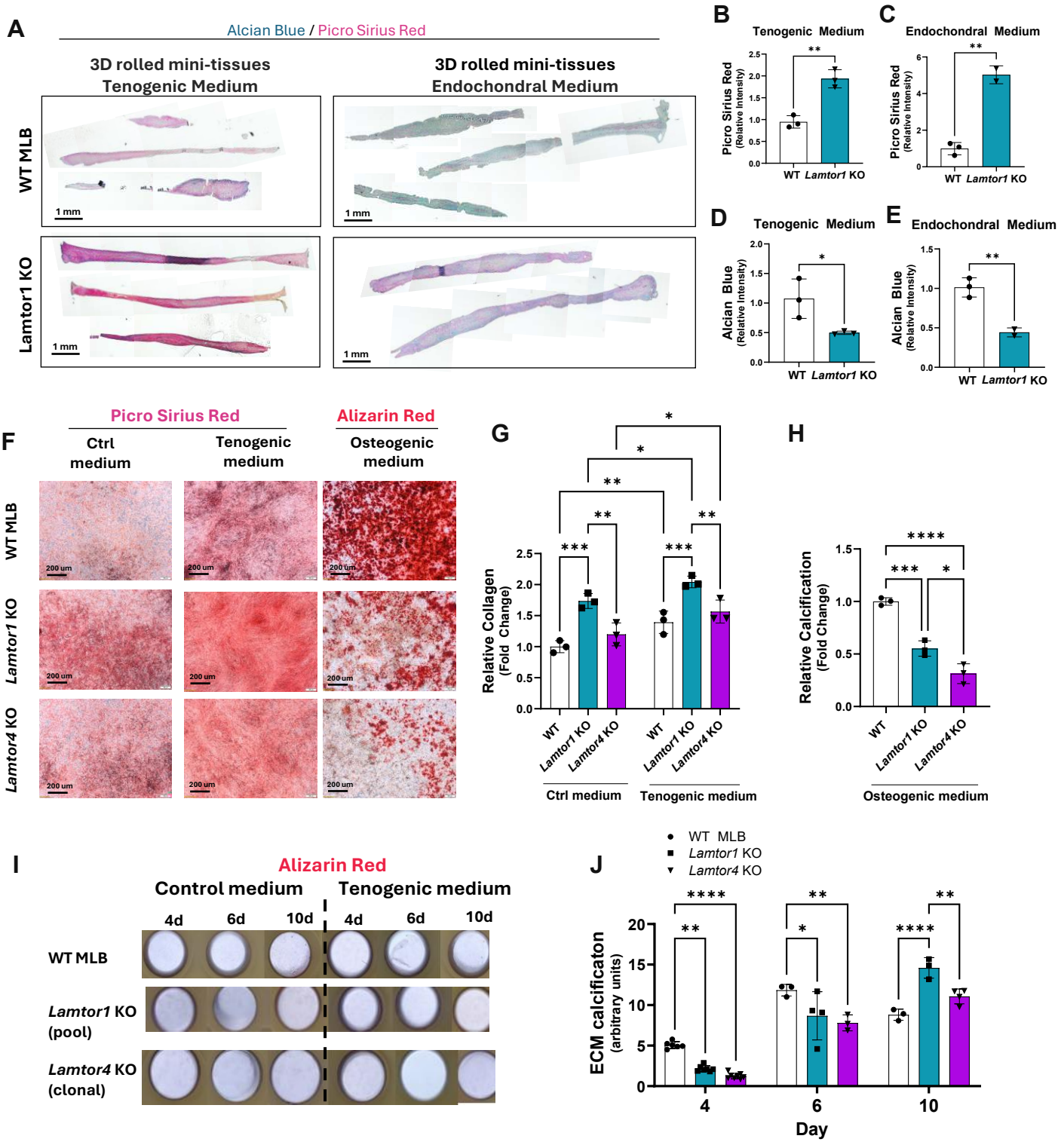

A
Alcian Blue / Picro Sirius Red
3D rolled mini-tissues
Tenogenic Medium
3D rolled mini-tissues
Endochondral Medium
WT MLB
Lamtor1 KO
1 mm
B
Tenogenic Medium
Picro Sirius Red
(Relative Intensity)
WT Lamtor1 KO
C
Endochondral Medium
Picro Sirius Red
(Relative Intensity)
WT Lamtor1 KO
D
Tenogenic Medium
Alcian Blue
(Relative Intensity)
WT Lamtor1 KO
E
Endochondral Medium
Alcian Blue
(Relative Intensity)
WT Lamtor1 KO
F
Picro Sirius Red
Alizarin Red
Ctrl medium
Tenogenic medium
Osteogenic medium
WT MLB
Lamtor1 KO
Lamtor4 KO
200 um
G
Relative Collagen
(Fold Change)
WT
Lamtor1 KO
Lamtor4 KO
Ctrl medium
Tenogenic medium
H
Relative Calcification
(Fold Change)
WT
Lamtor1 KO
Lamtor4 KO
Osteogenic medium
I
Alizarin Red
Control medium
Tenogenic medium
4d
6d
10d
WT MLB
Lamtor1 KO
(pool)
Lamtor4 KO
(clonal)
J
WT MLB
Lamtor1 KO
Lamtor4 KO
ECM calcificaton
(arbitrary units)
Day

FIGURE S3

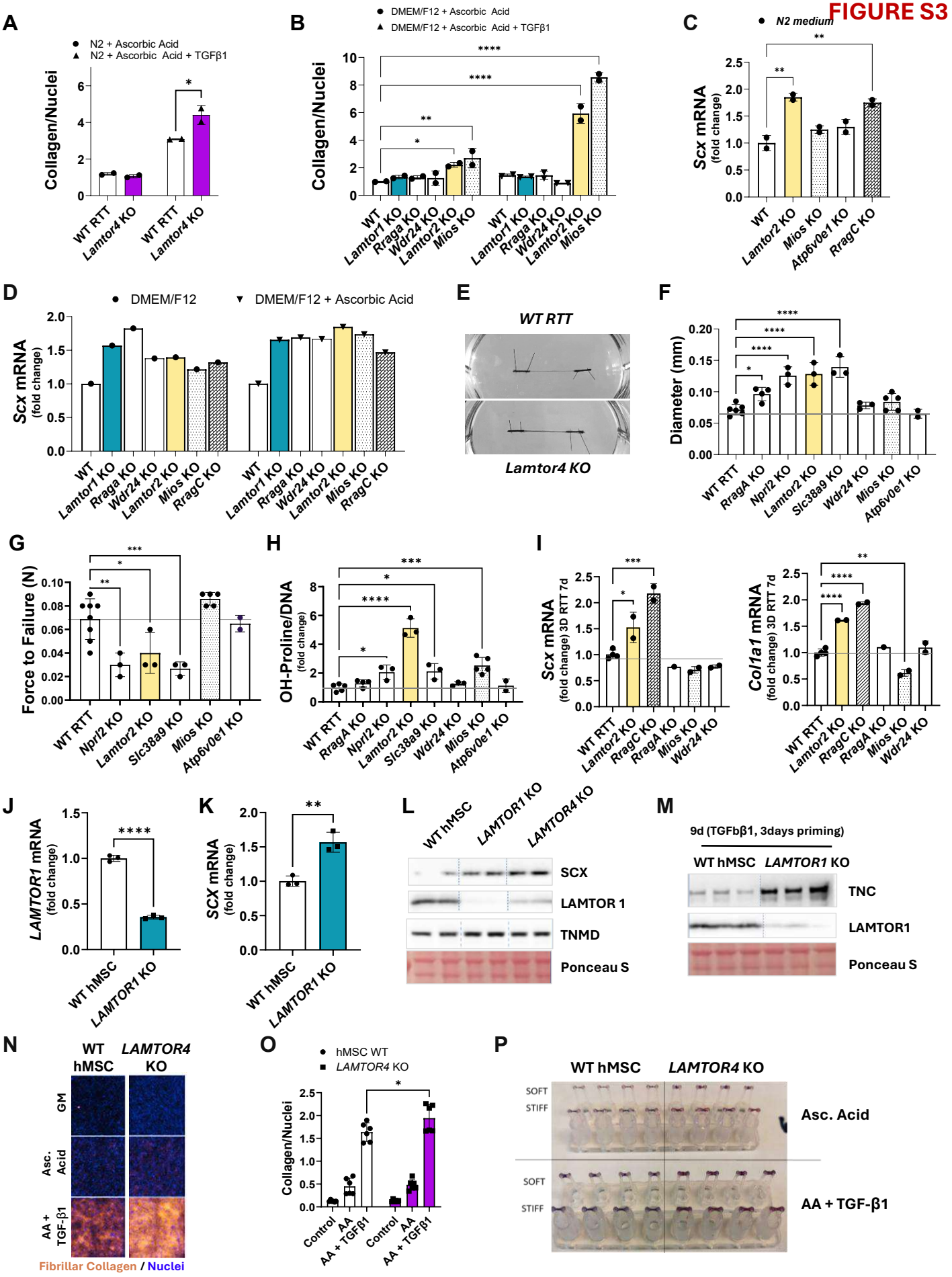

A
N2 + Ascorbic Acid
N2 + Ascorbic Acid + TGFβ1
Collagen/Nuclei
WT RTT
Lamtor4 KO
B
DMEM/F12 + Ascorbic Acid
DMEM/F12 + Ascorbic Acid + TGFβ1
Collagen/Nuclei
WT
Lamtor1 KO
Rraga KO
Wdr24 KO
Lamtor2 KO
Mios KO
RragC KO
C
N2 medium
Scx mRNA (fold change)
D
DMEM/F12
DMEM/F12 + Ascorbic Acid
Scx mRNA (fold change)
E
WT RTT
Lamtor4 KO
F
Diameter (mm)
WT RTT
RragA KO
Nprl2 KO
Lamtor2 KO
Slc38a9 KO
Wdr24 KO
Mios KO
Atp6v0e1 KO
G
Force to Failure (N)
H
OH-Proline/DNA (fold change)
I
Scx mRNA (fold change) 3D RTT 7d
Col1a1 mRNA (fold change) 3D RTT 7d
J
LAMTOR1 mRNA (fold change)
WT hMSC
LAMTOR1 KO
K
SCX mRNA (fold change)
L
WT hMSC
LAMTOR1 KO
LAMTOR4 KO
SCX
LAMTOR 1
TNMD
Ponceau S
M
9d (TGFbβ1, 3days priming)
WT hMSC
LAMTOR1 KO
TNC
LAMTOR1
Ponceau S
N
WT hMSC
LAMTOR4 KO
GM
Asc. Acid
AA + TGF-β1
Fibrillar Collagen / Nuclei
O
hMSC WT
LAMTOR4 KO
Collagen/Nuclei
Control
AA
AA + TGFβ1
P
WT hMSC
LAMTOR4 KO
SOFT
STIFF
Asc. Acid
AA + TGF-β1

FIGURE S4

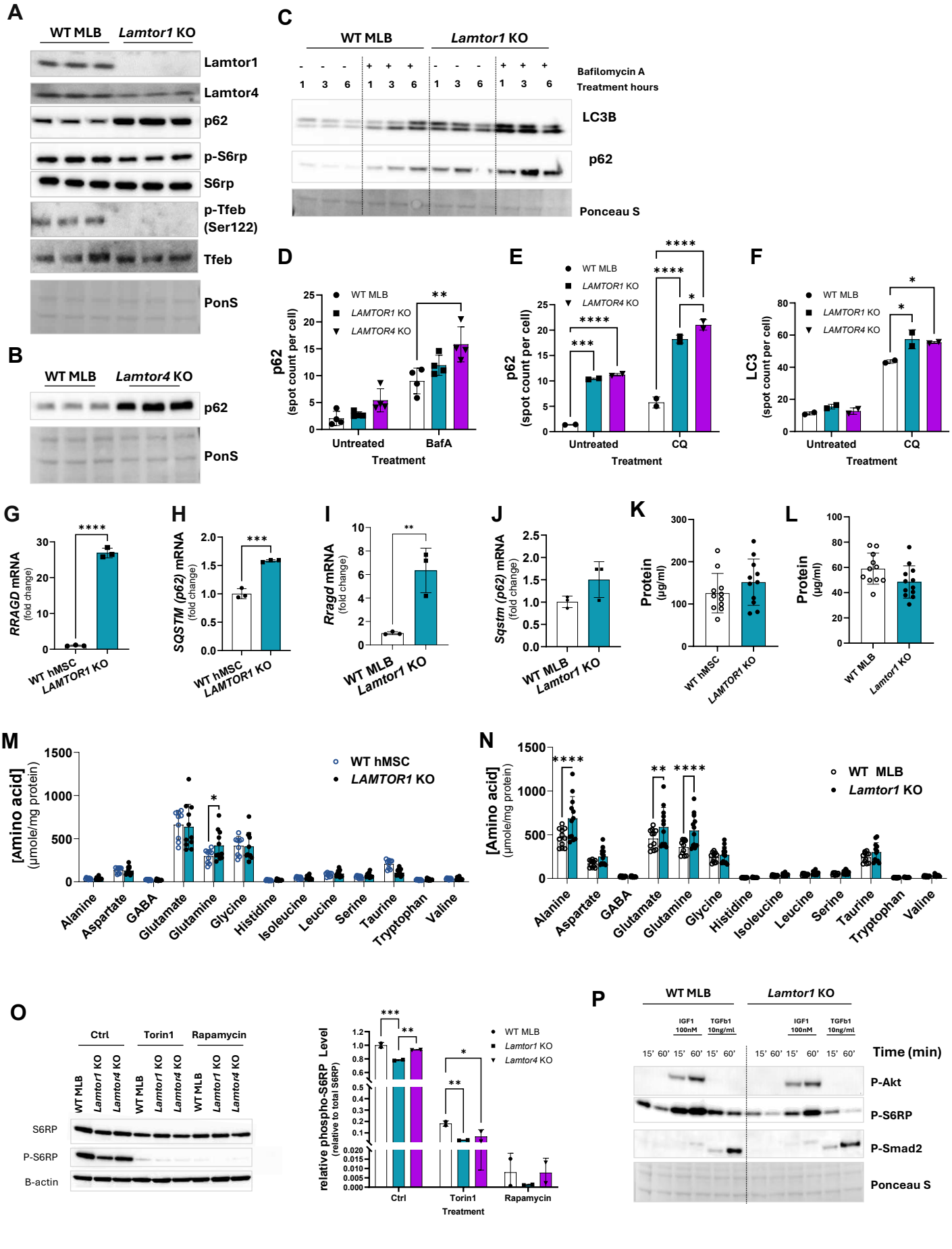
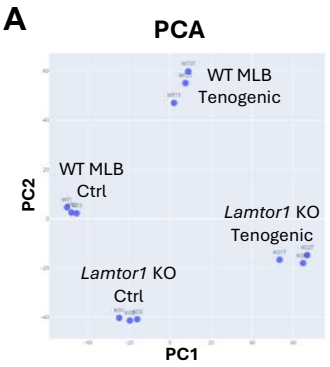
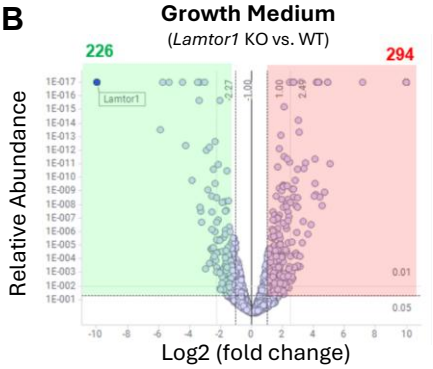
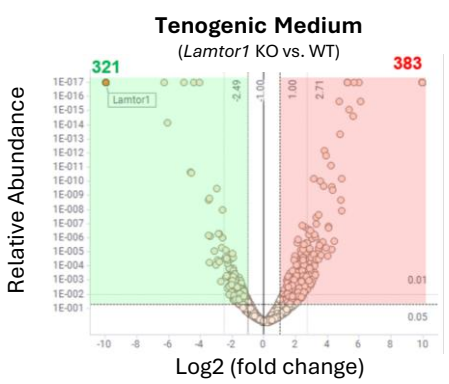

A
WT MLB
Lamtor1 KO
Lamtor1
Lamtor4
p62
p-S6rp
S6rp
p-Tfeb (Ser122)
Tfeb
PonS
B
WT MLB
Lamtor4 KO
p62
PonS
C
WT MLB
Lamtor1 KO
Bafilomycin A
Treatment hours
1 3 6 1 3 6 1 3 6 1 3 6
LC3B
p62
Ponceau S
D
p62 (spot count per cell)
WT MLB
LAMTOR1 KO
LAMTOR4 KO
Untreated
BafA
Treatment
E
p62 (spot count per cell)
Untreated
CQ
Treatment
F
LC3 (spot count per cell)
Untreated
CQ
Treatment
G
RRAGD mRNA (fold change)
WT hMSC
LAMTOR1 KO
H
SQSTM (p62) mRNA (fold change)
WT hMSC
LAMTOR1 KO
I
Rragd mRNA (fold change)
WT MLB
Lamtor1 KO
J
Sqstm (p62) mRNA (fold change)
WT MLB
Lamtor1 KO
K
Protein (µg/ml)
WT hMSC
LAMTOR1 KO
L
Protein (µg/ml)
WT MLB
Lamtor1 KO
M
[Amino acid] (µmole/mg protein)
WT hMSC
LAMTOR1 KO
Alanine
Aspartate
GABA
Glutamate
Glutamine
Glycine
Histidine
Isoleucine
Leucine
Serine
Taurine
Tryptophan
Valine
N
[Amino acid] (µmole/mg protein)
WT MLB
Lamtor1 KO
Alanine
Aspartate
GABA
Glutamate
Glutamine
Glycine
Histidine
Isoleucine
Leucine
Serine
Taurine
Tryptophan
Valine
O
Ctrl
Torin1
Rapamycin
WT MLB
Lamtor1 KO
Lamtor4 KO
S6RP
P-S6RP
B-actin
relative phospho-S6RP Level (relative to total S6RP)
WT MLB
Lamtor1 KO
Lamtor4 KO
Ctrl
Torin1
Rapamycin
Treatment
P
WT MLB
Lamtor1 KO
IGF1 100nM
TGFb1 10ng/ml
15' 60' 15' 60' 15' 60' 15' 60' 15' 60' 15' 60'
Time (min)
P-Akt
P-S6RP
P-Smad2
Ponceau S

FIGURE S5







D

Growth Medium significantly upregulated in KO

GeneName	Log2 (FC)	FC	Accession	Description
Decr2	7.18	144.97	Q9WV68	Peroxisomal 2,4-dienoyl-CoA reductase
Ca12	5.05	33.05	Q8CI85	Carbonic anhydrase 12
Cdh2	4.9	29.78	P15116	Cadherin-2
Hs6st2	4.9	29.90	Q80UW0	Heparan-sulfate 6-O-sulfotransferase 2
Tango2	4.7	26.01	P54797	Transport and Golgi organization 2 homolog
Faah	4.54	23.29	O08914	Fatty-acid amide hydrolase 1
Npepl1	4.4	21.08	Q6NSR8	Probable aminopeptidase NPEPL1
Gpnmb	4.34	20.23	Q99P91	Transmembrane glycoprotein NMB
Gm11214	4.31	19.82	V9GX06	Predicted gene 11214 (Fragment)
Aebp1	4.19	18.20	Q640N1	Adipocyte enhancer-binding protein 1
Pkp4	4.19	18.25	Q68FH0	Plakophilin-4
Krt8	4.13	17.48	P11679	Keratin, type II cytoskeletal 8

Growth Medium significantly downregulated in KO

GeneName	Log2 (FC)	FC	Accession	Description
Adamtsl4	-5.87	58.49	Q80T21	ADAMTS-like protein 4
Cd248	-5.72	52.71	Q91V98	Endosialin
Gml2	-5.32	39.95	G5E8L7	Glycosylphosphatidylinositol-anchored molecule-like 2
Cntf	-4.47	22.16	P51642	Ciliary neurotrophic factor
Thtpa	-4.23	18.77	Q8JZL3	Thiamine-triphosphatase
Plekha7	-3.82	14.12	Q3UIL6	Pleckstrin homology domain-containing family A member 7
Alms1	-3.46	11.00	Q8K4E0	Alstrom syndrome protein 1 homolog
Cav2	-3.37	10.34	Q9WVC3	Caveolin-2 OS=Mus musculus
Fblim1	-3.34	10.13	Q71FD7	Filamin-binding LIM protein 1
Pik3c2a	-3.33	10.06	Q61194	Phosphatidylinositol 4-phos.3-kin.C2 dom.-cont.sub.alpha

Growth Medium
Relative Abundance
(*Lamtor1* KO vs. WT)

E

Tenogenic Medium significantly upregulated in KO

GeneName	Log2 (FC)	FC	Accession	Description
Decr2	6.07	67.05	Q9WV68	Peroxisomal 2,4-dienoyl-CoA reductase
Gpnmb	6	64.01	Q99P91	Transmembrane glycoprotein NMB
Htra1	5.67	50.89	Q9R118	Serine protease HTRA1
Rbis	5.63	49.57	Q0VG62	Ribosomal biogenesis factor
Atp1b1	5.38	41.58	P14094	Sodium/potassium-transporting ATPase subunit beta-1
Krt8	5.27	38.70	P11679	Keratin, type II cytoskeletal 8
Xylt1	5.25	38.13	Q811B1	Xylosyltransferase 1
Ogdhl	5.24	37.87	E9Q7L0	Oxoglutarate dehydrogenase-like
Faah	4.89	29.64	O08914	Fatty-acid amide hydrolase 1
Tmem47	4.87	29.17	Q9JJG6	Transmembrane protein 47
Tysnd1	4.85	28.78	Q9DBA6	Peroxisomal leader peptide-processing protease
Pex11b	4.77	27.28	Q9Z210	Peroxisomal membrane protein 11B

Tenogenic Medium significantly downregulated in KO

GeneName	Log2 (FC)	FC	Accession	Description
Cav1	-6.27	77.17	P49817	Caveolin-1
Pde3b	-6.06	66.72	Q61409	cGMP-inhibited 3',5'-cyclic phosphodiesterase B
Lamtor5	-5.05	33.13	Q9D1L9	Ragulator complex protein LAMTOR5
Cav2	-4.65	25.11	Q9WVC3	Caveolin-2
Prg4	-4.42	21.41	Q9JM99	Proteoglycan 4
Smap	-4.09	17.03	Q9R0P4	Small acidic protein
Lbh	-3.52	11.47	Q9CX60	Protein LBH
Plin1	-3.48	11.16	Q8CGN5	Perilipin-1

Tenogenic Medium
Relative Abundance
(*Lamtor1* KO vs. WT)

F

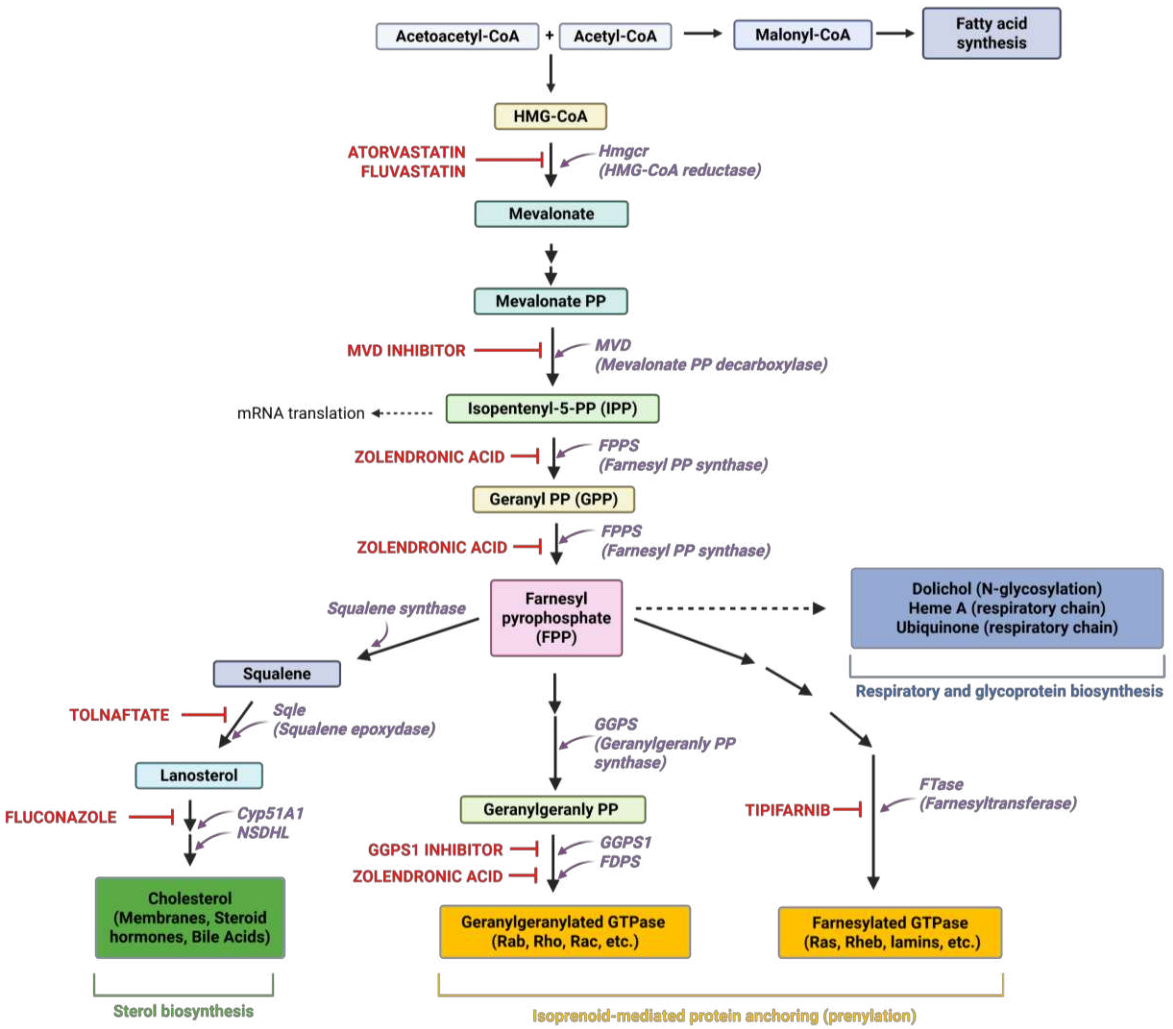
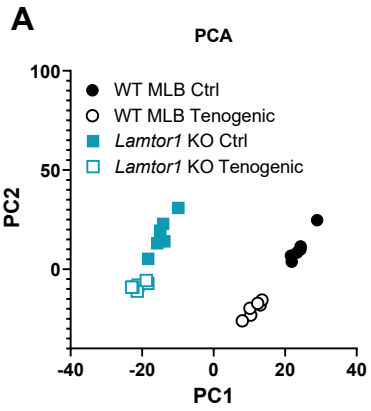
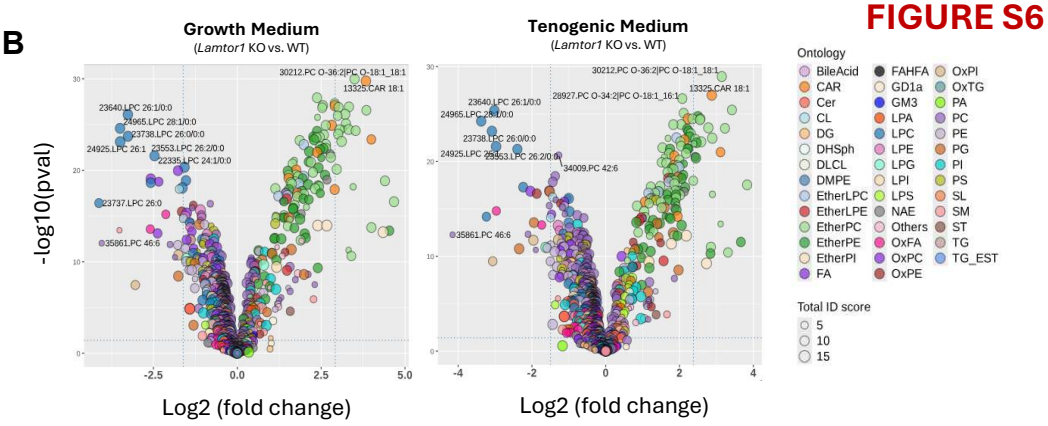
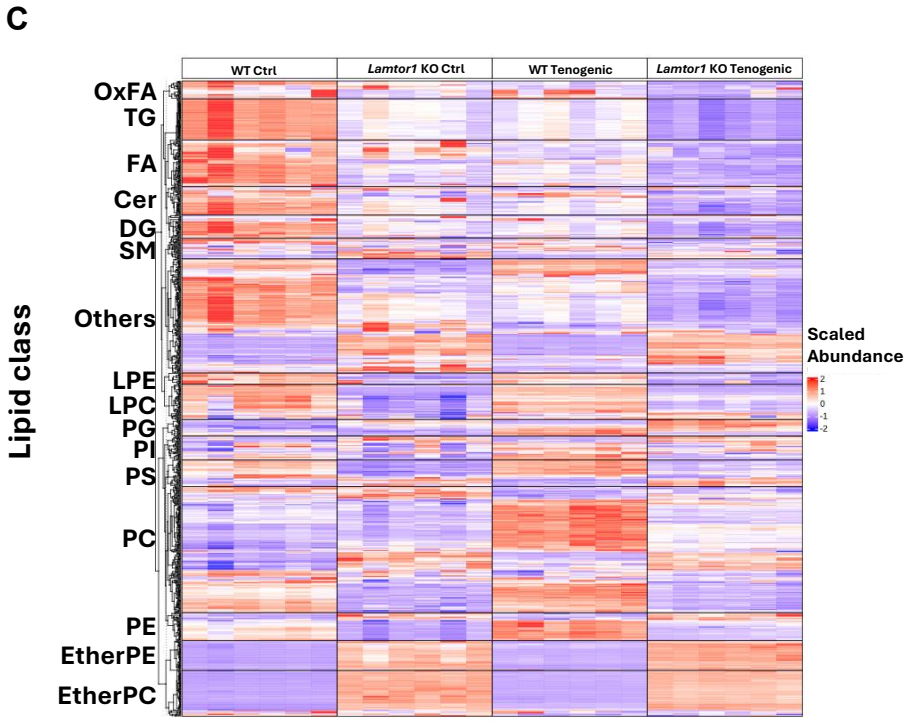
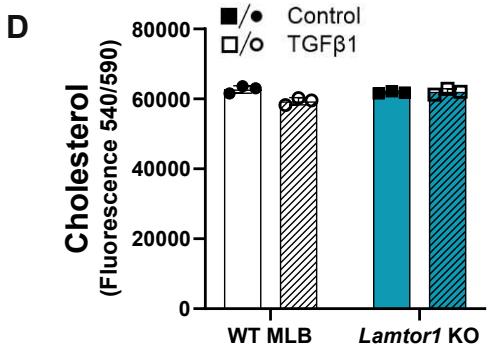


FIGURE S6


A
PCA
WT MLB Ctrl
WT MLB Tenogenic
Lamtor1 KO Ctrl
Lamtor1 KO Tenogenic
PC2
PC1


B
Growth Medium
(Lamtor1 KO vs. WT)
Tenogenic Medium
(Lamtor1 KO vs. WT)
-log10(pval)
Log2 (fold change)
Log2 (fold change)
Ontology
BileAcid
CAR
Cer
CL
DG
DHSph
DLCL
DMPE
EtherLPC
EtherLPE
EtherPC
EtherPE
EtherPI
FA
FAHFA
GD1a
GM3
LPA
LPC
LPE
LPG
LPI
LPS
NAE
Others
OxFA
OxPC
OxPE
OxPI
OxTG
PA
PC
PE
PG
PI
PS
SL
SM
ST
TG
TG_EST
Total ID score
5
10
15


C
WT Ctrl
Lamtor1 KO Ctrl
WT Tenogenic
Lamtor1 KO Tenogenic
Lipid class
OxFA
TG
FA
Cer
DG
SM
Others
LPE
LPC
PG
PI
PS
PC
PE
EtherPE
EtherPC
Scaled Abundance


D
Control
TGFβ1
Cholesterol
(Fluorescence 540/590)
WT MLB
Lamtor1 KO

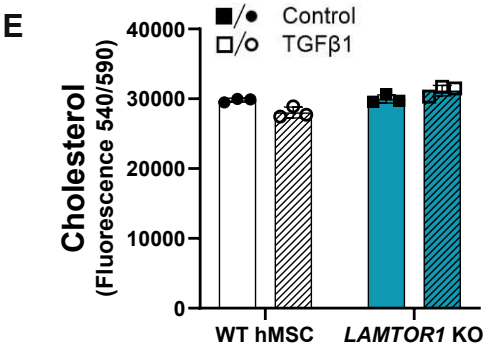
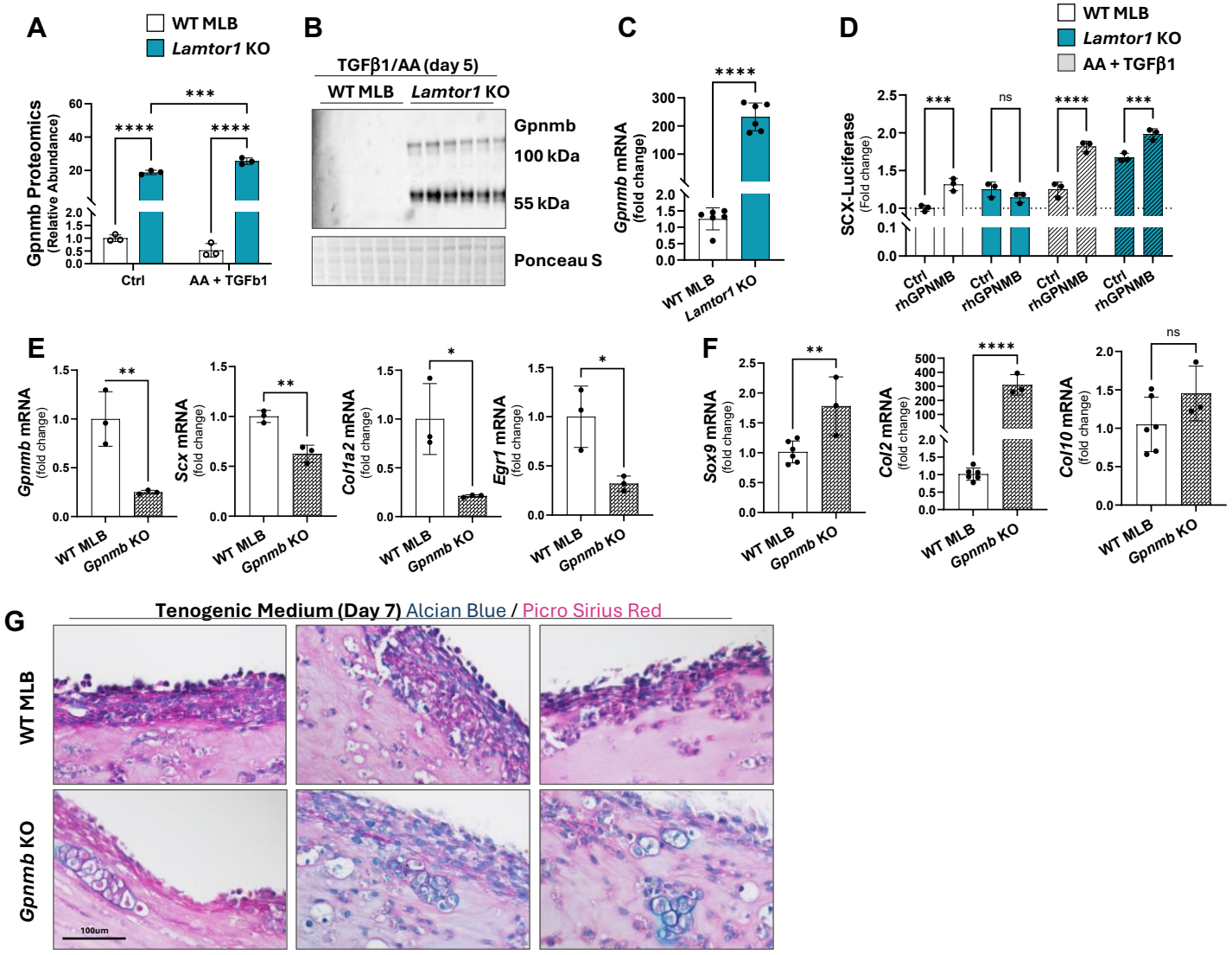

E
Control
TGFβ1
Cholesterol
(Fluorescence 540/590)
WT hMSC
LAMTOR1 KO

FIGURE S7


A
WT MLB
Lamtor1 KO
Gpnmb Proteomics
(Relative Abundance)
Ctrl
AA + TGFb1
B
TGFβ1/AA (day 5)
WT MLB
Lamtor1 KO
Gpnmb
100 kDa
55 kDa
Ponceau S
C
Gpnmb mRNA
(fold change)
WT MLB
Lamtor1 KO
D
WT MLB
Lamtor1 KO
AA + TGFβ1
SCX-Luciferase
(Fold change)
Ctrl
rhGPNMB
E
Gpnmb mRNA
Scx mRNA
Col1a2 mRNA
Egr1 mRNA
WT MLB
Gpnmb KO
F
Sox9 mRNA
Col2 mRNA
Col10 mRNA
ns

G
Tenogenic Medium (Day 7) Alcian Blue / Picro Sirius Red
WT MLB
Gpnmb KO
100um

Supplementary Files

This is a list of supplementary files associated with this preprint. Click to download.

- TableS4Antibodies.pdf
- TableS1HitsfromScxGFPGeneticScreens.xlsx
- SourcedataforLAMTORmanuscriptnoWB.xlsx
- TableS5MediaFormulations.pdf
- ImmunblotRawImages.pdf
- TableS2ProteomicsLamtor1KOvsWTMLBC.xlsx
- TableS6Primers.pdf
- TableS3SampleSizeAchillesBiomechanics.xlsx